SPECTROSCOPIC DETERMINATIONS OF MAGNETIC FIELDS, ELECTRON TEMPERATURES, AND ELECTRON DENSITIES IN SINGLE WIRE ALUMINUM PLASMAS

A Dissertation

Presented to the Faculty of the Graduate School

of Cornell University

in Partial Fulfillment of the Requirements for the Degree of

Doctor of Philosophy

by

Kate Suzanne Blesener

August 2012

SPECTROSCOPIC DETERMINATIONS OF MAGNETIC FIELDS, ELECTRON TEMPERATURES, AND ELECTRON DENSITIES IN SINGLE WIRE ALUMINUM PLASMAS

Kate Suzanne Blesener, Ph.D.

Cornell University 2012

This dissertation provides a detailed determination of the visible emission spectra and plasma parameters of an exploding single aluminum (Al) wire while addressing the applicability of a new spectroscopic measurement technique to measure magnetic fields (B) in dense plasmas, where magnetic field measurements were previously unobtainable. Through the use of this new technique, hereafter called "Zeeman Broadening", there was evidence for magnetic fields in the spectra and a measurement was made.

The Zeeman Broadening technique was first proposed and employed at the Weizmann Institute of Science in Rehovot, Israel [47] and is based on the difference in line-widths of two fine structure components of the same multiplet that undergo different splittings due the magnetic field.

Experiments were conducted exploding fine Al wire using Cornell's Low Current Pulser 3 (LCP3), a pulsed power generator that initially produced a 10 kiloamp (kA) current pulse with a rise time of 500 nanoseconds [16]. It was later modified to produce up to 13kA with a 450ns rise time. Aluminum 1100 alloy wires were used, which are 99.9% Al. The wire length was 1.0cm, and the diameter ranged between 15μm and 33μm. The primary diagnostics included a high resolution grating spectrometer coupled to either a Kentech gated optical imager (GOI), Princeton Instruments PIMax3 gated intensified charge-coupled

device (ICCD), or an Andor iStar ICCD. Additional diagnostics included pulser current, wire current, and load voltage monitors.

The first set of experiments, with the GOI, were exploratory and meant to determine an initial electron temperature and electron density. Using these data it was concluded that the plasma parameters were conducive to the Zeeman Broadening technique, and the PIMax3 camera was borrowed from Princeton Instruments to create a diagnostic setup with resolution sufficient for studying the magnetic field. While the spectra were unsatisfactorily noisy, a magnetic field of $B = 3.5T$ was fitted to a spectrum at a radius of $500\mu m$ from the initial wire position at peak current. This result implies a high portion of the 10kA current remained within $r \leq 500\mu m$, even though the plasma had expanded beyond a $2mm$ radius.

To gather more data with improved signal-to-noise ratios, a Shamrock 500i spectrometer and iStar camera were borrowed from Andor Technology. The spectra were analyzed to determine electron density n_e and electron temperature T_e over many radii throughout the evolution of single wire explosion. Over the entire single wire explosion, the n_e ranged between $8 \times 10^{16} cm^{-3}$ and $1.6 \times 10^{18} cm^{-3}$, while the T_e was measured between $2eV$ and $4eV$. The exploding wire plasma formed a hot less dense plasma shell surrounding a colder and denser core, both expanding outwards at a rate of $\sim 3km/s$. In the Andor data set there also existed indications of measurable magnetic field that implied significant portions of current was flowing within $r \leq 500\mu m$, in agreement with the previous results.

BIOGRAPHICAL SKETCH

Kate was born on March 5th, 1984 to parents Greg and Michele Bell. She grew up in Albuquerque, New Mexico with sister Anne. After high school, Kate went on to study physics and economics at Duke University. Several summer internships at Sandia National Laboratories during her undergraduate career developed her interest in fusion and plasma physics, which lead her to choose the Laboratory of Plasma Studies at Cornell University for her graduate education. While at Cornell, she met and married her husband Isaac.

To Isaac

ACKNOWLEDGEMENTS

I would like to acknowledge my thesis advisor Dave Hammer for his guidance, support, wisdom, and friendship. I also thank him for allowing me the independence to develop my own strengths and my own thesis. Through his mentorship I have grown immeasurably, both as a scientist and as an adult. I would like to acknowledge Professor Maron and Dr. Ramy Doron for their guidance and insight. They both inspire me to strive for precision in my understanding, and accept nothing less. I would like to thank Sergei and Tania for their their endless ideas. I strive to emulate their ability to efficiently turn those ideas into creations. I would like to thank Harry and Todd for the all of the problems they've solved and always being there to lend me a helping hand. I would like to thank Bruce for his friendship and his many home cooked meals. I thank all of the LPS graduate students that have spanned my time at Cornell for their friendship, guidance, support, and fond memories. I also am very thankful for my parents unwavering support and loving generosity. I also thank my loving husband Isaac. It has been a joy and an honor to have gone through our degrees together, and to continue to support each other in our accomplishments.

TABLE OF CONTENTS

LIST OF FIGURES

CHAPTER 1

INTRODUCTION

1.1 Motivation

Pulsed-power generated wire array Z-Pinches have proven to be an efficient and powerful source of laboratory radiation [34], making the physics of these systems an important field of study. Understanding single wire explosions, also driven by pulsed-power generators, is an important step for understanding the complex physics of wire array Z-Pinches. While they share many similarities, there are also differ in many ways. In single wire explosions the current causes the wires to heat, expand, and explode in a multiphase state or perhaps fully vaporized. Then, with sufficient current, the self induced magnetic field can act to reduce the expansion and cause a pinching of the plasma.

In wire array Z-Pinches, several single wires are commonly arranged in a cylindrical patten. The current running through the wires provides a mechanism to heat and vaporize the material and then the global azimuthal magnetic field creates a pinching force that can accelerate material to the central axis where it stagnates. During the beginning of this process, the global magnetic field close to the wire can be small compared to the individual wire's local magnetic field and the argument can be made that wires in a Z-Pinch can be approximated as single exploding wires early in time. This approximation is valid when the wire-to-wire spacing in the array is large enough so that adjacent expanded wire plasmas do not overlap. This is always the case early in the current pulse before the wires expand.

Additionally, early in time during a Z- pinch, an individual wire's magnetic pressure due to the local magnetic field is less than the kinetic pressure of the exploding wire plasma, which leads to an expansion of the wire plasma. For a Z-Pinch, this kinetic pressure is eventually overcome by the growing magnetic pressure of the global field, which sweeps material toward the central axis. But for those early times before the global field dominance, the individual wire explosion scenario is comparable to that of a single wire explosion, which makes these plasmas great candidates for studying the plasma physics that seeds the more complex physics of wire array implosions.

While the physics of single wire explosions has been investigated for some time, the understanding of the physics has been limited by the diagnostics available. With the continuing development of high-precision diagnostic equipment, we are now able to create extremely high resolution spectroscopic systems with resolving powers R upwards of 9000 (defined as the wavelength of the line of interested divided by the full-width-half-max of the line: $R = \lambda/\Delta\lambda$), with extremely high photon sensitivity and gain. With these high sensitivity high resolution systems, we are now able to measure spectroscopic line profiles in very short lived plasmas. These technology advances, with advantages in analysis techniques, e.g. the Zeeman Broadening technique, allows us to measure regimes and plasma properties that were previously inaccessible.

The high energy density (HED) plasma community is working hard to determine the location of the current flow in HED plasmas. Diagnosing the current location, direction, and magnitude are very challenging because any current probes placed in the plasma could be hugely disruptive and therefore could not be trusted. Therefore, it is advantageous to measure the magnetic fields

remotely and thereby determine the current information. There are several ways to measure the magnetic field in plasma, including Faraday rotation, B-dot probes, and spectroscopic techniques based on Zeeman splittings of emission lines.

Within high energy density (HED) plasmas, spectroscopic measurements based on Zeeman splittings techniques are most often impractical or entirely impossible due to the physical conditions of the plasma, such as extremely high electron density or ion temperature to name two. When either or both of these are large, emission lines are broadened. Within HED plasmas, the line profiles are typically broadened by these effects sufficiently such that any Zeeman splittings caused by magnetic fields are no longer resolvable.

The need to extend the parameter space in which we can spectroscopically determine the magnetic field led to the development of the Zeeman Broadening technique. This method was conceived and demonstrated at the Weizmann Institute of Science (WIS) in Israel, using laser blowoff plasmas [47]. It is important to note that in the Zeeman Broadening benchmarking experiments at the WIS, the B-field did not vary along the line of sight and was decoupled from the plasma [47]. In the experiments presented in this thesis, the magnetic field was *not* decoupled from the plasma and the magnetic field *did* vary over the line-of-sight. This difference makes inferring the magnetic field using Zeeman Broadening in the wire explosion experiments more difficult than in the benchmarking experiments at the WIS.

With the Zeeman Broadening method, two different fine structure components of a multiplet are simultaneously measured and compared with simulated line profiles to determine the electron density and the magnitude of the mag-

netic field. The groundbreaking feature of this technique is that the individual splittings due to the magnetic field do not have to be individually resolvable. Rather, the two composite broadened lines have enough information when analyzed as a pair to extract information about the magnetic field and electron density in the plasma in the observation region.

Since magnetic field information can be gathered by this technique using carefully selected lines that are substantially broadened by high local electron density and/or ion temperature, it is now in principle possible to diagnose magnetic fields in plasmas with higher electron density and ion temperatures than was possible up to now. This extension of the measurable parameter space could contribute greatly to the range of HED plasmas that can be understood.

Presented in Chapter 2 is an overview of the Low Current Pulser 3 (LCP3) pulsed power generator, used to drive the experiments presented in this thesis. The various diagnostic setups for the data presented in this thesis are described in Chapter 2.

Chapter 3 is a discussion of the types of continuum and characteristic radiation encountered in single wire plasmas. Chapter 4 describes the spectroscopic measurement techniques used in analyzing the data presented in this thesis, with a lengthy discussion about Zeeman splitting and Zeeman Broadening. The current challenge of the Zeeman Broadening method is the application to scientifically significant plasma experiments, which is also discussed in Chapters 4 and 6.

Chapter 5 presents results from experiments designed to measure the evolution of the electron density and temperature throughout the explosion of the

single aluminum wire. The first section includes a small subset of the initial exploratory experiments designed to evaluate the feasibility of a Zeeman Broadening measurement in single exploding wire plasmas. The second section presents results of detailed experiments that characterize the single exploding wire plasma, both as a function of time and position.

Additional exploratory experiments were performed at the initiation of this thesis project which are not included in detail in this thesis. Experiments began on Cornell's X-Pinch (XP) pulser, with results presented at the 2008 Dense Z-Pinch (DZP) Conference and published in the DZP proceedings [2]. Later on the experiments were redesigned and transitioned to Cornell's LCP3 pulser. Initial time-integrated single wire results from LCP3 were presented at the 2010 IEEE International Conference on Plasma Science [6]. The first set of time-resolved single wire experiments used a Hamamatsu optical streak camera, and the results were presented at the 52nd Annual Meeting of the American Physical Society Division of Plasma Physics [5].

Chapter 6 presents the results from high resolution experiments designed to explore the Zeeman Broadening magnetic field and electron density measurement technique. Evidence was found that suggests the presence of magnetic fields in the plasma and a detailed line profile fit was performed.

Chapter 7 summarizes all of the results for the single exploding wire experiments and presents interesting and related experiments that could be performed in the future.

1.2 Z-Pinches & Single Wire Explosions

Z-Pinches and single wire explosions are very similar in many ways. Perhaps the best way to explain them together while highlighting key differences is through a discussion of the Bennett pinch equilibrium in a column of current carrying plasma. In the plasma column, there are two main pressure sources. They are magnetic pressure and thermal pressure. The magnetic pressure works to pinch the plasma column, while the thermal pressure works to expand the plasma column. In the simplest form, the Bennett pinch condition states that there is a point at which the magnetic pressure will balance the thermal pressure and the column will be in equilibrium.

The pinching force, in essence, results from the Lorentz force, the electromagnetic force that acts on a single charged particle [28]. Here, q is the particle charge, $\mathbf{E}$ is the electric field, $\mathbf{v}$ is the velocity of the particle, and $\mathbf{B}$ is the magnetic field.

$$\mathbf{F} = q(\mathbf{E} + \mathbf{v} \times \mathbf{B}) \tag{1.1}$$

A plasma never consists of a single particle, and to solve the system computationally using only Maxell's equations and Lorentz forces is not practical. Therefore assumptions and other models are necessary. The most used and appropriate assumption is quasi-neutrality, and the plasma can often be treated using a collisionless two-fluid model. This model introduces equations of motion for electrons and ions that include a thermal pressure term ∇p [10], which is key to the Bennett equilibrium. For a particle x (either e for electron or i for ion), the mass of the particle is m_x, the particle number density is n_x, and $\dot{\mathbf{v}}_\mathbf{x}$ is the velocity time derivative.

$$m_e n_e \dot{\mathbf{v}}_e = q_e n_e(\mathbf{E} + \mathbf{v}_e \times \mathbf{B}) - \nabla p_e \tag{1.2}$$

$$m_i n_i \dot{\mathbf{v}}_i = q_i n_i (\mathbf{E} + \mathbf{v}_i \times \mathbf{B}) - \nabla p_i \tag{1.3}$$

Bennett was the first to derive the equilibrium equation from the motion equations in a form which states that the equilibrium condition occurs with a particular current for a given temperature and electron line density (electrons per unit length) in a singly ionized plasma. To arrive at Eqn. 1.4, Bennet assumed electrostatic neutrality, axial and azimuthal uniformity, and a stationary state meaning no electric field. He also assumed that all the electrons have the same velocity of u, and that all of the ions have the same velocity of v but in the opposite direction [3].

$$i_0 = \frac{[c^2 * 2k_B(T_1 + T_2)]}{e(u + v)} \qquad [c.g.s.] \tag{1.4}$$

Here $i_0 = Ne(u + v)$ and is the driving current with $N = \pi a^2 \langle n \rangle$, $\langle n \rangle$ is the radially averaged electron density (defined below in Eqn. 1.6), T_1 is the electron temperature, T_2 is the ion temperature, e is the electron charge, c is the speed of light, and k_B is the Boltzmann constant . Equation 1.4 is from Bennett's original paper in c.g.s. units, in a form not often used by present day plasma physicists.

To change the units of Eqn. 1.4 into MKS and a more intuitive form for the experimentalist, it might be best to rederive the equilibrium from the two-fluid motion equations in MKS units. The result is Eqn. 1.5, where I_B is the driving current, a is the radius of the pinch column, $T_{e,i}$ are the election and ion temperatures, and $\langle n \rangle$ is the average volume particle density ($\#/m^3$)given below in Eqn. 1.6.

$$I_B^2 = \frac{8\pi^2 a^2}{\mu_0} \langle n \rangle k_B (T_i + T_e) \tag{1.5}$$

$$\langle n \rangle = \frac{\int_0^a n(r) 2\pi r dr}{\pi a^2} \tag{1.6}$$

From Eqn. 1.5, in which singly charged ions are still assumed, the relationship between the size, temperature, density and driving current is clear when the column is in equilibrium.

1.2.1 Z-Pinches

When the plasma column is not in equilibrium and the magnetic pressure is larger than the thermal pressure we get a pinching of the plasma toward the axis, usually denoted as the z axis. This is the case in the implosion of a Z-pinch as the current rises.

The usual wire array Z-pinch configuration is a cylindrical array of parallel fine metal wires. It is typically described as having four main phases. First a current is driven through these wires, which causes them to heat ohmically until they breakdown, creating a plasma around a solid wire core. This is typically referred to as the initiation stage.

The ablation stage begins after voltage breakdown, during which the magnetic pressure around the individual wires is smaller than the thermal pressure and the plasma will expand forming a coronal around the wire cores. The global $\mathbf{J} \times \mathbf{B}$ begins to drive coronal plasma to the central axis in so-called ablation streams, beginning to form a column of plasma called the precursor.

As the driving current increases, so will the global $\mathbf{J} \times \mathbf{B}$ force, which will continue to sweep plasma away from the wire corona. Once enough material has been removed and gaps form in the wire cores, the ablation phase transitions to the implosion phase [4]. During the implosion phase there is a sweeping

in of a majority of the material remaining near the original radius of the array by the $\mathbf{J} \times \mathbf{B}$ force. Once the bulk of the plasma reaches the axis, the Z-pinch is in the stagnation phase. The majority of the x-ray radiation from the experiment occurs during stagnation. However, it should be noted that the plasma radiates during the entire experiment with varying intensities and photon energy spectra. Additionally magnetized Rayleigh-Taylor (RT) instabilities develop during the ablation stage that develop further during implosion and stagnation. These instabilities can greatly affect the x-ray pulse duration and the composition of line radiation in the x-ray pulse.

1.2.2 Single Wire Explosions

A single wire explosion of the kind that is the subject of this thesis has a lot of similar characteristics to the individual wire explosions in the initiation and ablation stages in a wire-array Z-pinch. However, the main difference occurs in the pressure balance following the ablation phase. Unlike a Z-pinch, in a relatively low current single wire explosion the thermal pressure almost always exceeds the magnetic pressure, inhibiting any pinching of the plasma. The important parameter here is the driving current. If the current is large enough in a single wire explosion, it is possible to get some pinching of the plasma back onto itself. However, this is not the case for the experiments presented in this thesis.

Pulsed power driven single wire explosions with many types of wire materials have been studied in detail over the last 50 years. To give a few recent examples among many experiments, the single wire topics of previous study include

polarity effects [16, 18, 40], energy disposition [8, 9, 16, 18, 37, 43, 44], electrode contact effects [16, 18], wire expansion rates [8, 9, 16, 18, 24, 25, 37, 43, 44], and plasma and core structure [24, 25, 29, 36, 37]. Only a few experiments exist on current density through the explosion [16, 17] or visible spectra emitted by these plasmas [30]. More information on these experiments may be found in the cited articles and the references within.

The current density profile is one of the most difficult measurements to make in HED plasmas, including single exploding wires. As such, the spatial dependence of the current flow is poorly understood. One previous experiment attempting to measure current in these types of plasmas was performed by Dr. Peter Duselis as part of his thesis experiments at Cornell University [16, 17]. Using a three electrode wire holder, see Fig. 1.1, Duselis measured how the current transferred from the center regions of the plasma to outer radii by measuring the total current and the current through the Lower Cathode Plate. Therefore the difference in these measurements must be flowing through the Upper Cathode Plate.

Duselis discovered a gradual expansion of current to radii $r \geq 700\mu m$, limited by the inner diameter of the Upper Cathode Plate, with all of the current flowing through the Upper Cathode Plate at peak current. It would be possible for current to be flowing at considerably larger radii than $700\mu m$, but would not change the signal in these experiments. While these experiments measured an outward expansion of current density, it is difficult to unfold the effects of the cathode structure from the results. Therefore, there is still a great need for non-perturbing measurements of the current density profile, either directly or indirectly (e.g., by way of the B field distribution).

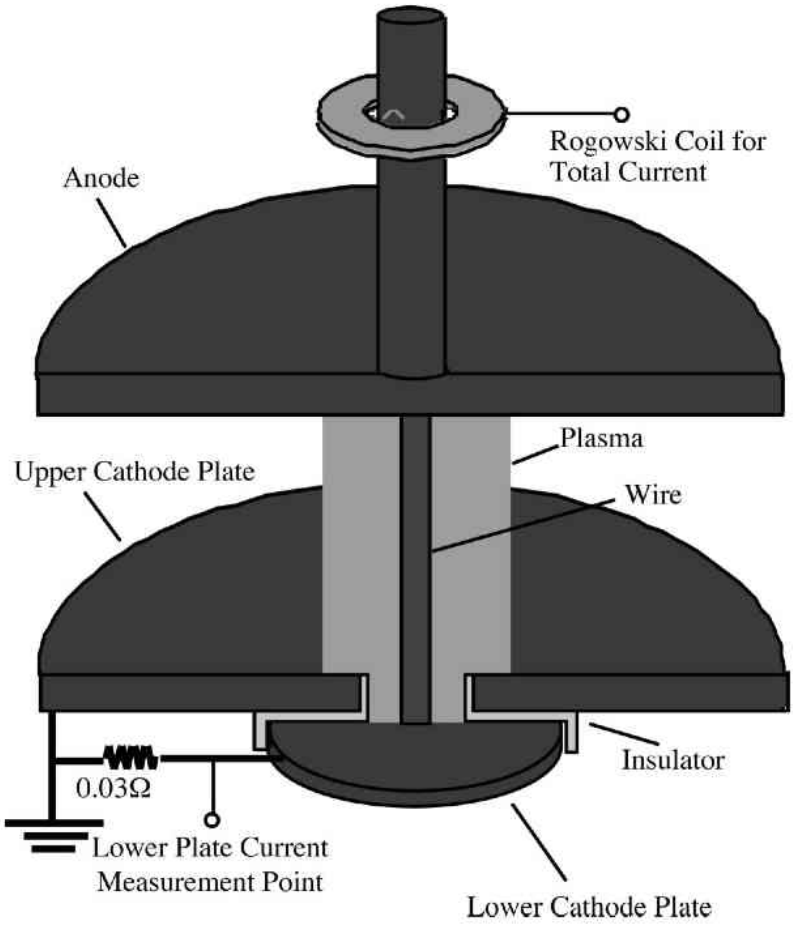

Figure 1.1: Three electrode wire holder used by Duselis to study the transfer of current from immediately around the wire to radii greater than the inner radius of the Upper Cathode Plate [16, 17]. The top Rogowski coil measured the total current while the resistor allowed for measurements of the current through the Lower Cathode Plate.

It is important to gain a full understanding of the beginning plasma properties, including developing instabilities, since this plasma seeds the physical processes that take place in the wire-array Z-pinch. The experiments discussed in this thesis are driven by an average current rate of rise of $25A/ns$. As such, they can be compared to the first ten's of nanoseconds of a Z-pinch's initiation and ablation phases when the current drive per wire is also around $25A/ns$.

CHAPTER 2

THE LCP3 PULSED POWER GENERATOR

A pulsed power generator is uniquely capable of driving the high current levels necessary to drive short pulse Z-pinches or single wire explosions. These devices operate by storing up a large amount of electrical energy in capacitors over a long period of time. The stored energy is then released in a very short amount of time, generally microseconds to nanoseconds. Some pulsed power devices use additional pulse forming lines and switches to compress the current pulse further. Typical current rise times of pulsed power drivers range between $50ns$ and $500ns$. The current level and rise time depend on the capacitance, the inductance, and the pulse compression stages of the individual generator.

2.1 Overview of LCP3

The experiments in this thesis were conducted on the Low Current Pulser 3 (LCP3), which originally produced up to $10kA$ of current [16]. It consists of a single $0.2\mu F$ capacitor charged to between $-23kV$ and $-30kV$. The capacitor is connected to a triggered gas switched, which is filled with 4 to 6 psi of nitrogen gas. The mid-plane of the switch is held at half the charging voltage by a chain of resistors. A high voltage pulse from a PT-55 sends a signal to the mid-plane of the switch which causes the switch to close and the voltage pulse to proceed down the power feed to the wire load. A picture of the LCP3 showing the PT-55, capacitor, gas switch, and top of the chamber is shown in Fig. 2.1. The power feed started out simple in a loop configuration, as opposed to coaxial or a strip line configuration. As a result of the inductance of that configuration, a charge of $-23kV$ on the capacitor produced a current of $10kA$ with a $500ns$ rise time

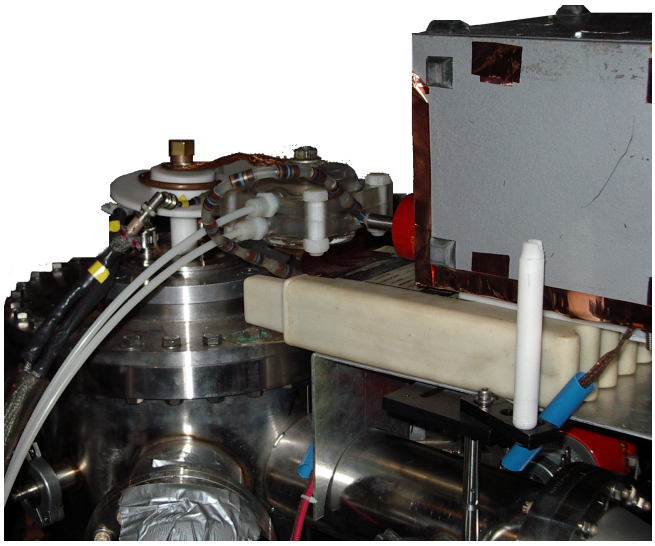

Figure 2.1: Pictures of LCP3 showing the PT-55, capacitor, gas switch, and top of the LCP3 chamber.

through a $1cm$ long wire.

With a rise time of $500ns$ we can use Eqn. 2.1 for the resonant angular frequency of an LC circuit to determine an approximate inductance for LCP3.

$$\omega_0 = \frac{1}{\sqrt{CL}} \tag{2.1}$$

Taking $0.2\mu F$ for the capacitance C, we determine that LCP3 must drive a circuit inductance L of $500nH$.

Efforts were made to reduce LCP3's inductance in order to increase the machine's performance. This included adding additional ground paths from the load to ground, shortening the power feed, and switching part of the power feed from copper mesh to a copper strip. These changes reduced the rise time to $430ns$, and increased the current by about $1200A$. With a charging voltage of $-30kV$, LCP3 produces $13.2kA$ with a rise time of $430ns$. Using Eqn. 2.1 again,

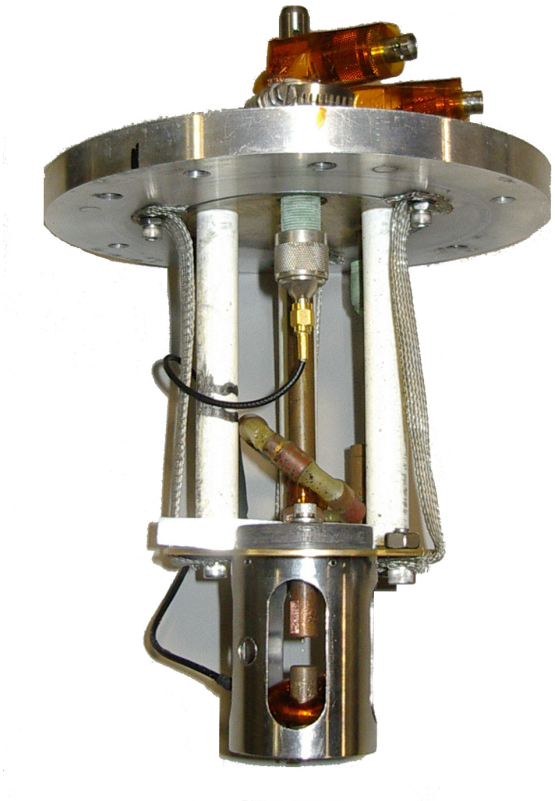

Figure 2.2: Picture of the LCP3 vacuum power fed and wire holder with additional ground paths. The second Rogowski coil is fitted around the anode of the wire holder, and the voltage monitor is seen wrapping around the power feed.

but with the new rise time, the inductance was reduced to $375nH$.

Changes to the system were made in the Andor experimental setup that were intended to increase the light collection efficiency in the exploding wire experiments. These changes are described in Sec. 2.3.3. They increased the inductance slightly, reducing the current to $13.0kA$ with a charge of $-30kV$.

2.2 Diagnostics on LCP3

2.2.1 Current Monitor

Two non-integrating Rogowski coil current monitors were used to measure the current on LCP3 and in the exploding wire. A non-integrating Rogowski consists of a wire with one lead turned into helical coil surrounding a return wire in the center of the coil. The coil is then bent to form a circle. Figure 2.3 is a drawing of a Rogowski coil with the key features noted and labeled. This circular coil is then placed around a current-carrying circuit element, e.g. a current carrying rod. The current produces a magnetic fields which, in turns, induces a voltage across the monitor leads that is directly proportional to the rate of change of the magnetic flux due to the current. The resulting voltage signal is a measurement of the first derivative of the current, dI/dt. To determine the magnitude of the current I, the signal must to be integrated with respect to time and multiplied by a calibration factor. The location of the current within the Rogowski coil does not matter. It will measure the current correctly as long as the entire current is contained within the coil [26].

One of the current monitors was a large diameter Rogowski coil that was placed after the current switch at the beginning of the power feed, which was outside of the vacuum chamber. The second Rogowski had a much smaller diameter and was placed around the anode section of the wire holder, as seen in Fig. 2.2, to measure the current through the wire. This setup was necessary as it enabled detection of breakdowns or current loss in the power feed.

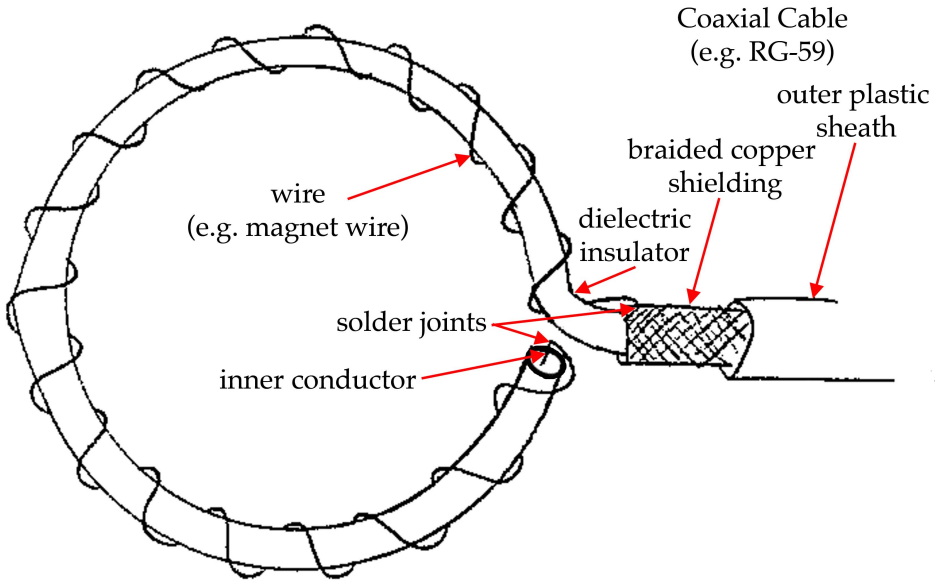

Figure 2.3: Diagram of a non-integrating Rogowski coil. (Figure from Isaac Blesener's thesis.)

2.2.2 Voltage Monitor

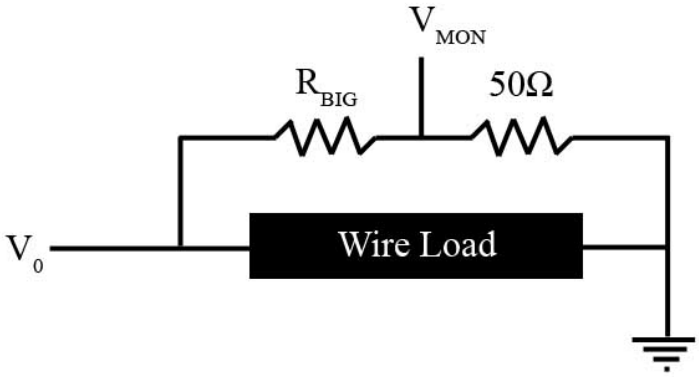

Figure 2.4: Diagram of the voltage monitor's circuit.

A high impedance voltage monitor is connected in parallel with the single wire load such that it leaches a very small amount of current from the load. Within the voltage monitor, a simple resistive voltage divider is used to record a low voltage signal that is directly proportional to the load voltage. Figure 2.4

shows a circuit diagram of the voltage monitor. A 50Ω resistor is used to connect the monitor output to ground, so that the impedance of the monitor will match the impedance of the cable connected to the V_{MON} output point. The voltage monitor is seen in Fig. 2.2 as the chain of resistors wrapping around the power feed leading to the wire holder.

2.2.3 Spectrometers

Two types of spectrometers were used to collect spectra in the visible bandwidth between 350*nm* and 700*nm*. The first type was a ruled concave grating spectrometer with a 1 meter focal length. It had the capability to take high spectral resolution measurements. However, this spectrometer was used only during the collection of the preliminary data due to its low efficiency at visible wavelengths with the higher resolution settings.

The second type was a Czerny-Turner spectrometer, with a 1/2 meter focal length. Two different spectrometers of this type were used to collect data. One was built by λ Minuteman, and the other was built by Andor Technologies. While there were subtle difference in the design of the two spectrometers, the basic principle of operation is the same, and is depicted by the drawing in Fig. 2.5. All Czerny-Turner spectrometers have an entrance slit, two concave focusing mirrors, and a ruled grating. The dispersion and resolution of the system is dependent on these four components.

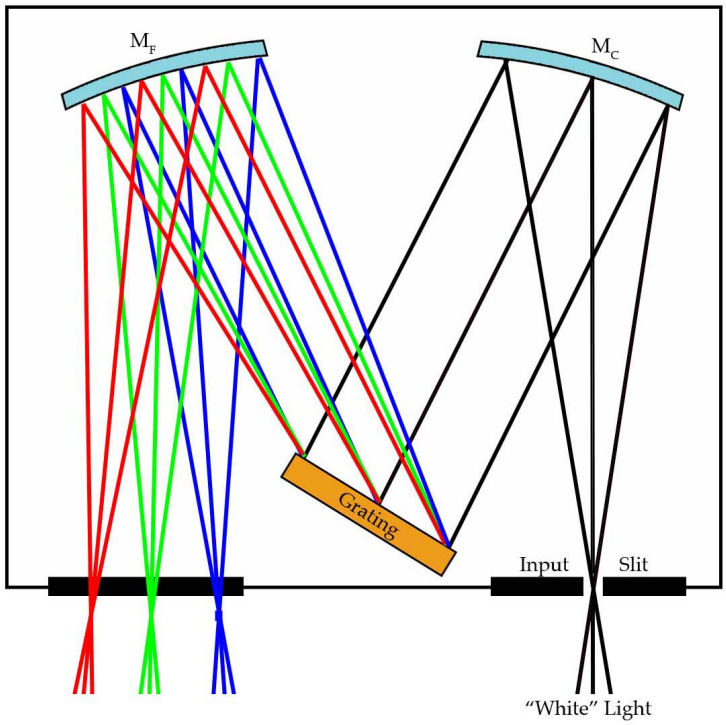

Figure 2.5: Drawing of the Czerny-Turner Spectrometer's principle of operation. M_C is the collimating concave mirror; M_F is the focusing concave mirror.

Dispersion

First, polychromatic light is focused onto the entrance slit of the spectrometer. The light then hits the first mirror M_C, which collimates the light into a parallel beam. The parallel light then interacts with the grating and each component wavelength of the light is diffracted at a different angle according to the grating equation [32], given in Eqn. 2.2. With respect to the grating normal, α is the angle of incidence and β is the angle of diffraction given in degrees, as shown in Fig. 2.6. The groove density is n in terms of $grooves/millimeter$. The diffraction order is k, and λ is the wavelength in $nanometers$.

$$\sin\alpha + \sin\beta = 10^{-6} kn\lambda \tag{2.2}$$

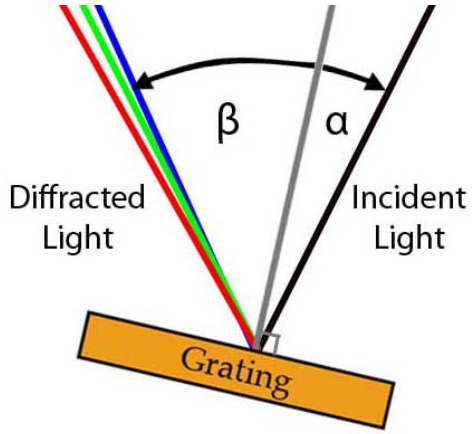

Figure 2.6: Diffraction angles due to a ruled grating.

The central wavelength of light λ is dispersed along the spectrometer's focal field according to Eqn. 2.3 with units of nm/mm, which correspond to a spectral dimension over a physical dimension [32]. This is called the linear dispersion. The new term L_B in Eqn. 2.3 is the distance between the grating and spectral focal plane, often called the "exit arm". The constants of 10^{-6} in Eqn. 2.2 and 10^6 in Eqn. 2.3 results from using the given units.

$$\frac{d\lambda}{dx} = \frac{10^6 \cos\beta}{knL_B} \quad [nm/mm] \tag{2.3}$$

Often it can be more illustrative to consider the dispersion in terms of $dx/d\lambda$. As $dx/d\lambda$ we see that a given spectral range $d\lambda$, say $1nm$, is spread over a certain physical dimension dx. From this we can see the direct relation between dispersion (and later resolution), the spectrometer's focal length, and the grating's groove density. The "$1nm$" is spread over a larger distance as we increase the exit arm length L_B and/or increase the groove density n.

Resolution

The resolution of a spectrometer is the ability of the spectrometer to separate two adjacent lines. It is based on the Rayleigh criterion and often quoted in terms of an infinitely narrow line's full width at half max (FWHM) after passing through the spectrometer. To determine the resolution, two factors must be considered. These are the limiting instrumental line profile of the spectrometer and the impact of the entrance slit width. When calculating the spectrometer's resolution the assumption is made that the natural line width of our hypothetical line is zero, and will not contribute to the FWHM. Therefore the natural line width will not be included at this stage.

The instrumental line profile is calculated from the resolving power of the spectrometer. The term resolving power has two definitions, and care must be taken to avoid confusion. The first is based on the original dimensionless definition of resolving power used to describe a system's actual performance, given in Eqn. 2.4.

$$R = \frac{\lambda}{d\lambda} \tag{2.4}$$

λ is the line under consideration and $d\lambda$ is the measured FWHM. In this context, R is used to express the working capability of a spectrometer system independent of the wavelength. For instance a FWHM alone, or resolution, of $1\mathring{A}$ would be terrible for working with x-rays while it would be excellent if working with infrared radiation. However, by expressing the resolution in terms of resolving power R, one is able to relate the capabilities of a spectrometer system.

The second definition and usage of R is for calculating theoretical maximum resolving power of the spectrometer. This is important when determining the

limiting resolution of a spectrometer. From Eqn. 2.4 it can be shown that

$$R = \frac{\lambda}{d\lambda} = knW_g = kN \tag{2.5}$$

where W_g is the width of the grating and N is the total number of grooves [32]. Rearranging to give the limiting instrumental line profile $d\lambda_{res}$ we have

$$d\lambda_{res} = \frac{\lambda}{kN} \tag{2.6}$$

Equation 2.6 is the formula that should be used in combination with the impact of the entrance slit width to determine a spectrometer's expected resolution.

The contribution to the FWHM from the entrance slit is due to the bandpass $d\lambda_{slit}$ based on the slit width w_s. This is found by multiplying the slit width by the linear dispersion given in Eqn 2.3:

$$d\lambda_{slit} = w_s * \frac{d\lambda}{dx} \, . \tag{2.7}$$

To determine the FWHM of the spectrometer we assume Gaussian line profiles and take a convolution of the two contributions, keeping in mind the assumption that the natural line width of our hypothetical line is zero.

$$FWHM = \sqrt{d\lambda_{res}^2 + d\lambda_{slit}^2} \tag{2.8}$$

Examining Eqns. 2.6, 2.7, and 2.8, the relationships between the primary spectrometer variables and the resolution can be seen clearly. As the slit width is decreased, the FWHM is also decreased, which is equivalent to saying that the resolution is increased. Also as the groove density n, size of the grating, and exit arm length L_B are all increased, the resolution is increased.

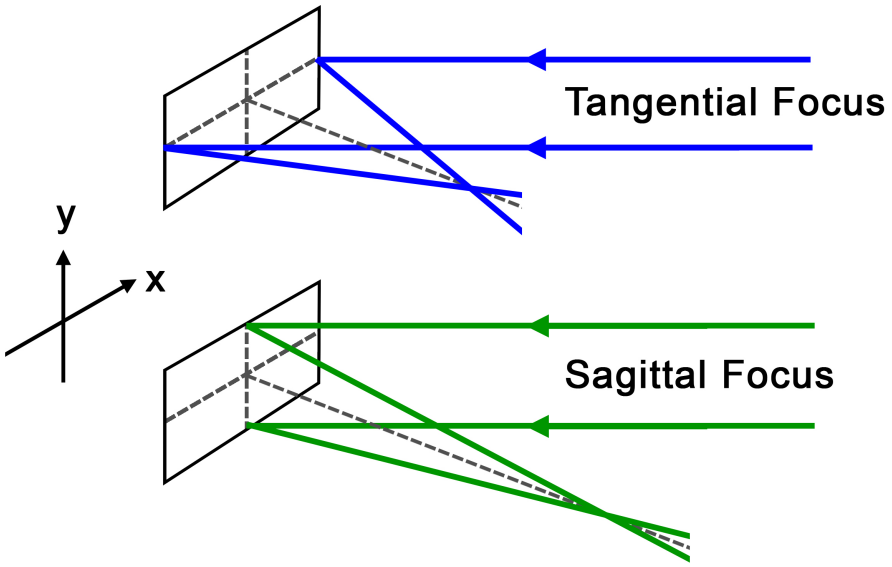

Figure 2.7: Definition of tangential focus and sagittal focus. In a spectrometer with astigmatism, the two focal points have different locations.

Astigmatism

All Czerny-Turner spectrometers with spherical mirrors will have some degree of astigmatism. This is when the spectral focal plane, the tangential focus located along the x-axis, is at a different location than the spatial focal plane, the sagittal focus located along y-axis [32]. A visual definition and example of the astigmatism is shown in Fig. 2.7. The astigmatism is caused by off axis geometry of the spectrometer, with a plane wave incident on a spherical mirror. The severity of the astigmatism increases with the square of the spectrometer's numerical aperture and the square of the off axis angle [32].

For most applications the spatial focus is not very important, and no efforts are made to correct the aberration. The main effect of this astigmatism at the spectral focal plane is a spreading of light in the spatial dimension (along the y-axis). While the spectral resolution will remain as it should, the intensity of

the signal at a given point will be decreased. This reduced intensity can lead to signal-to-noise problems if the spectrum is already dim.

In the experiments in this thesis, several independent spectra are to be recorded simultaneously using a single spectrometer by the use of a linear array of fibers. Therefore the vertical blending of the independent spectra due to the astigmatism would negate the spatial resolution provided by the fibers. The astigmatism can be corrected two ways. The first is in the design of the spectrometer by using toroidal mirrors instead of spherical mirrors [32]. The second is to install an aftermarket cylindrical lens into the optical system that will move the sagittal focal point to the tangential focal point.

In the data presented in this thesis, the λ Minutemen spectrometer was modified through the use of a cylindrical mirror to correct the astigmatism. Conversely, the Andor spectrometer was designed with toroidal mirrors and needed no modifications to be used in the desired manner in these experiments.

2.2.4 Gated ICCD Cameras

The spectra were recorded using a gated intensified charge-coupled device (ICCD) designed for use in the optical region of the spectrum. An ICCD is essentially a micro-channel plate (MCP) that has been coupled to a CCD camera for recording the data. The MCP is a type of gated imager which intensifies a light signal over a small time window of tens of nanoseconds in these experiments.

A MCP has a fairly straightforward principle of operation. Incident light strikes a photocathode which then converts the photons to electrons via the pho-

toelectric effect. The electrons are then accelerated through fine capillaries by a large bias voltage. In these capillaries the accelerated electrons are multiplied as a result of collisions with the capillaries, which provides the desired gain in signal. The electrons then strike a phosphor upon reaching the end of the capillary and are converted back to photons and captured in the pixel wells of a coupled CCD. The signal can then be read out of the CCD and the data analyzed.

The very fast gating of these devices is achieved through the capillary voltage bias. Electrons are accelerated and multiplied only when the voltage is applied. Therefore the short gating window requires a very short and high voltage pulse.

One important feature of an ICCD is the size of the capillaries. It is often the case that they are $\sim 25\mu m$, as it is very difficult to make them smaller yet function properly with a large gain. When coupled with a spectrometer, they have the impact of reducing the system resolution, typically by a factor of 2. There is usually no loss in resolution from the transition from the capillaries to the charge-coupled device (CCD) that records the data, because the CCD pixels are typically much smaller. For the Andor iStar ICCD used in these experiments, each CCD pixel was $13.5\mu m$ by $13.5\mu m$.

2.3 Experimental Arrangements

Three difference experimental arrangements were used to collect the data presented in this thesis. In all three setups, the light from the exploding wire was transferred to the spectrometer through fiber optics. The emitted visible radiation from the plasma was imaged onto a coherent linear fiber array consisting

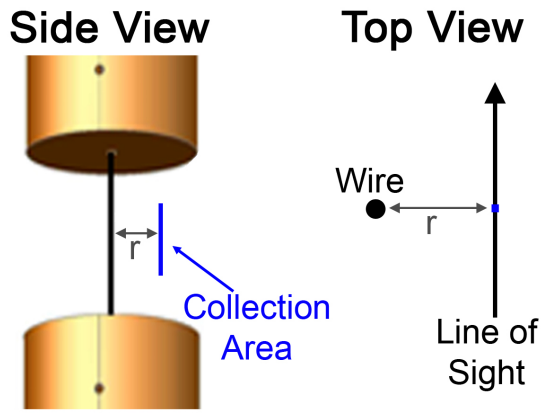

Figure 2.8: The field of view near the exploding wire used in the GOI setup. Side view showing the integration over focal points spaced vertically parallel to the wire and a distance of r away from the original wire position. Top view of the wire showing the line of sight of the collecting optics.

of 17 fibers, each with a core diameter of 100μm and a numerical aperture (NA) of 0.12. This is half the NA of a standard fiber, which means that it has a smaller light cone and angle of light acceptance. The fiber centers were spaced 122μm from each other, on both ends. In the GOI setup, the fibers were aligned to integrate over a large vertical area at a single radial distance, as shown in Fig. 2.8. In the PIMax3 and Andor experimental setups, the fiber was aligned to look radially across the exploding wire to sample light from 17 different points each at a different radius in the plasma, as depicted in Fig. 2.9. This provided the spatial resolution in the spectra.

The magnification between the plasma and the fiber was varied over the experiments to change the amount of spatial averaging. Most experiments had either $1:1$ or $1:2$ imaging, so that each fiber sampled a region of 100μm to 200μm at the focal point. It should be pointed out that the line of slight did not limit the collection area to only the focal point. For each spectrum, the light was collected and integrated along an entire chord along the line of sight. Because

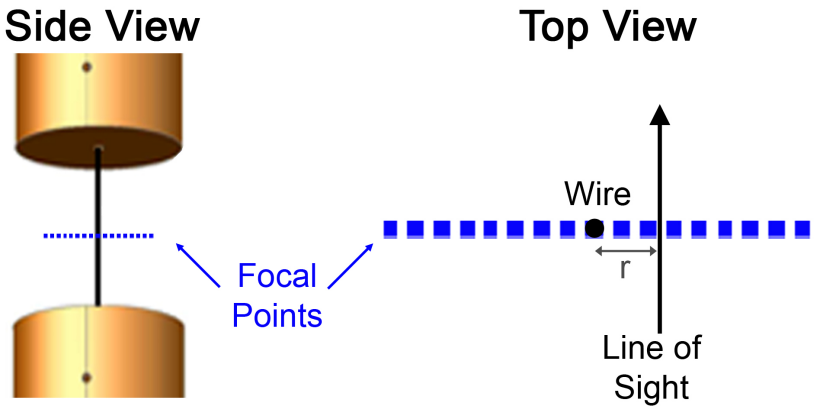

Figure 2.9: The field of view near the exploding wire. Side view showing the focal points spaced radially perpendicular to the original wire position. Top view of the wire showing the line of sight of the collecting optics.

the plasma expanded radially outwards, the length of the chord through the plasma decreases as the focal point moves farther away radially from the original wire position. Likewise, the sample points nearest the original wire position have the longest chords and integrate through the most plasma.

2.3.1 GOI Setup

The first experimental setup is shown in Fig. 2.10 and was used for the initial exploratory experiments presented in Sec. 5.1. Light from the plasma was focused into the linear fiber array aligned parallel to the wire so that spectra were collected over a large vertical area and a narrow radial area. The light signal was integrated over all of the fibers (after recording the data) resulting in one spectrum per experiment. The fiber alignment and field of view is shown in Fig. 2.8.

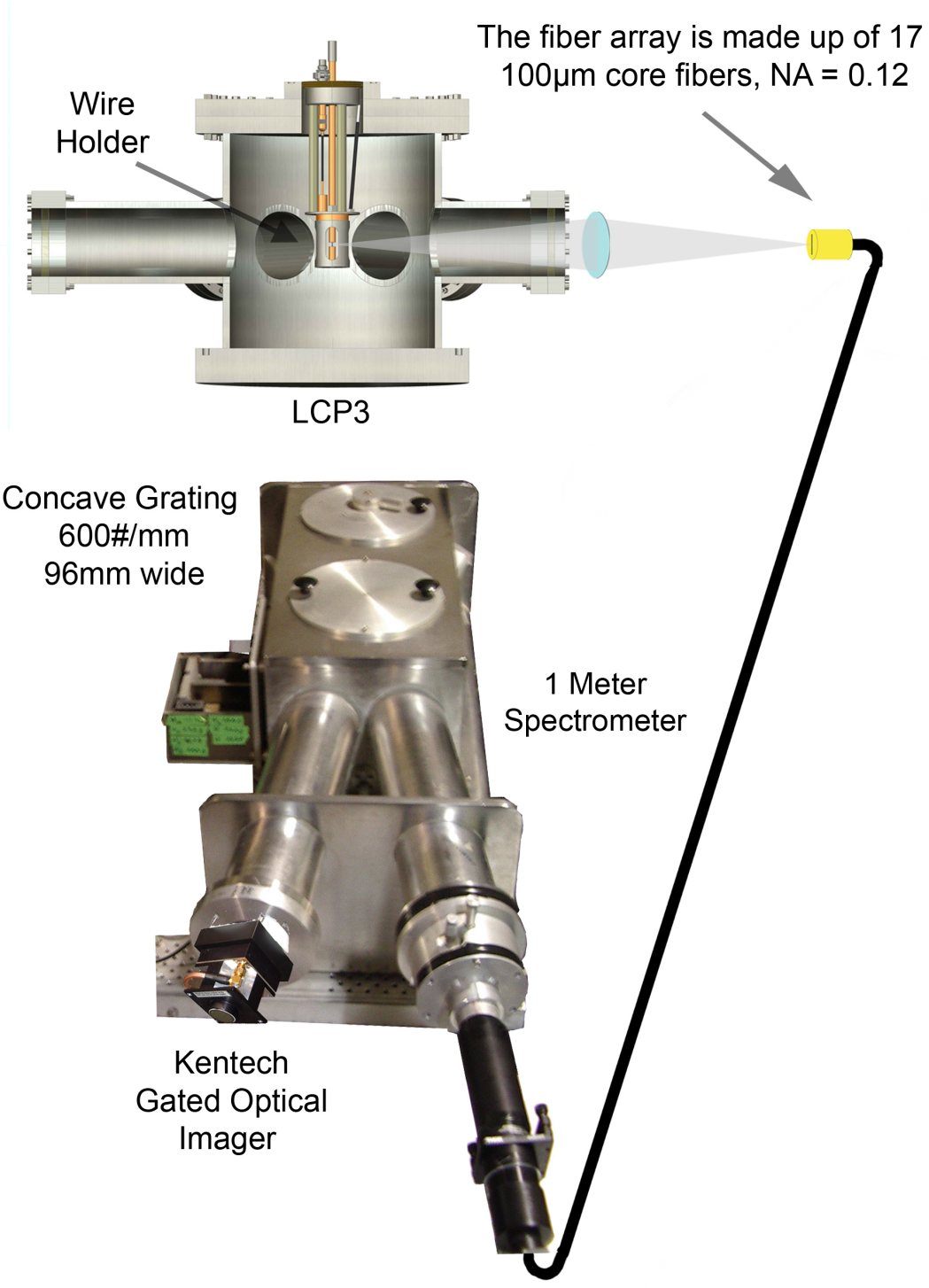

Figure 2.10: The Kentech gated optical imager (GOI) setup. This one included a 1 meter concave grating spectrometer and a Kentech GOI. The system resolution was 3.2$\mathring{A}$ because of the GOI's 10$lpmm$ resolution.

The light from the fiber array was then focused onto the entrance slit of a 1 meter spectrometer with a concave grating with $600 grooves/mm$. The grating was the only element to focus the light while dispersing it. The spectrum was intensified by a Kentech gated optical imager (GOI) borrowed from Sandia National Laboratories. The GOI acted only to intensify and gate the spectrum. The integration time determined by the gate was $12 ns$. Therefore it was necessary to couple it to a camera to record the spectra. The resolution of this system was $3.2 Å$, limited by the GOI's $10 lpmm$ (line pairs per millimeter) resolution.

2.3.2 PIMax3 Setup

The second setup is shown in Fig. 2.11. Light was focused into the fibers by a compound camera lens. The fiber was aligned to collect spectra radially, as shown in Fig. 2.9. The light from the fiber was then focused into a λ Minuteman 1/2 meter spectrometer with a $2160 grooves/mm$. This spectrometer had a significant amount of astigmatism that was corrected using a cylindrical lens. It was placed before the compound camera focusing lens, seen in the picture in Fig. 2.11 just behind the PIMax3 camera, which imaged the fiber array onto the slit of the spectrometer.

While the optics setup corrected the majority of the astigmatism, it was not perfect and there was some "cross-talk" between the fiber signals. This is when the edges of the individual fiber signals slightly overlapped. To accommodate for this, the low intensity edge rows of each spectrum were not included in the summation of the final fiber spectra. While this did result in some elimination of signal, the resulting spectra had less contamination.

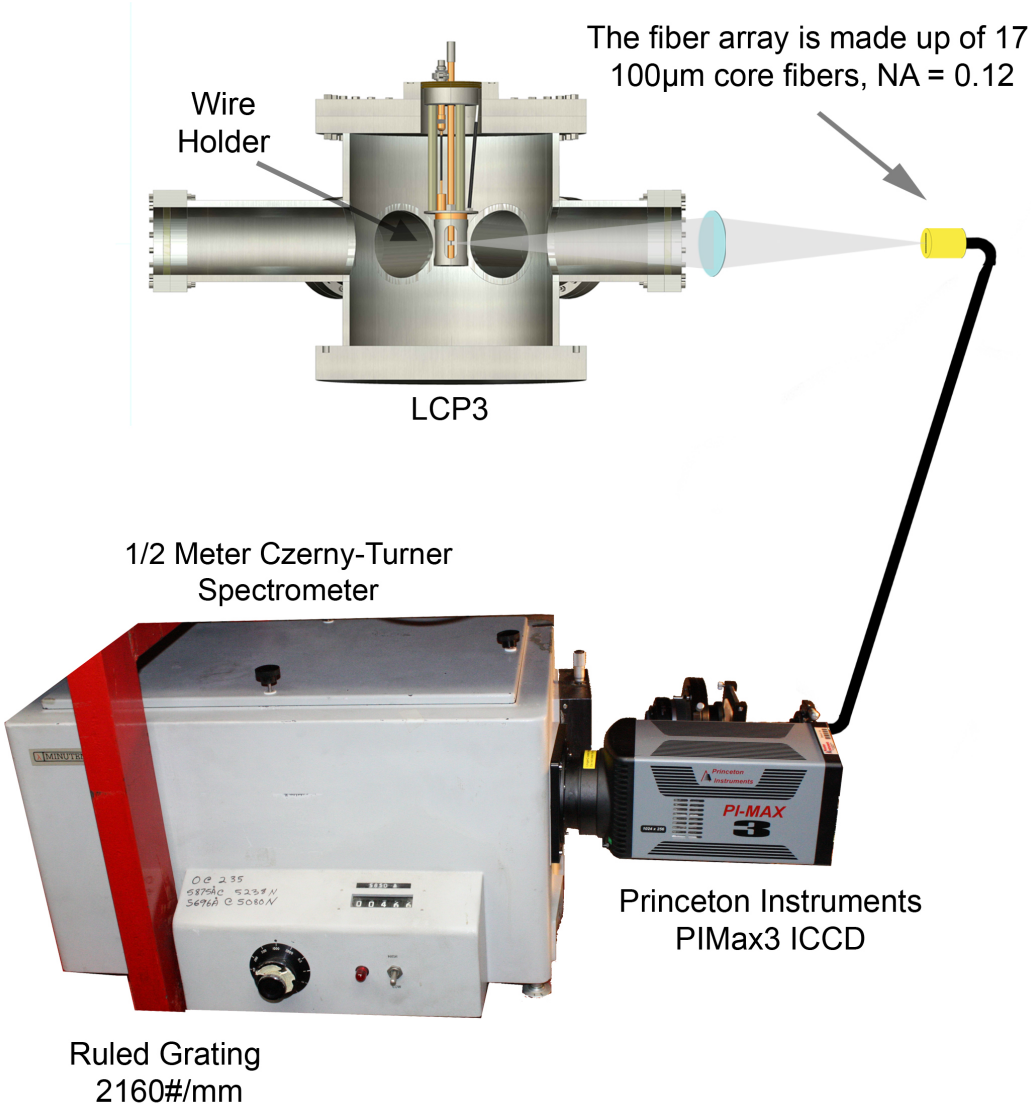

Figure 2.11: The PIMax3 setup. It included a 1/2 meter Czerny-Turner spectrometer and a Princeton Instruments PIMax3 gated ICCD. The system resolution with the 2160*grooves*/*mm* grating was 0.75$\mathring{A}$.

A gated ICCD camera was mounted on the exit plane of the spectrometer to record the spectra. This ICCD was a Princeton Instruments PIMax3 camera borrowed as a ”demo” from the company. The final resolution with the camera and the 2160$grooves/mm$ grating was 0.75$\mathring{A}$. The resolution was limited by the focal length and incident angles of the spectrometer. The time gate width used was 100ns. The data collected with the PIMax3 setup is presented in Sec. 6.1 and was used to determine electron densities and the magnitude of the magnetic field at a particular radial position.

2.3.3 Andor Setup

The third setup is shown in Fig. 2.13. In the previous configurations, the wire load was located in the center of the LCP3 chamber, which has an 11.5 inch (292.1 mm) diameter. In order to decrease the distance between the wire and one of the viewing ports, i.e., increase the solid angle of light collection, one of the LCP3 ports was shortened by 2.5 inches (63.5 mm). Additionally hardware was designed to offset the wire holder by 2 inches (50.8 mm) from the center of the chamber. The combined effect of these changes was to increase possible light collection by 170%, or a factor of 2.7.

The same collecting optics and linear fiber bundle was used, aligned radially as shown in Fig. 2.9 to collect simultaneous spectra as a function of radial position. The fiber bundle was placed directly at the entrance slit of an Andor Shamrock 1/2 meter imaging Czerny-Turner spectrometer borrowed from the company as a ”demo”. The spectra were recorded with a ”demo” Andor iStar gated ICCD.

Even though the spectrometer was an imaging spectrometer, there was still some astigmatism which caused the closely spaced spectra to overlap slightly creating ”cross-talk” between the fiber signals. As in the Princeton Instruments PIMax3 setup, the low intensity edge rows of each spectrum were not included in the summation of a final fiber spectrum. While this did result in some reduction of signal, the resulting spectra had less contamination. Shown as the blue curve in Fig. 2.12 is the ”vertical” signal intensity over signals from four fibers in shot 1601, integrated over five pixels on the wavelength axis. A Gaussian curve is fit to each of the fiber signals, and the resulting curve is shown in red. Two Gaussian fits to individual fibers are graphed in black to show the fiber signal

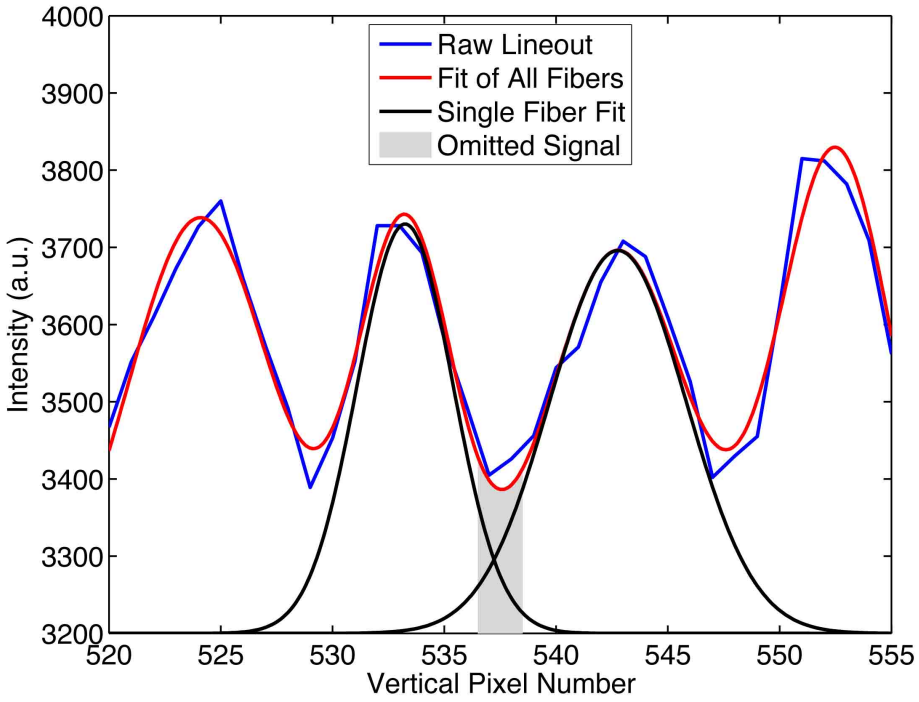

Figure 2.12: The "vertical" signal intensity over signals from four fibers shown in blue. A Gaussian curve is fit to each of the fiber signals, and the resulting curve is shown in red. Two Gaussian fits to individual fibers are graphed in black to show the fiber signal overlap. The gray shaded region represents the pixels omitted from the final spectra.

overlap. The gray shaded region represents the pixels omitted from the final spectra. While not all of the signal contamination is eliminated, it is reduced significantly. At the peak intensity pixel, the cross-talk is $\leq 2.5\%$ of the original signal. At the edge pixel of the fiber signal, the cross-talk can raise the intensity by $\leq 16\%$. Over the entire summed fiber area, the cross-talk from one adjacent fiber could be $\leq 2\%$. Therefore, after omitting the pixels between fibers with the most cross-talk, at most $\leq 4\%$ of a summed spectrum could be from adjacent fibers.

Two different grating were used in the Andor spectrometer. One was a

$300 grooves/mm$ grating that provided a spectral bandwidth of $\sim 900 Å$ and a resolution of $7.0 Å$. For this resolution, a $50 ns$ gate time was used. The data was used to determine electron densities and electron temperatures and is presented in Sec. 5.2.

The other grating used was a $2400 grooves/mm$ giving a resolution of $0.6 Å$ over a $100 Å$ bandwidth. Due to the larger dispersion, a $100 ns$ gate time was needed to collect enough signal. The data taken with this grating were used to look for evidence of measurable magnetic fields and determine electron densities, and is presented in Sec. 6.2.

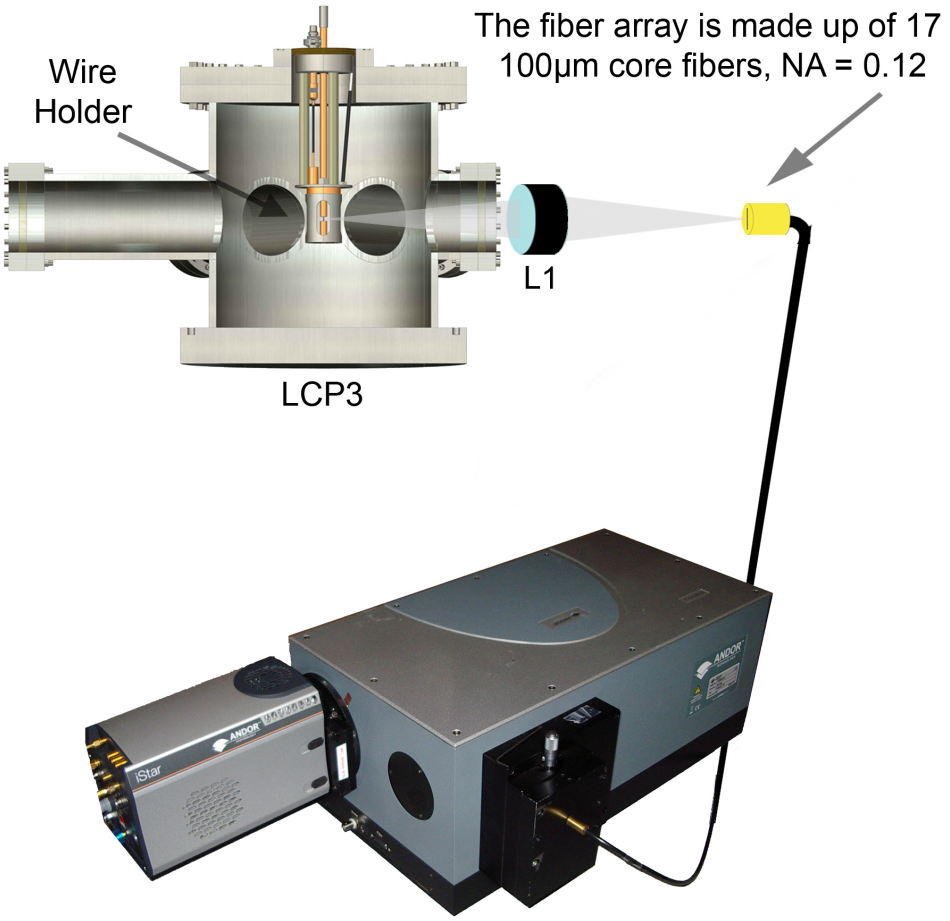

Figure 2.13: The Andor system setup. It included an imaging 1/2 meter Czerny-Turner spectrometer and an Andor iStar gated ICCD.

CHAPTER 3

PLASMA RADIATION

Many types of plasmas can exist, and the plasma parameters, such as material, ionization, electron temperature, ion temperature, and electron density, can vary significantly. Over all of the ranges for these parameters, the plasma will emit radiation. The emitted radiation can include continuum radiation and characteristic radiation. Most of the continuum radiation in a plasma comes from two types of transitions, free-free transitions (bremsstrahlung) and free-bound transitions (radiative recombination). Characteristic, or line, radiation is comprised of bound-bound transitions (de-excitation). From studying the particulars of the emitted radiation, both continuum and characteristic, one can determine an abundant amount of information about the plasma. In order to determine this information, the processes involved in emitting the radiation must be well understood. The analysis of the spectra in this thesis will focus on emitted line radiation; however, a brief description of continuum radiation is given to provide a description of plasma radiation as a whole.

3.1 Continuum Radiation

The two main sources of continuum radiation are from free-bound and free-free transitions in the form of radiative recombination and bremsstrahlung, respectively. While often considered separately, bremsstrahlung is closely related to radiative recombination. Quantum mechanically, bremsstrahlung corresponds to transitions between continuum states. It is derived by taking a different limit in the radiative recombination derivation between bound and continuum states.

Non-radiative recombination also plays a role in the plasma dynamics and is important in determining how long the plasma takes to reach a steady state. While included in the steady state calculations presented in Sec. 5.2, these transitions do not radiate and will not be discussed in detail.

Radiative Recombination

Radiative recombination is the process of an ion capturing a free electron. This changes the charge state of the ion and is accompanied by emission of a photon. The process, along with energy conservation, can be represented as

$$A^{z+1}(g) + e^- \rightarrow A^z(q) + \gamma \tag{3.1}$$

$$E_{free} = [E(q) - E(\infty)] + h\nu_\gamma \tag{3.2}$$

where $A^{z+1}(g)$ is the ion of charge $z+1$ in its ground state, $A^z(q)$ is the ion with the captured electron in the excited level q, γ is the emitted photon, E_{free} is the starting energy of the free electron, $E(q)$ is the energy of the excited level q, $E(\infty)$ is the energy of the ionization limit, $[E(q)-E(\infty)]$ is the ionization energy of state q, and $h\nu_\gamma$ is the energy of the emitted photon.

In radiative recombination, one could think of the process as a deexcitation of an electron from an upper state to a lower state, with the upper state being in the continuum. One very important feature of the free-bound cross-sections is that they must cross the ionization barrier to connect continuously with the bound-bound cross-sections. More details on this can be found in [13, 31].

Recombination rates, cross-sections, and the emissivity of radiative recombination are closely related to their photoionization counterparts. The Milne relation in Eqn. 3.3 gives the relationship between the recombination cross-section

$\sigma_{z+1}(E_{free} \rightarrow q, \nu)$ and the photoionization cross-section $\sigma_z(q \rightarrow E_{free}, \nu)$ [31].

$$\sigma_{z+1}(E_{free} \rightarrow q, \nu) = \frac{g_z(q)}{g_{z+1}(g)} \frac{1}{2m_e c^2} \frac{(h\nu)^2}{E_{free}} \sigma_z(q \rightarrow E_{free}, \nu) \tag{3.3}$$

The terms $g_{z+1}(g)$ and $g_z(q)$ are the statistical weights of the levels.

The photoionziation cross-section $\sigma_z(q \rightarrow E_{free}, \nu)$ most commonly used is the semiclassical Kramers cross-section in Eqn. 3.5 multiplied by the free-bound Gaunt factor $G^{bf}_{n_q}(\nu)$ to correct for quantum effects [13, 31]. It is derived for hydrogenic ions with an initial principal quantum number, n_q, averaged over the momentum states l.

$$\sigma_z(q \rightarrow E_{free}, \nu) = \sigma^{Kr}_z(q \rightarrow E_{free}, \nu) * G^{bf}_{n_q}(\nu) \tag{3.4}$$

$$\sigma^{Kr}_z(q \rightarrow E_{free}, \nu) = \frac{64\alpha}{3\sqrt{3}} \frac{Z^4}{n_q^5} \left(\frac{E_R}{h\nu}\right)^3 \pi a_0^2 \quad \text{with} \quad \nu \geq \nu_{n_q \infty} \tag{3.5}$$

In Eqn. 3.5, $\alpha \approx 1/137$ and is the fine-structure constant, $a_0 \approx 0.53\mathring{A}$ and is the Bohr radius, E_R is the Ryberg energy defined as $E_R = (m_e e^4)/(8\epsilon_0^2 h) = 13.606eV$, and Z is the ion charge which is also the atomic number (and charge of the nucleus because this is only for hydrogenic ions with one electron that is captured in the recombination).

Assuming a Maxwellian energy distribution (which is appropriate for a high collisional frequency), the emission coefficient for hydrodgenic ions is $\varepsilon^{fb}_\nu(\nu)$ with units of $[Ws\ sr^{-1}m^{-3}]$, given in Eqn. 3.6 below, using the photoionziation cross-section $\sigma_z(q \rightarrow E_{free})$ in Eqn. 3.4 [31].

$$\varepsilon^{fb}_\nu(\nu) = \frac{h^4\nu^3}{(2\pi m_e)^{3/2}c^2} \frac{n_{z+1}(g)n_e}{(k_B T_e)^{3/2}} \exp\left(-\frac{h\nu}{k_B T_e}\right)$$
$$\times \sum_{q \geq q_{min}} \frac{g_z(q)}{g_{z+1}(g)} \exp\left(\frac{E(q) - E(\infty)}{k_B T_e}\right) \sigma_z(q \rightarrow E_{free}) \tag{3.6}$$

Plugging the Gaunt corrected Kramer's cross-section for the photoionization cross-section in Eqn. 3.6 leads to Eqn. 3.7 for hydrogenic emission in terms of

wavelength using $\varepsilon_\lambda = \varepsilon_\nu c/\lambda^2$; the units are $[Wsr^{-1}m^{-4}]$ [20].

$$\varepsilon_\lambda^{fb}(\lambda) = \frac{64\sqrt{\pi}c(\alpha a_0)^3 E_R}{3\sqrt{3}} n_Z n_e Z^4 \left(\frac{E_R}{k_B T_e}\right)^{3/2} \frac{1}{\lambda^2} \exp\left(-\frac{hc}{\lambda k_B T_e}\right) \times \sum_{n_q \geq n_{q_{min}}} \frac{1}{n_q^3} \exp\left(\frac{Z^2 E_R}{n_q^2 k_B T_e}\right) G_{n_q}^{bf}(\lambda) \tag{3.7}$$

The $1/n^3$ term in Eqn. 3.7 means that recombination into the ground state will be the strongest component. It can also be shown from Eqn. 3.7 that at short wavelengths the emission will be dominated by the $\exp(-hc/\lambda k_B T_e)$ term, and at long wavelengths the $1/\lambda^2$ term dominates.

To solve Eqn. 3.7, Griem [22] splits the summation into two parts. One part is from $n_{q_{min}}$ to n'_q. The other part is for $n'_q + 1$ and above, where the atomic energy levels are so close that they can be approximated by continuum and an integral. The original summation is over all levels; therefore, the integration will go to infinity. In this context, infinity is the ionization limit.

$$\begin{aligned} \sum_{n_q \geq n_{q_{min}}} \frac{1}{n_q^3} \exp\left(\frac{Z^2 E_R}{n_q^2 k_B T_e}\right) \quad &\Rightarrow \quad \int_{n'_q+1}^{\infty} \frac{1}{n^3} \exp\left(\frac{Z^2 E_R}{n_q^2 k_B T_e}\right) dn_q \\ &= -\frac{k_B T_e}{2Z^2 E_R} \int_{\frac{Z^2 E_R}{(n'_q+1)^2 k_B T_e}}^{0} \exp(x) dx \\ &= \frac{k_B T_e}{2Z^2 E_R} \int_{0}^{\frac{Z^2 E_R}{(n'_q+1)^2 k_B T_e}} \exp(x) dx \end{aligned} \tag{3.8}$$

For other types of ions with charge states other than hydrogen-like, the photoionization cross-section can be determined experimentally (or calculated numerically for all levels of a specific ion) and then applied in Eqn. 3.6. Another approach is to apply the Biberman correction factor $\xi^{bf}(z, T_e, \lambda)$ to the hydrogen-like emission coefficient, in a similar manner used previously for the Gaunt factor [22]. The Biberman factor takes into account the energy levels of the final ion, and produces a good approximation with the correct ionization

edges [22, 13, 31].

Bremsstrahlung

Bremsstrahlung is often described classically as the deflection of electrons in a Coulomb potential that causes a deceleration and emission of radiation. The process and electron energy conservation can be written as

$$A^z + e^- \rightarrow A^z + e^- + \gamma \tag{3.9}$$

$$E_{free} = E'_{free} + h\nu_\gamma \tag{3.10}$$

where E_{free} is the starting energy of the free electron, E'_{free} is the final energy of the free electron, $h\nu_\gamma$ is the energy of the emitted photon γ, and A^z is an ion with charge z.

To derive the emission coefficients for bremsstrahlung radiation, we start at Eqn. 3.7. Examining closely the integral portion for the free-bound transitions in Eqn. 3.8, we see that to consider transitions between free states we need only to change the limits of integration. Integrating from $x = Z^2 E_R/(n'_q + 1)^2 k_B T_e$ (which is positive) down to $x = 0$ (or $n_q \rightarrow \infty$), gives transitions into bound states at the ionization limit. Therefore integrating from the ionization limit at $x = 0$ and below to $x = -\infty$, results in transitions between continuum states [31]. Therefore, the bremsstrahlung emission coefficient in a fully ionized plasma is

$$\varepsilon_\lambda^{ff}(\lambda) = \frac{32\sqrt{\pi}c(\alpha a_0)^3 E_R}{3\sqrt{3}}\, n_Z\, n_e\, Z^2 \left(\frac{E_R}{k_B T_e}\right)^{1/2} \frac{1}{\lambda^2} \exp\left(-\frac{hc}{\lambda k_B T_e}\right) G^{ff}(T_e, \lambda). \tag{3.11}$$

In a similar manner as before, the bremsstrahlung due to ions that are not fully stripped in a Maxwellian plasma is found by replacing the free-free Gaunt factor $G^{ff}(T_e, \lambda)$ with the free-free Biberman factor $\xi^{ff}(z, T_e, \lambda)$. In a plasma

with many ion species, the contributions to the total bremsstrahlung are additive, and the emission coefficient is modified simply by a summation over ion species.

$$\varepsilon_{\lambda}^{ff}(\lambda) = \frac{32\sqrt{\pi}c(\alpha a_0)^3 E_R}{3\sqrt{3}} n_e \left(\sum_{i,z} n_{i,z} z_i^2\right) \left(\frac{E_R}{k_B T_e}\right)^{1/2} \frac{1}{\lambda^2} \exp\left(-\frac{hc}{\lambda k_B T_e}\right) \xi^{ff}(T_e, \lambda). \quad (3.12)$$

For an optically thin plasma, the wavelength with the highest intensity is given by λ_{max}.

$$\lambda_{max} = \frac{hc}{2k_B T_e} \quad (3.13)$$

3.2 Characteristic Radiation

Within an atom or ion, a bound electron can transition between two bound energy levels. When an electron transitions from a higher energy level to a lower one, radiation is emitted with energy that corresponds to the difference in energy between the two levels. This is called line or characteristic radiation.

For a transition from an upper state k to a lower state i, a photon is emitted with a frequency ν_{ki} that is dependent on the difference between the energy levels.

$$\nu_{ki} = \frac{E_k - E_i}{h} \quad (3.14)$$

The photon frequency ν_{ki} is related to the wavelength by the speed of light: $\nu = c/\lambda$.

There are many types of stimuli for a bound-bound transition, either exciting from a lower to higher state, or deexciting from a higher to lower state. They include spontaneous emission, induced emission by electromagnetic waves, and induced absorption by electromagnetic waves, among others.

For a spontaneous transition between the two states, the decay rate of the upper state is proportional to the density of the species in the upper state N_k and an emission probability constant A_{ki} called the Einstein A coefficient for spontaneous emission given in units of inverse seconds, s^{-1}.

$$-\frac{dN_k}{dt}\Big|_{k\to i} = A_{ki}\, N_k \tag{3.15}$$

The Einstein A coefficient is the quantum mechanical probably that an electron in a given state will transition to a particular lower state in a unit time.

For a plasma with many excited ions with electrons in the upper state k, the spontaneous emission coefficient for a given line is Eqn. 3.16, with units of $[Wm^{-3}sr^{-1}Hz^{-1}]$. The new term, $\mathcal{L}(\nu)$, is called the line profile function. It is there because the line transitions are not truly a delta function.

$$\varepsilon_{\nu,ki} = \frac{h\nu_{ki}}{4\pi}\, A_{ki}\, N_k\, \mathcal{L}(\nu) \tag{3.16}$$

The integrated intensity I_{ki} for a given transition is determined from the emissivity by integrating over the path length and frequency (i.e. the line profile function).

$$I_{ki} = \iint \varepsilon_{\nu,ki} d\nu dx \tag{3.17}$$

The resulting equation for the integrated intensity I_{ki} of the k to i transition due to spontaneous emission is given in Eqn. 3.18 with units of $[Wm^{-2}sr^{-1}]$.

$$I_{ki} = \frac{h\nu_{ki}}{4\pi} A_{ki}\, N_k\, L \tag{3.18}$$

Here $h\nu_{ki}$ is the photon energy, N_k is the population density of the upper level k, and A_{ki} is the Einstein coefficient for spontaneous emission. The population density function for N_k can range from being complicated to simple depending on the plasma conditions. The most simple and well understood cases are for equilibrium conditions, such as thermodynamic equilibrium.

Emission of a photon can also be induced by an electromagnetic field, and the change in population density due to induced emission is given in Eqn. 3.19. Here B_{ki} is the Einstein coefficient for stimulated emission and u_ν is the spectral radiant energy density of the electromagnetic field interacting with the particle.

$$-\frac{dN_k}{dt}\Big|_{k\to i} = B_{ki}\, N_k\, u_\nu \tag{3.19}$$

The Einstein B coefficient for induced emission was discovered (by Einstein) because another process was needed to derive Plank's law in thermodynamic equilibrium [39].

The other more frequently encountered Einstein B coefficient is the B coefficient for absorption of a photon from an electromagnetic field, B_{ik} [39, 31]. In this process, a photon is absorbed by the electron, which is excited from a lower state i to an upper state k. The change in the population density of the lower state N_i is proportional to the population density of the lower state N_i, u_ν is the spectral radiant energy density, and the B coefficient for absorption is B_{ik}.

$$-\frac{dN_i}{dt}\Big|_{i\to k} = B_{ik}\, N_i\, u_\nu \tag{3.20}$$

The induced absorption and induced emission are both relevant for opacity determinations. Perhaps initially surprising, induced emission is included in opacity and absorption calculations, instead of emission calculations.

Due to the Heisenberg uncertainty principle that states $\Delta E \Delta t \geq \hbar/2$, there exists uncertainty in the actual value of the energy levels. This leads to a slight "width" in the energy levels, which in turns leads to a distribution of frequencies for a given transition between two levels. When not compounded by other factors (such as high density or particle movement), this result is the "natural" line shape which has a finite width. No matter the units, the line shape is de-

fined to integrate to a value of 1.

$$\int_{line} \mathcal{L}(\omega)d\omega = 1 \quad \int_{line} \mathcal{L}(\nu)d\nu = 1 \quad \int_{line} \mathcal{L}(\lambda)d\lambda = 1 \tag{3.21}$$

The natural line shape is Lorentzian, and typically the line width is very small. As written in Eqn. 3.22, the parameter β_L is the full width at half max (FWHM) and ω_0 is the central line position.

$$\mathcal{L}_L(\omega) = \frac{\beta_L}{2\pi} \frac{1}{(\omega - \omega_0)^2 + (\beta_L/2)^2} \tag{3.22}$$

A derivation of the Lorentzian profile as the natural line profile can be found in Griem's textbook [22]. For the experiments in this thesis, the natural line shape can be neglected compared to other broadening mechanisms because it is smaller by a order of magnitude.

Another function commonly encountered in spectroscopy is the Gaussian line profile, given in Eqn. 3.23:

$$\mathcal{L}_G(\omega) = \frac{2\sqrt{\ln 2}}{\sqrt{\pi}} \frac{1}{\beta_G} \exp\left[-4\ln 2 \left(\frac{\omega - \omega_0}{\beta_G}\right)^2\right] \tag{3.23}$$

Similarly, β_G is the FWHM of the line and ω_0 is the central line position. The odd looking factors of $\ln 2$ in this expression of a Gaussian distribution come from using the FWHM β_G instead of the more common variance σ.

The line profile due to a spectrometer's response is Gaussian, with a much larger FWHM than the natural line width, so much so that the line profile is dominated by a Gaussian and the Lorentzian component can be neglected. Line broadening due to the thermal Doppler effects is also Gaussian. In contrast, line broadening due to density or magnetic field has a Lorentzian profile. This will be discussed in greater detail in Chapter 4.

Where there are several broadening mechanisms and types of profiles influencing the line shape, the resulting line shape will be a convolution of the contributing profiles. Keep in mind that convolving two or more Gaussian profiles results in a Gaussian with a new FWHM $\beta_{G,new}$,

$$\beta_{G,new} = \sqrt{\beta_{G,1}^2 + \beta_{G,2}^2}. \tag{3.24}$$

When convolving two or more Lorentzians, the resulting profile will also be Lorentzian with a new FHWM $\beta_{L,new}$ that is the sum of the contributing FWHMs.

$$\beta_{L,new} = \beta_{L,1} + \beta_{L,2} \tag{3.25}$$

When convolving a Lorentzian with a Gaussian, the result is not as simple or neat. The new profile function is called a Voigt profile $\mathcal{L}_V$ and must be determined numerically:

$$\mathcal{L}_V(\omega) = \int_{-\infty}^{\infty} \mathcal{L}_L(\omega - \Delta\omega)\mathcal{L}_G(\Delta\omega)d\Delta\omega \tag{3.26}$$

$$\mathcal{L}_V(\omega) = \frac{2\ln 2}{\pi^{3/2}}\frac{\beta_L}{\beta_G^2}\int_{-\infty}^{\infty} \frac{\exp\left(-y^2\right)}{\left(\frac{2\sqrt{\ln 2}(\omega-\omega_0)}{\beta_G} - y\right)^2 + \ln 2\left(\frac{\beta_L}{\beta_G}\right)^2} dy \tag{3.27}$$

The resulting Voigt FWHM is not a simple combination of the constituent profile FWHMs. However, the following approximation that is accurate to about 1% can be made [51].

$$\beta_V \approx \frac{\beta_L}{2} + \sqrt{\left(\frac{\beta_L}{2}\right)^2 + \beta_G^2} \tag{3.28}$$

As the experimental line profile measurements are used to determine information about the plasma, the relation in Eqn. 3.28 will be extremely useful. In these experiments, the major Gaussian contributor to the experimental line shape was from the spectrometer's line profile, which was independently measured. Using Eqn. 3.28, the Lorentzian width can be quickly determined and, for

the experiments discussed in this thesis, relates directly to the electron density of the plasma. This will be further discussed in Sec. 4.2.

CHAPTER 4

SPECTROSCOPIC MEASUREMENT TECHNIQUES

As the plasma parameters vary, the type and intensity of the emitted radiation changes. By studying the spectra of the emitted radiation, we are able to determine information about the plasma that emitted the radiation.

4.1 Magnetic Fields

Within an atom, orbiting bound electrons produce an internal magnetic field. This has the effect of creating spin-orbit (SO) splitting of energy states in the atom, which is referred to as the fine structure of the atomic energy levels. With the application of an external magnetic field, the degeneracy of the sub-levels is lifted and an additional splitting of energy levels is observed.

4.1.1 Zeeman Splitting

For external magnetic fields, the effect of which is less than the SO interaction, the level spitting due to the magnetic field is linear. If the magnetic field is very large (much larger than those in this thesis), the effect will overcome the SO coupling and the quadratic Zeeman effect must be considered. This will not be discussed in this thesis, but more information can be found in Cowan's book [13].

With an external magnetic field, each level, with total angular momentum number J, will split into $2J + 1$ levels, each with a different quantum magnetic momentum number M. The energy shift of the levels can be expressed by the

addition of the magnetic interaction term H_{mag} to the atom's Hamiltonian:

$$H_{mag} = -\mathbf{B} \cdot \mu. \tag{4.1}$$

The magnetic field vector is **B**, and μ is the intrinsic magnetic moment of the atom. The latter is comprised of the Bohr magnetron μ_B, the anomalous gyromagnetic ratio for the electron $g_s \backsimeq 2.0023192 \approx 2$, the total angular momentum **J**, and the spin **S**.

$$\mu = -\mu_B[\mathbf{J} + (g_s - 1)\mathbf{S}] \tag{4.2}$$

The new Hamiltonian for the atom with an external magnetic field is given by [13].

$$H = -\sum_i \nabla_i^2 - \sum_i \frac{2Z}{r_i} + \sum_i \xi_i(r_r)(\mathbf{l_i} \cdot \mathbf{s_i}) + \sum_{\mathbf{i>j}} \sum \frac{\mathbf{2}}{\mathbf{r_{ij}}} + -\mathbf{B} \cdot \mu \tag{4.3}$$

The Schrödinger equation with this new Hamiltonian can be solved in the LS coupling approximation with the magnetic field along **z**, and the change in energy level due to the Zeeman effect ΔE_z can be expressed as

$$\Delta E_z = g_{LSJ}\mu_B MB. \tag{4.4}$$

The term g_{LSJ} is the Landé g factor, most often expressed with $g_s = 2$.

$$g_{LSJ} = 1 + (g_s - 1)\frac{J(J+1) + S(S+1) - L(L+1)}{2J(J+1)} \tag{4.5}$$

$$g_{LSJ} \backsimeq 1 + \frac{J(J+1) + S(S+1) - L(L+1)}{2J(J+1)} \tag{4.6}$$

Dipole selection rules apply with transitions allowed satisfying $\Delta M = 0, \pm 1$. When $\Delta M = 0$, the transitions are called π-components and emit only perpendicular to the magnetic field. This π emission will be linearly polarized parallel to the field (observed perpendicular to the field).

When $\Delta M = \pm 1$, the transitions are called σ-components and they can be observed from all angles. When observed perpendicular to the field, the emission is circularly polarized in the direction of the field. When observed along the field, the emission will be linearly polarized in the direction perpendicular to the field.

If the Zeeman splitting can be observed experimentally with known line transitions, it is then a simple procedure to back out information about the magnetic field. The wavelength shift between two line transitions from upper level p to a lower level q is given in Eqn. 4.7 with the units nm for λ and T for B [31].

$$\Delta\lambda_{pq} = 4.669 \times 10^{-8} \left(M_q g_{LSJ}(q, J, L, S) - M_p g_{LSJ}(p, J, L, S) \right) \lambda^2 B \qquad (4.7)$$

4.1.2 Zeeman Broadening

Introduction

When the individual splittings cannot be observed experimentally due to other broadening mechanisms, such as Stark broadening or Doppler broadening, it used to be that the limit of experimental techniques to measure magnetic fields spectroscopically was reached. In 1998, a technique based on polarization spectroscopy was introduced at the Weizmann Institute of Science [14]. This allowed information to be determined about the magnetic field when the individual Zeeman splittings were unresolvable but information about the magnetic field topology was known, and the field did not curve or change directions over the region of observation. This increased the range of configurations for which information about the magnetic field magnitude could be determined

The limitation of the Davara polarization method [14] is that the direction of the field must be known a priori to determine its magnitude. Therefore this method cannot be used if the magnetic field topology is not known, changes during the measurement, or varies along the line-of-sight. In 2007 a new technique was introduced by the same Weizmann Institute of Science group that enables magnetic field measurements with severe broadening due to other mechanisms (such as Stark, etc.) without additional information about the directionality of the magnetic field [47]. This method makes use of two fine structure lines of the same multiplet that undergo different splittings due to the magnetic filed while they are equally affected by both Stark and Doppler broadening. Therefore the only difference in the line pair is due to the magnetic field, assuming no opacity effects, except for a known difference in the two line intensities due to quantum mechanical effects. This method has been named "Zeeman Broadening".

Line Pair Selection

There are a limited number of suitable line pairs from each element for this measurement that have been identified up to now. They include the $Na-like$ $4p-4s$ multiplet, and the $Li-like$ $3p-3s$ multiplet. For this thesis, the $Na-like$ doubly ionized aluminum (Al III) multiplet was used. The multiplet has two fine structure transitions, each between the electron configurations of $2p^6 4p - 2p^6 4s$, but with different total angular momentum J. Each of the components will undergo Zeeman splittings as described in Sec. 4.1.1.

The more intense transition occurs at $5696.60\mathring{A}$ and is a transition from an angular momentum of $J = 3/2$ down to $J = 1/2$. The Einstein A coefficient of

the transition is $8.82 \times 10^7 sec^{-1}$, with a statistical weight of the upper level g_k equal to 4. The other transition is less intense and occurs at $5722.73\mathring{A}$. This is a transition that does not change the total angular momentum of the atom. The upper level $J = 1/2$, and the lower level $J = 1/2$. The Einstein A coefficient of the less intense 1/2 to 1/2 transition is $8.70 \times 10^7 sec^{-1}$, with a statistical weight of the upper level g_n equal to 2 [38].

The line intensity ratio of the 1/2 to 3/2 transition over the 1/2 to 1/2 transition is equal to 2 (if optically thin). This mainly comes from the difference in statistical weight of the upper levels of the transitions, which is $g_k/g_n = 4/2 = 2$. As discussed in Sec. 3.2, the intensity of the line radiation also depends of the Einstein A coefficient and the wavelength of the transition. For the selected line pair, these values are nearly equal for the two transitions and therefore have a small impact on the intensity ratio. The statistical weights come into the intensity equation via the population density function, which usually introduces a temperature dependance as well. If the plasma was in local thermodynamic equilibrium, Eqn 4.18, on page 61, is appropriate for the intensity ratio. The intensity ratio has no dependence on temperature since the difference between the upper energy levels of the transitions is extremely small, only $0.009934eV$.

If there is no magnetic field, then the two line transitions will have the same FWHM since they will be broadened equally by instrumental and Stark broadening. For the plasma conditions in this thesis, Doppler broadening is negligible due to low ion temperature. If there is a B field, then the upper and lower states will split, with a change in energy of the level ΔE. For the selected Al transitions, the splittings are as follows.

$$\Delta E_{S_{1/2}} = \pm 1 \mu_B B, \quad \Delta E_{P_{1/2}} = \pm 1/3 \mu_B B, \quad \Delta E_{P_{3/2}} = \pm [2/3,\ 2] \mu_B B \tag{4.8}$$

For the 1/2 to 1/2 transition at 5722.73$\mathring{A}$, the original line will be split into four with energy shifts $\Delta\hbar\omega_{S_{1/2}-P_{1/2}}$.

$$\Delta\hbar\omega_{S_{1/2}-P_{1/2}} = \pm[\ 2/3,\ 4/3\ ]\mu_B B, \quad \text{with } [\pi, \sigma] \text{ polarization} \tag{4.9}$$

The 1/2 to 3/2 transition at 5696.60$\mathring{A}$ will be split into six lines with energy shifts $\Delta\hbar\omega_{S_{1/2}-P_{3/2}}$.

$$\Delta\hbar\omega_{S_{1/2}-P_{3/2}} = \pm[\ 1/3,\ 1,\ 5/3\ ]\mu_B B, \quad \text{with } [\pi, \sigma, \sigma] \text{ polarization} \tag{4.10}$$

The intensity of each split line is discussed in detail in Cowan's book [13], and is proportional to the square of the Wigner 3-j symbol with J and M corresponding to the lower state and J' and M' corresponding to the upper state.

$$I \propto \begin{pmatrix} J & 1 & J' \\ -M & M - M' & M' \end{pmatrix}^2 \tag{4.11}$$

Appendix C in Cowan book provides limited tabulated results for the Wigner 3-j symbol. The relative intensities of the line splittings for the 1/2 to 1/2 transitions and the 1/2 to 3/2 transitions are below, following the same structure as in equations 4.9 and 4.10.

$$I_{S_{1/2}-P_{1/2}} \propto [1/3,\ 1/6] \quad \text{with } [\pi, \sigma] \text{ polarization} \tag{4.12}$$

$$I_{S_{1/2}-P_{3/2}} \propto [1/6,\ 1/4,\ 1/12] \quad \text{with } [\pi, \sigma, \sigma] \text{ polarization} \tag{4.13}$$

For the π polarization, which corresponds to the first entry in the brackets for both the relative intensities (4.12 & 4.13) and the changes in energies (4.9 & 4.10), the 1/2 to 1/2 transition has a larger splitting of $\pm 2/3\mu_B B$, compared to the 1/2 to 3/2 transition that has a splitting of $\pm 1/3\mu_B B$. Therefore the 1/2 to 1/2 transition will have a larger FWHM when there is a magnetic field together with other broadening mechanisms

For the σ polarization this is also the case, but it is not as obvious due to the extra 1/2 to 3/2 splitting. The 1/2 to 3/2 has two σ entries in the brackets (which corresponds to four lines), with splittings of $\pm 1\mu_B B$ and $\pm 5/3\mu_B B$. The 1/2 to 1/2 transition has two σ lines with a splitting of $\pm 4/3\mu_B B$, which is less than the largest 1/2 to 3/2 splitting. The 1/2 to 1/2 transition still has a larger FWHM due to magnetic field because of the relative intensities of the 1/2 to 3/2 σ lines. The $\pm 5/3\mu_B B$ has an intensity $\propto 1/12$, while the $\pm 1\mu_B B$ has an intensity $\propto 1/4$. When broadened by other mechanisms to the point where the splittings are unresoveable, the σ polarization of the 1/2 to 3/2 line will be dominated by the higher intensity splitting of $\pm 1\mu_B B$. This is similar to having one splitting at $\pm 7/6\mu_B B$, which is less than the 1/2 to 1/2 transition splitting at $\pm 4/3\mu_B B$.

Therefore for both polarizations, and any combination of the polarizations, the 1/2 to 1/2 transition will always have a wider FWHM than the 1/2 to 3/2 transition when there is a magnetic field. If there is no magnetic field, then there will be no splittings and the two line transitions will have the same FWHM, again without opacity effects.

Application of the Technique in Experiments

To apply the Zeeman Broadening technique using the Al III lines in an experiment, there are two conditions that must be satisfied. The first is that the lines must exist and be more intense than the continuum background, which is not trivial in a dense plasma when working with lines in the optical regime. The second is that the magnetic-field-induced line difference between the two lines must be clearly detectable. For a particular value of magnetic field, these constraints put limitations on the spectral resolution and the maximum electron

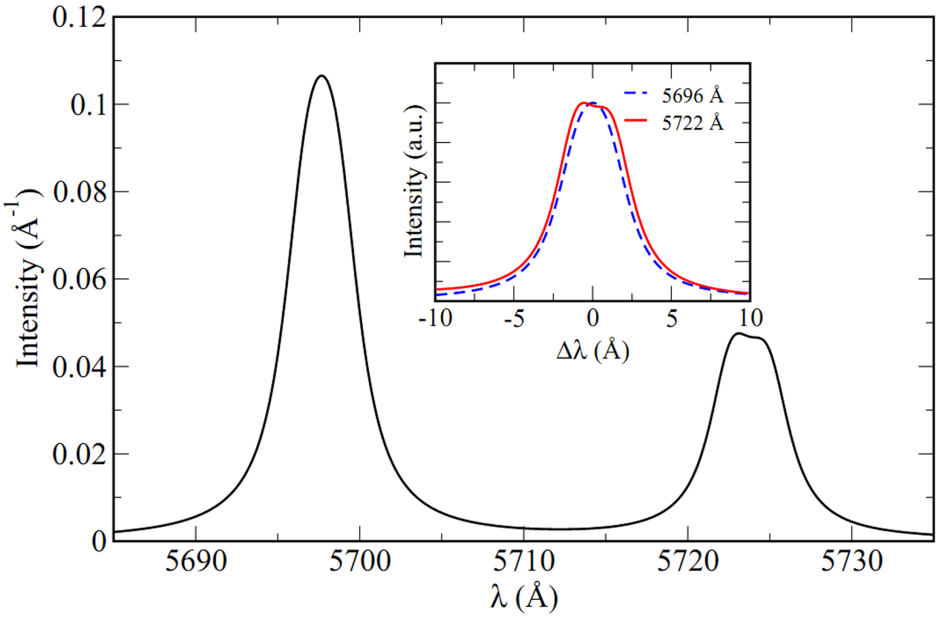

Figure 4.1: Simulated spectrum of the Al III doublet with $n_e = 5\times10^{17}cm^{-3}$, $T_e = 3eV$, $B = 6.5T$ ($r = 300\mu m$ and $I = 10kA$), and $\Delta\lambda_{instr.} = 0.5\mathring{A}$

density of the plasma. It is also important to note that the values of these constraints are a function of the strength of the magnetic field.

The necessary resolution is determined by considering the contribution of the broadening due to the Stark effect compared to the difference in the broadening due to the Zeeman effect. To do this, it is necessary to calculate the Al III line pair under conditions relevant to the plasma under study in the experiment. As a first approach, the WIS performed these calculations assuming an electron density of $5\times10^{17}cm^{-3}$, electron temperature of $3eV$, and a magnetic field of $6.5T$. The value of $6.5T$ was reached assuming that the observation was $300\mu m$ away from the wire and that $10kA$ of current was flowing at the center of the wire. The simulated spectrum is shown in Fig. 4.1, assuming an instrumental resolution of $0.5\mathring{A}$ and that the plasma consists of only one B and one n_e.

Under these conditions, the broadening contribution due to Stark is $\approx 3.5\mathring{A}$

while the Zeeman width contribution is $\approx 3.0\mathring{A}$, and the FWHM difference between the two lines with both effects is about 10%. The necessary instrumental width, or resolution, is dependent on both the width difference and the width contribution from the Stark effect. The contribution of the instrumental width should be of the order of the width difference due to the magnetic field, and the effects of instrumental width should not change the line width ratio by more than 10%. When the Stark contribution is large, such as the case in the simulated spectra shown in Fig. 4.1, an instrumental width that is $\sim 15\%$ the Stark width should not degrade the relative width difference [15]. Therefore to see the width difference, a spectral resolution of $0.5\mathring{A} \approx 0.15 * 3.5$ is needed. (These guidelines were revised and restricted during the progression of the experiments. At the beginning of the project it was believe that a $1.0\mathring{A}$ instrumental resolution would be sufficient for the plasma conditions stated above.) For a given electron density, as the Zeeman contribution decreases so does the FWHM difference and a better spectral resolution is needed.

There is a point at which the Zeeman contribution to the FWHM is so small compared to the Stark or other contributions that even with an excellent resolution one would not be able to detect the difference in the FWHM. This means that there is an effective threshold for the magnetic field measurement determined mostly by the percent difference in the FWHM with some dependance on the system resolution and the signal to noise ratio, but this percent difference is dependent on the relative Stark and Zeeman broadening contributions. Figure 4.2 shows a map of the usable parameter space in gray with a red boundary line calculated for a 8% difference in the FWHM of the Al III doublet lines. This graph was calculated at the WIS for this work. The star on the graph represents the conditions of the simulated spectrum in Fig. 4.1. It is possible to extend the

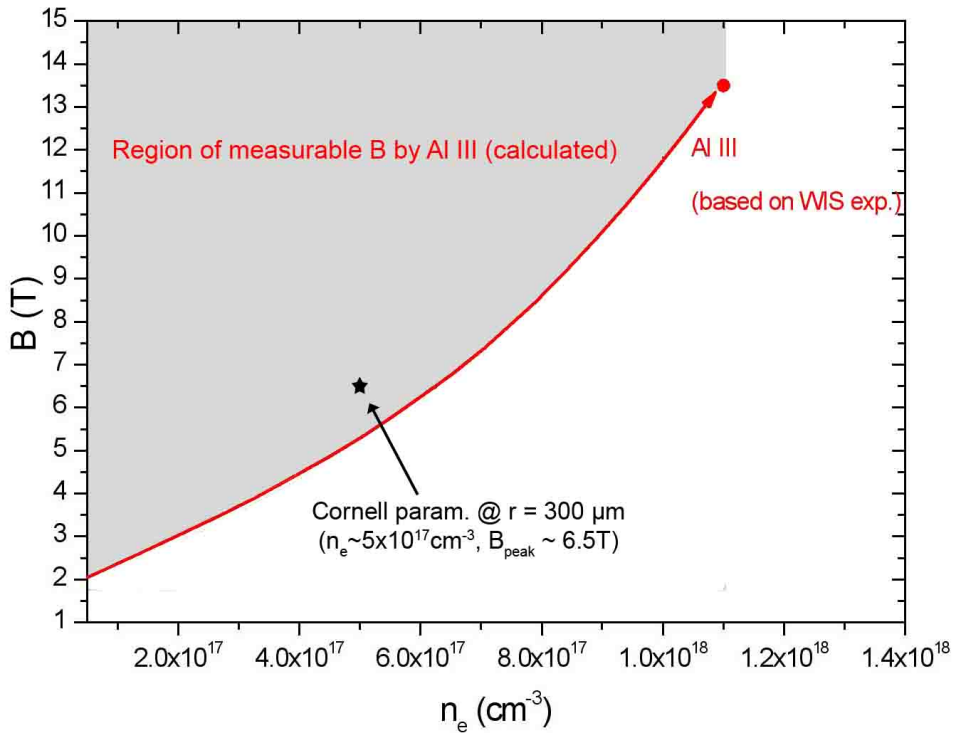

Figure 4.2: Parameter space of measurable magnetic field using the Al III doublet, with a threshold corresponding to a 8% difference in the FWHM.

measurement below the boundary line in Fig. 4.2. To do this it is necessary to have excellent spectral resolution and a high signal-to-noise ratio.

With regards to the application of this technique, it is a robust measurement in that all other influencing factors in the spectra tend to diminish the magnetic field induced difference in the FWHM of the 1/2 to 1/2 transition compared to the 1/2 to 3/2 transition. Said in another way, the magnetic field is the only influence that will cause the 1/2 to 1/2 line to have a larger FWHM. Everything else will make a difference harder to detect or actually widen the FWHM of 1/2 to 3/2 line (e.g. opacity effects) so that the difference is reduced or eliminated.

Poor spectral resolution or a low signal-to-noise ratio can make a small FWHM difference appear to be no difference, meaning that a small magnetic

field will be interpreted as no magnetic field. There is no way to correct for these effects other than to know the threshold for measurable magnetic field for a given resolution. Under these conditions if no FWHM difference is measured, then there is no field or it is below the threshold for measurement.

Opacity effects will broaden the 1/2 to 3/2 line more than the 1/2 to 1/2 line because the 1/2 to 3/2 line is more intense. Therefore the FWHM difference will be reduced and the measured magnetic field would be less than the actual magnetic field if no adjustments were made. Thankfully, the opacity doesn't just affect the FWHM and can be accounted for and factored into the magnetic field measurement. Because opacity has a larger effect on the more intense line (the 1/2 to 3/2 line), more of that line will be self-absorbed compared to the less intense line. Therefore the intensity ratio of the two lines will be affected by decreasing. Without opacity effects the intensity ratio of the 1/2 to 3/2 line to the 1/2 to 1/2 line is 2; with opacity effects the line intensity ratio will be less than 2. The measured difference in the line intensity ratio can then be used as part of the fitting of the line pair to account for opacity effects. This will determine a more accurate magnetic field that will be larger than what would be obtained from the measured FHWM assuming no opacity.

The Al III doublet for the Zeeman Broadening measurement has the extra complication that it is vulnerable to a common impurity line. There is a doubly ionized carbon (C III) line at 5695.92$\mathring{A}$ that almost exactly overlays the Al III line at 5696.60$\mathring{A}$. Carbon is a common impurity found in wire array based plasmas because the vacuum systems are not very clean and hydrocarbons are used in the manufacturing of the fine wires. If that C III line is present in a spectrum, it will increase the FWHM and the intensity of the 1/2 to 3/2 Al III line. This

means that any difference in the FWHM of the two Al III lines will be reduced, possibly to the point where the two lines have equal widths or the 1/2 to 3/2 line is wider. However, with an increased intensity of the 1/2 to 3/2 line due to the C III line, the line intensity ratio of the two Al III lines will be above the norm of 2.

An increase in the line intensity ratio above 2 could be evidence of carbon impurities in the plasma. Unfortunately, it is difficult to account for the effects of the carbon impurity when fitting a magnetic field to the line. If not accounted for, the fitted magnetic field will be less than the actual value (due to the decreased difference in the FWHM). To account for the impurity, other measurements of the carbon distribution within the plasma must be made. The best way to do this is to measure other C III lines at different wavelengths, ideally ones that share an electron configuration with the line of interest. The "impurity" line has an electron configuration change from $1s^2 2s 3d$ to $1s^2 2s 3p$. Therefore the doubly ionized carbon triplet between the electron configurations $1s^2 2s 3p$ to $1s^2 2s 3s$, are the best lines to use when evaluating the overlapping C III impurity line. They occur at 4647.42$\mathring{A}$, 4650.25$\mathring{A}$, and 4651.47$\mathring{A}$.

It is also important to consider the difference in the original Zeeman Broadening benchmarking experiments at the WIS compared to the application in the experiments presented in this thesis. In the WIS experiments, the B-field did not vary along the line of sight and its generation was decoupled from the plasma generation [47, 48]. Figure 4.3 is a drawing of the experimental setup. The plasma was ablated by a laser from an Al target on a rod, creating a plume of plasma. The B-field was generated by a current applied to the rod creating a cylindrically symmetric magnetic field profile that was only dependent on the

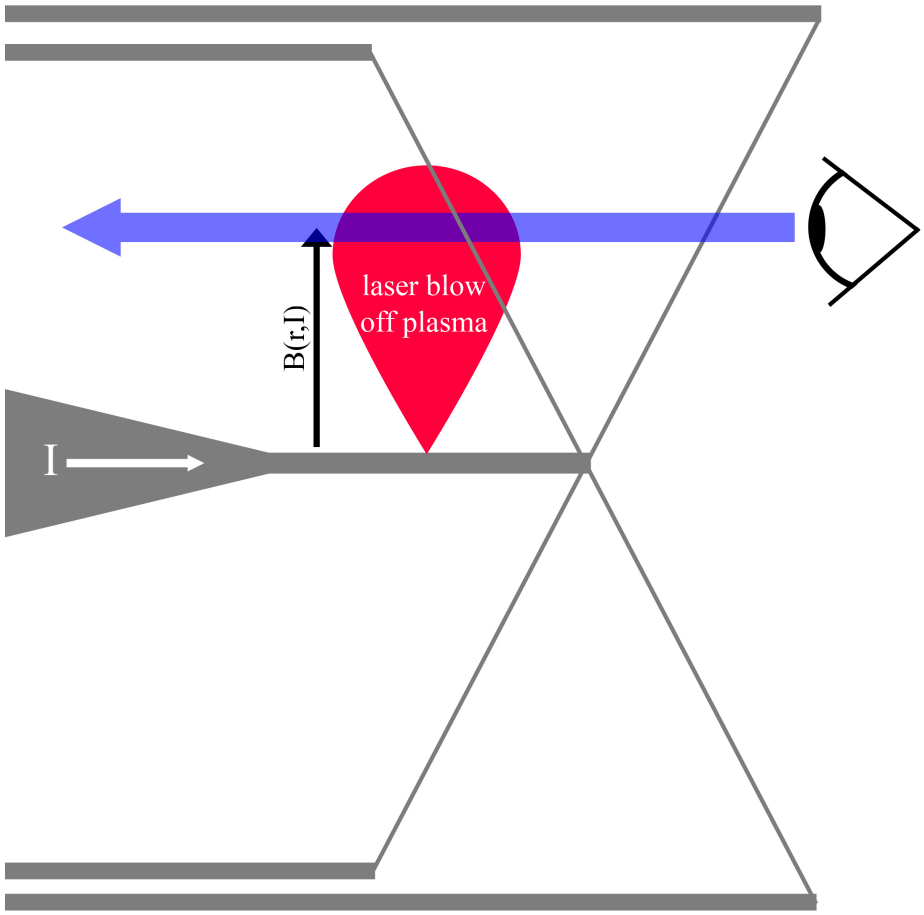

Figure 4.3: Drawing of the WIS experimental setup. The B-field did not vary along the line of sight and it was decoupled from the Al laser blowoff plasma.

radius and the applied current. The plasma was viewed along a line of sight parallel to the rod such that the magnetic field did not vary over the line-of-sight. This simple experimental setup was ideal for measuring the magnetic field. In the experiments presented in this thesis, the magnetic field was not decoupled from the plasma and the magnetic field did vary over the line-of- sight. This difference makes inferring the magnetic field using this technique more complicated in the experiments presented in the thesis than the benchmarking experiments at the WIS.

The modeling that is used to generate the line profiles used for determining the magnetic field was developed at the WIS and used by Professor Maron and his team to analyze the spectra in this thesis. The line shape calculations begin with ab initio calculations of Zeeman splitting, Stark broadening, and Stark shifting of the line. Any Doppler or instrumental effects are convolved into the line profile afterwards. The specifics of the modeling are beyond the scope of this thesis, but can be found in works published by the WIS [46, 47].

4.2 Electron Density

Electron density results have been determined largely by one of two ways in the analysis of the data presented in this thesis. The first was by a Baranger based calculation performed at the WIS that was used as a first approximation in the analysis of the high resolution spectra of the Al III doublet. This was a first approximation because it assumed a single density fit with no magnetic field. The more comprehensive code described in Sec. 4.1.2 was used only for simultaneous determinations of magnetic field and electron density.

The Baranger method is a semi-classical approximation of impact theory of the Stark effect that is appropriate for isolated lines [1]. A line is isolated when the broadening of its originating energy level is less than the difference between adjacent energy levels. In most cases, line profiles due to Stark broadening are very complicated and without an analytic form, the exception being isolated lines in the impact approximation. These lines have a Lorenztian distribution

$$\mathcal{L}(\omega; T, n_e) = \frac{1}{\pi} \frac{\Delta\lambda(T, n_e)}{\Delta\lambda^2(T, n_e) + (\omega - \omega_0 - d(T, n_e))^2} \tag{4.14}$$

with the original line position ω_0, a line shift d, and a half width at half max

(HWHM) $\Delta\lambda$ [21, 48]. For the plasma conditions in this thesis, the Al III doublet lines are isolated and the Stark effect is linear because the main contribution to the Stark broadening is the electron impacts that result in a finite life-time of energy levels. Specifically, the life time of the energy levels τ is roughly

$$\tau \sim \frac{1}{n_e\, Q}, \tag{4.15}$$

where n_e is the electron density and Q is the electron-impact collision-rate coefficient [15, 20].

A semi-empirical approximation for the Stark shift d is

$$d \approx 0.5\ \Delta\lambda \times \frac{d_o}{w}, \tag{4.16}$$

where $\Delta\lambda$ is the Stark HWHM (which is linear with n_e), d_o is the Stark shift with an electron density of $n_e = 10^{16} cm^{-3}$, and w is the Stark width parameter [12, 21]. The quantities d_o and w need to be calculated or measured for each transition. In general one can say that the shift is proportional to the width, with the leading coefficient $\ll 1$ being a weak function of the temperature [15].

The Baranger treatment incorporates the effect of inelastic collisions and the change in electric field due to stationary electrons and ions. Professor Maron concludes that for a single electron density, their Baranger based calculations are accurate within 20%, and differ from their more sophisticated codes that include elastic processes by only 10% [33].

The second method is based on line profiles generated by PrismSPECT®, which are then fitted to the lower resolution data to simultaneously determine the electron density and electron temperature. PrismSPECT® is a collisional-radiative modeling code that generates spectra for LTE or non-LTE plasmas [27].

4.3 Electron Temperature

There are many ways to determine the electron temperature. Given in Eqn. 4.18 and 4.19, below, are two ways to determine electron temperature analytically that are valid within limiting conditions. It is more often the case that these conditions are not meet and a detailed collisional-radiative code is needed to calculate synthetic spectra which are then compared to the data. The electron temperature determinations of the data presented in Sec. 5.2 were performed by fitting PrismSPECT® spectra to the data.

The most common way to extract information about electron temperature is to compare the intensities of several lines that are highly depended on temperature. To do this, one begins with Eqn. 3.18 and substitutes the appropriate population density function and partition function $Z(T)$. (In previous sections, Z was ionization. Here, written as $Z(T)$, it is the partition function.) The population density N_k of the level k, assuming Maxwell-Boltzmann distribution, follows, where N is the total population density, g_k is the statistical weight of the level, $Z(T_e)$ is the partition function dependent on temperature T_e, and lastly E_K is the energy of the level [22]. It is important to remember that when using a Maxwell-Botlzmann distribution, LTE must be assumed.

$$\frac{N_k}{N} = \frac{g_k}{Z(T)} \exp\left(\frac{-E_k}{kT}\right) \tag{4.17}$$

The intensities, with Eqn. 4.17 substituted in for N_k, are then divided to give a ratio. When comparing two lines from the same ionization state using the above population density, the partition functions and total density are eliminated from the intensity ratio [22].

$$\frac{I_{ki}}{I_{nm}} = \frac{g_k A_{ki} \lambda_{nm}}{g_n A_{nm} \lambda_{ki}} \exp\left(\frac{E_n - E_k}{kT_e}\right) \tag{4.18}$$

Thankfully the values of the constants g, A, λ, and E can be found in the NIST Atomic Spectra Database [38], and one need only measure the intensities experimentally to determine the temperature. The limitation to using lines from the same ionization state is that the levels must be separated by $> 0.5eV$. It can be difficult to satisfy this condition.

As levels of subsequent ionizations are compared for dense LTE plasmas, the Saha Equation must be incorporated to derive the correct intensity levels [22].

$$\frac{I_{ki}}{I_{nm}} = \frac{g_k A_{ki} \lambda_{nm}}{g_n A_{nm} \lambda_{ki}} \frac{1}{4\pi a_0^3 N_e} \left(\frac{kT}{E_H}\right)^{3/2} \exp\left(\frac{E_n + \Delta E_\infty - E_k - E_\infty}{kT_e}\right) \tag{4.19}$$

The intensity ratio is determined by atomic constants and temperature as before, but now it is also determined by the electron density of the plasma N_e. The new atomic constants are the ionization energy of hydrogen E_H, the Bohr radius a_0, the ionization energy E_∞ of the z ion, the reduced ionization energy from the z to $z+1$ ion is $\Delta E_\infty = 2zE_H a_0/\rho_D$, and the Debye radius ρ_D.

If the electron density is known, then it is simple to determine the electron temperature from the measured intensities. However if the density is not known, the determination quickly becomes more complicated as another line is usually required to match the number of variables.

For the data in this thesis, the electron temperature and density were determined by fitting PrismSPECT® spectra to the data. The chosen lines included the two Al III lines used for the magnetic field measurement, whose line intensity ratio has no temperature dependence, making them excellent for determining the electron density. Then, to determine the temperature, a set of six additional lines of a lower ionization state within the field of view that were recorded simultaneously were used. Due to the resolution, the closely spaced six Al II $3s4p - 3s4d$ lines between $6226\mathring{A} \sim 6243\mathring{A}$ appear as one broad line.

Therefore the Al III lines were used to constrained the density while the Al II and Al III line ratio determined the temperature.

CHAPTER 5

ELECTRON TEMPERATURE AND ELECTRON DENSITY RESULTS

This chapter presents two sets of experiments with their electron temperature and electron density results. In the first set of experiments, initial information was collected about the plasma properties in a single wire explosion driven by a $\sim 10kA$, $500ns$ rise time current pulse. These experiments were important for determining the feasibility of a Zeeman Broadening magnetic field measurement. The data and results from these experiments are described in Sec. 5.1.

The second set of experiments developed a detailed accounting of the plasma and its properties at many times during the single wire explosion. This data set was designed to have a large bandwidth to measure the electron temperature profile, which required a spectral resolution insufficient for a Zeeman Broadening measurement. The results from this data set are presented in Sec. 5.2.

5.1 Results of Exploratory Experiments

Shown in Fig. 5.1 are spectra collected from two experiments, each exploding a $15\mu m$ Al wire, collecting light at a distance of $300\mu m$ away from the wire, and integrating for $12ns$. These were taken on the preliminary experimental setup that used the Kentech Gated Optical Imager (GOI) and a one meter spectrometer described in Sec. 2.3. LCP shot 1143, shown in dashed blue in Fig. 5.1, was taken at $458ns$ into the pulse with a machine current of $9.2kA$. LCP shot 1144, shown in solid green Fig. 5.1, was taken at an earlier time, $371ns$, with a machine current

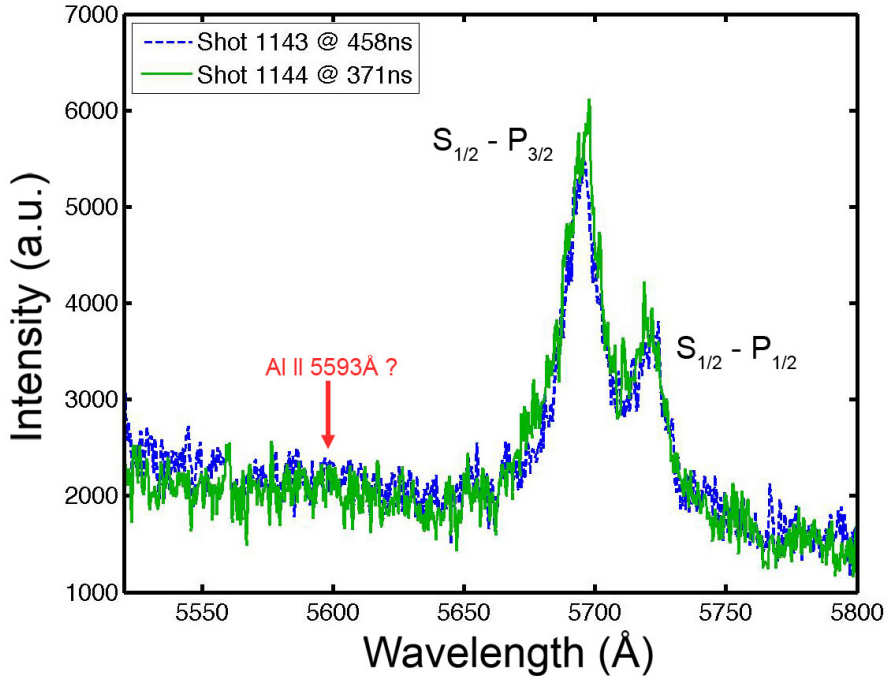

Figure 5.1: Spectra from LCP3 shots 1143 (dashed blue) and 1144 (solid green). The Al III doublet lines can be seen at 5696$\mathring{A}$ and 5722$\mathring{A}$, while the Al II line at 5593$\mathring{A}$ is near or below the continuum level.

of 8.9kA. The intensities and features of the two shots were very similar and are shown together, unnormalized, in Fig. 5.1.

While data taken with 3.2$\mathring{A}$ resolution does not enable measurement of the magnetic field, we can determine the electron density and a lower limit to the electron temperature. With temperatures in the 2 – 5eV range, Doppler broadening does not significantly contribute to the widths of the lines. Non-thermal Doppler broadening also has a negligible impact due to the slow expansion of the plasma, determined in subsequent experiments discussed in Sec. 6.2 to be $\sim$ 3km/s. Therefore, the line widths are due only to instrumental broadening and Stark broadening. We then deconvolved the measured Voigt FWHM and the Gaussian instrumental resolution of 3.2$\mathring{A}$ to determine the Lorenzian width

of the Stark contribution [51]. Shot 1143, at $458ns$ into the pulse, had a measured FWHM of $16.3\mathring{A}$ for both lines. This deconvolved to a Stark width of $15.6\mathring{A}$. Shot 1144 had a measured FWHM of $16.3\mathring{A}$ for the $5722\mathring{A}$ line, and $15.8\mathring{A}$ for the $5696\mathring{A}$ line. This equated to a Stark widths of $15.6\mathring{A}$ and $15.2\mathring{A}$, respectively.

Calculations based on the Baranger treatment in a linear Stark effect regime [46] for the doublet Al III line at $5722\mathring{A}$ give a FWHM of $5.4\mathring{A}$ for $n_e = 1 \times 10^{18} \pm 2 \times 10^{17} cm^{-3}$ and $T_e = 4eV$. Therefore, with a Stark width of $15.6\mathring{A}$, we concluded that late in time at $300 \pm 100\mu m$ away from the original wire position, the plasmas electron density is $2.9 \times 10^{18} \pm 6 \times 10^{17} cm^{-3}$ for the two spectra shown in Fig. 5.1, since the Stark widths of the two $5722\mathring{A}$ lines were $15.6\mathring{A}$.

To determine a lower limit for the electron temperature, we considered the line ratio between the Al II line at $5593\mathring{A}$ and the Al III doublet component at $5722\mathring{A}$. Due to the noise levels of the original data, it is unclear whether or not the Al II line is present in either shot. Remarkably, shots 1143 and 1144 had very similar current levels, timing, density, and line profile. In order to extract possible information from the spectra, we assumed reproducibility between the shots within detectable limits imposed by the $3.2\mathring{A}$ resolution, and processed the spectra together. We fitted and subtracted the continuum, applied a linear Gaussian $3.0\mathring{A}$ high frequency filter, took the geometric average of the two shots, and rejected random scatter points below 3σ. In the resulting combined spectrum shown in Fig. 5.2, the Al II line at $5593\mathring{A}$ is present, although very dim.

To determine the intensity ratio, the lines were fitted by a Lorentizan. The resulting intensity ratio of the Al II line to the Al III line at $5722\mathring{A}$ was 1.0×10^{-2} Collisional radiative (C-R) [46] modeling done at the WIS calculated an electron

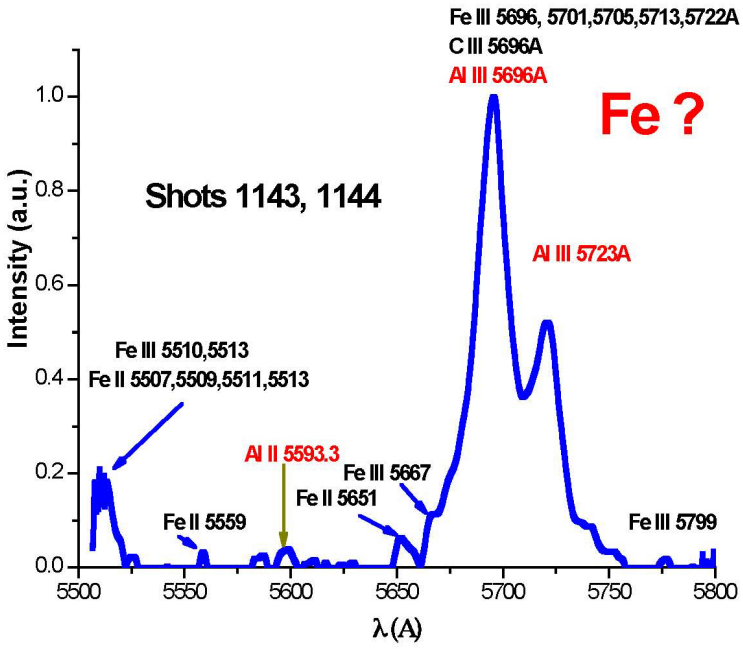

Figure 5.2: Resulting spectrum from processing that combined spectra at $r = 300\mu m$ from shot 1143 and 1144, taken at $458ns$ and $371ns$, respectively, after the start of current.

temperature of $4eV$ for this line ratio. Therefore assuming plasma consisted of a single region with one n_e and one T_e, we concluded that the plasmas electron temperature was $4eV$ or greater for these two spectra with an electron density of $3 \times 10^{18} cm^{-3}$ at $300\mu m$ away from the original wire position.

From the measured electron density of $3 \times 10^{18} cm^{-3}$ and a temperature limit of $4eV$ at a radius $300\mu m$, the Spitzer resistivity is determined to be $1.6 \times 10^{-4} \Omega m$. This was calculated using Eqn. 5.1 for plasma resistivity perpendicular to **B** with Z being the effective Z of the plasma ions [10].

$$\eta_\perp = 2.0\,\eta_\parallel = 2\left(5.2 \times 10^{-5} \frac{Z \ln \Lambda}{T^{3/2}(\mathrm{eV})}\right)\Omega\mathrm{m} \tag{5.1}$$

This leads to a magnetic diffusion timescale of $1.0ns$, or said another way, a skin depth of $8mm$ for the plasma conditions at a radius of $300\mu m$. This diffusion timescale is very small compared to the current rise time of $500ns$ and the skin

depth is much larger than the $4mm$ diameter of the detectable plasma. The skin depth is calculated using Eqn. 5.2 where ω is the frequency of the current driver and μ is the magnetic permeability [28].

$$\delta = \sqrt{\frac{2\eta_{\perp}}{\omega\mu}} \tag{5.2}$$

Therefore, one might expect that the current would flow uniformly throughout the plasma in spite of being driven to larger radii by inductive effects during the current rise. However, no information on the magnetic field could possibly be gathered due to insufficient spectral resolution, and so no experimental conclusions can be drawn about the current flow profile.

With an electron density of $3 \times 10^{18} cm^{-3}$, a magnetic field greater than $15T$ would be needed to measure the magnetic field. Magnetic fields of that magnitude would require the $10kA$ peak current in these experiments to be carried entirely within $r \simeq 130\mu m$. In order to measure the magnetic field in our system, the Stark line broadening contribution needed to be reduced relative to the Zeeman broadening while greatly improving the resolution.

In order to accomplish this, several possibilities were considered, including increasing the current to increase the magnetic field, changing the wire diameter to lower the electron density, and collecting data from plasma farther away from the wire at a much lower density. As spectra are collected at larger radii the density was expected to decrease as r^{-2}, while the magnetic field decreases as r^{-1}.

5.2 Evolution of Single Wire Explosion Plasma Properties

Another series of experiments was performed to obtain plasma density and temperature versus time in single wire explosions using the improved Andor experimental setup. In order to collect spectra with a larger bandwidth that included lines useful for electron temperature determinations, a $300 grooves/mm$ grating was used to collect spectra with $7\mathring{A}$ resolution. A total of 11 shots were taken integrating for $50ns$, each with up to 17 spectra that varied with radial position (see Fig. 2.9).

Shown in Fig. 5.3 is a typical current trace for this set of experiments, with a peak current around $11kA$ occurring $430ns$ into the pulse. Overlaid on the current trace are four bars which correspond to the timings of the four sets of spectra shown in Fig 5.4 that were obtained from the fiber bundle. The width of the color bars correspond to the temporal integration of $50ns$ for each shot. Shot 1576, the gray bar, corresponds to the set of "Early Time" spectra in Fig 5.4. Shot 1571, the green bar, shows the timing of the "Mid Time" spectra. Shot 1574, the blue bar, represents the spectra seen at a time approaching peak current, labeled "Peak Time" in Fig 5.4. Finally shot 1577, the pink bar, is the timing of the representative of the spectra seen soon after peak current, i.e. "Late Time", shown in Fig 5.4.

The "Early Time" spectra were integrated for $50ns$ over wire break down beginning at $12ns$ into the pulse. The original wire position is at $r = 0\mu m$, which is near the center of the image. During that time lines from both Al III and Al II were identified. Those were doubly ionized Al III at $5696.6\mathring{A}$ and $5722.7\mathring{A}$, and the six singly ionized Al II $3s4p - 3s4d$ lines between $6226\mathring{A} \sim 6243\mathring{A}$ (which

were unresolveable). The diameter of the Al lines in the plasma was $0.5mm$. Surprisingly there was also a carbon line present. It was a C IV line that expanded radially outward beyond the Al lines. In the spectra the most intense lines and continuum occur at the original wire position.

The "Mid Time" spectra gate pulse began $200ns$ into the pulse and the integration lasted for $50ns$; the spectra are obtained during the middle of the current rise, see Fig. 5.3. The original wire position at $r = 0\mu m$ is located at the center of the image. At this time only the doubly ionized Al III lines can be identified leading to the conclusion that the plasma has heated to the point in the field of view that the aluminum was mostly ionized beyond the singly ionized (Al II) state based on the lack of emitted Al II lines. The continuum levels are also the brightest during this times, and is more sensitive to density compared to temperature. The plasma has now expanded to a diameter of $1.1mm$ based on the width of continuum and line intensity.

The "Peak Time" spectra gate pulse began $300ns$ into the current pulse and lasted for $50ns$. While this is not exactly at the peak of the current rise this spectrum was chosen because it does show a shift in the characteristics of the plasma that is commonly seen around peak current. Additionally, this data set was chosen to exemplify "Peak Time" spectra (over a shot that was obtained closer to peak current) because it has a shifted field of view of the optical fibers that included the edge of the plasma. At peak time the plasma continues to expand and the singly ionized Al II species reappears. At "Peak Time", the singly ionized Al II lines are most intense at $r = 850\mu m$ and dimly present within that radius. This may indicate that the plasma is cooling as it is expanding. The diameter of the plasma is now about $2.2mm$.

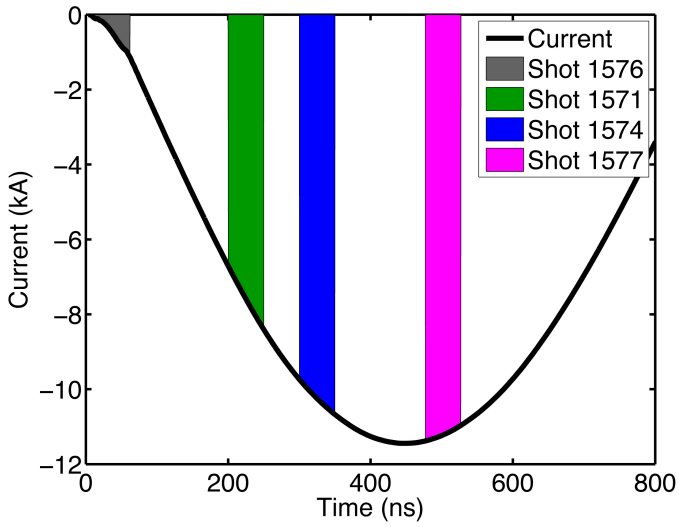

Figure 5.3: Typical LCP3 current in black with four shot timings overlaid corresponding to the spectra in Fig. 5.4. The width of the color bars corresponds to the time integration.

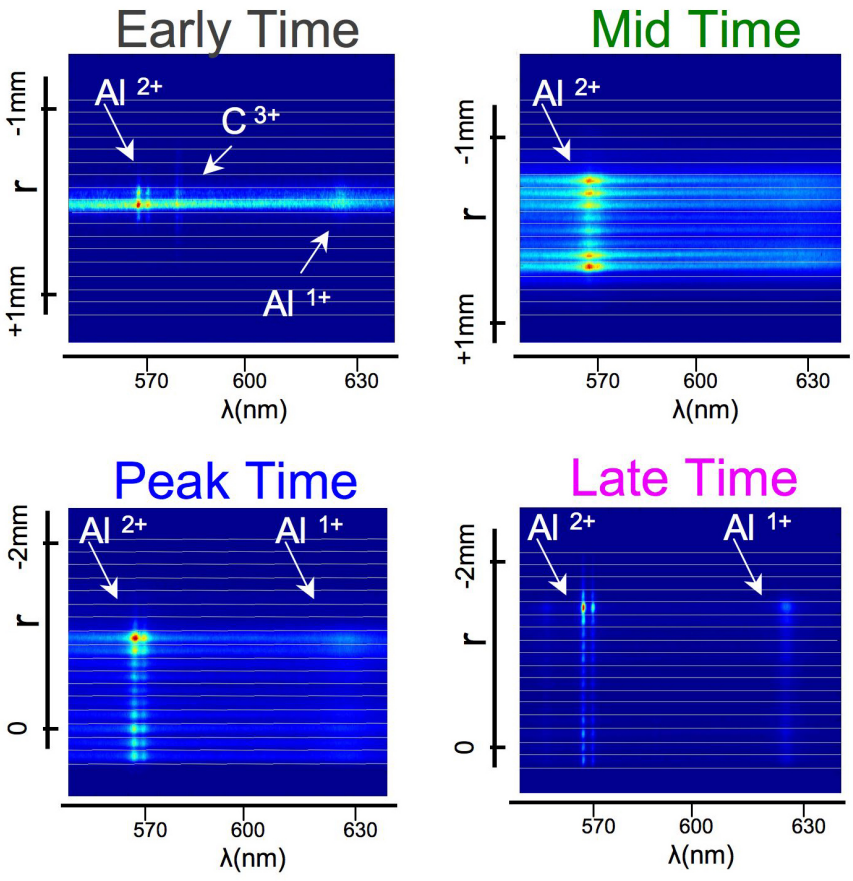

Figure 5.4: Representative spectra of the wire explosion evolution. The timing of these correspond to the color bars plotted in Fig. 5.3. The white horizontal lines delimit the spectra from adjacent fibers.

The "Late Time" spectra gate pulse began at $477ns$ into the pulse and lasted for $50ns$. This was about $45ns$ after peak, and the original wire position was located at the bottom of the image so that the field of view included one edge of the plasma as it expanded radially. Late in time both the singly and doubly ionized Al II and Al III lines are still detectable everywhere while appearing narrower, which is an indication that the plasma is less dense than at peak current. At this time the plasma has expanded to a diameter of about $4mm$.

The spectra shown in Fig. 5.4 were evaluated with PrismSPECT® [27] to determine the electron density and electron temperature. To do this the raw images were taken in ascii form and the flat field calibration was applied to the data. Then each spectrum from the images was summed vertically over the rows of pixels corresponding to a fiber. Occasionally the image was rotated sightly because the ICCD camera had twisted on its mounting. To account for this, the MATLAB function "improfile" was used to interpolate the correct horizontal pixel rows for summation.

Once an individual spectrum was extracted from the raw data file, it was compared with spectra calculated with PrismSPECT®. The assumptions used in PrismSPECT® calculations were that the plasma was optically thin ("zero width" in PrismSPECT®) and in local thermodynamic equilibrium (LTE). For LTE to be valid, the electrons must have a Maxwellian distribution and the Saha equation must apply. To obtain these conditions, the collision rate of the plasma must be significantly greater than the radiation rates [20]. The collision rate increases with density, which is why even radiation-dominated plasmas with high density can be in LTE.

For conditions relevant to wire explosion plasmas, e.g. $T_e = 2eV$ and

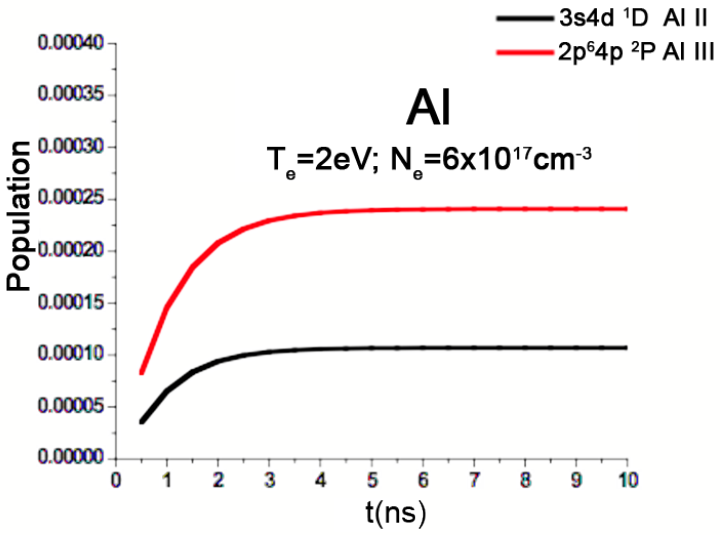

Figure 5.5: Results of a collitional-radiative calculation showing the plasma reaches a steady state in $3ns$.

$n_e = 6 \times 10^{17} cm^{-3}$, a collisional radiative calculation without an LTE assumption was performed by Professor Maron. Shown in Fig. 5.5, it found that with those parameters a steady state would be reached within $3ns$, which is short compared to the radiation rates and the time scale for the plasma to change. As the density increases, the time to reach steady state decreases. Therefore the assumption that the plasma is in LTE is valid.

The amount of opacity within the plasma can be determined from the Al III doublet at 5696.6$\AA$ and 5722.7$\AA$ as discussed in Sec. 4.1.2. However, within the 7$\AA$ resolution, it is very difficult to detect a difference from 2 in the line intensity ratio of the Al III doublet. Therefore, the assumption of optically thin is adequate.

The Al III doublet at 5696.6$\AA$ and 5722.7$\AA$ was used to fit the electron density since these lines have a negligible temperature dependence, as shown in

Sec. 4.1.2. Then intensities of the Al III and Al II line groupings were used to determine the electron temperature. The resulting electron temperature and densities are graphed in Fig. 5.6 and Fig. 5.7 respectively.

Early in time the plasma is between $2 - 2.5eV$ and $1.6 - 2.1 \times 10^{17}cm^{-3}$, with the peak temperature and density occurring at the wire. As current drives the wire explosion, the plasma was heated and became denser as it expanded. At "Mid Time", during the peak of dI/dt, the plasma was at its densest. Also at "Mid Time", structure appeared in the electron density and temperature. Even though a single parameter electron temperature and density were used in fitting the spectra, the data shows a hotter less dense plasma shell surrounding a colder denser region surrounding the initial wire position. The "colder, denser" inner region had an electron temperature of $2.75eV$ and an electron density of $1.5 \times 10^{18}cm^{-3}$. The surrounding region had an electron temperature of $3.0eV$ and an electron density of $1.2 \times 10^{18}cm^{-3}$.

As the current reached its peak, the plasma has expanded radially and decreased in density overall. The structure evident in the "Mid Time" remained, but with a comparatively colder central region and a hotter shell at the edge of the plasma. There was plasma beyond $r = 1100\mu m$; however, data was not included for those locations because the Al II lines were no longer detectable and a temperature cannot be determined. The entire plasma was expanding because the magnetic pressure was not enough to balance the thermal pressure, and the plasma decreased in density as it expanded. Therefore, peak densities were not at peak current. The central region had an electron temperature of $2.6eV$ and an electron density of $6.6 \times 10^{17}cm^{-3}$. At the edge of the ability to measure temperature, the hotter less dense surrounding shell had an electron temperature of

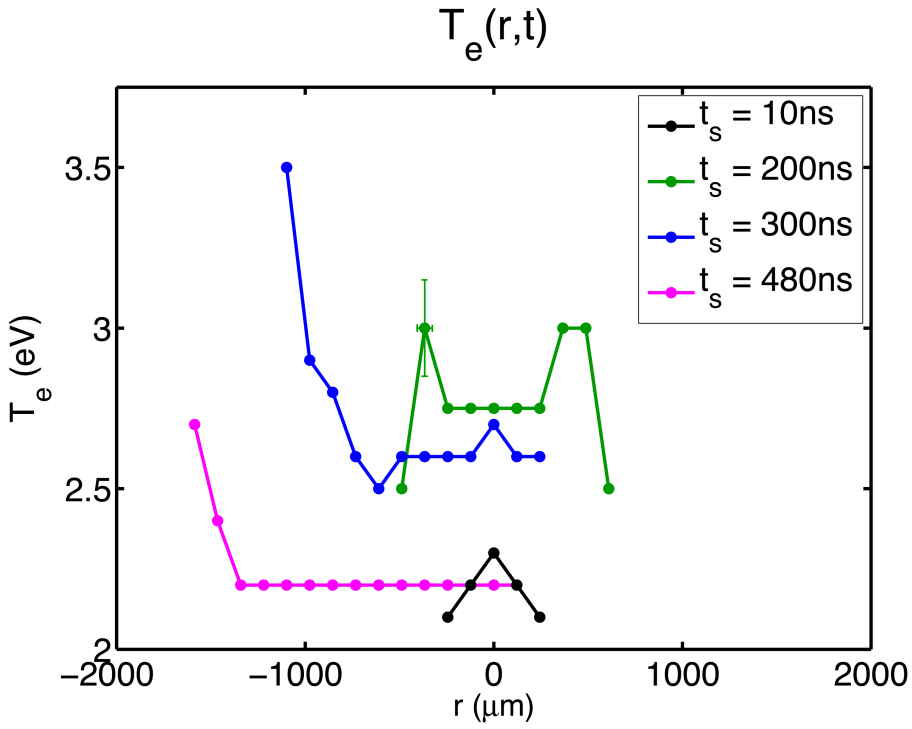

Figure 5.6: Electron temperatures for the spectra in Fig 5.4 determined using PrismSPECT®.

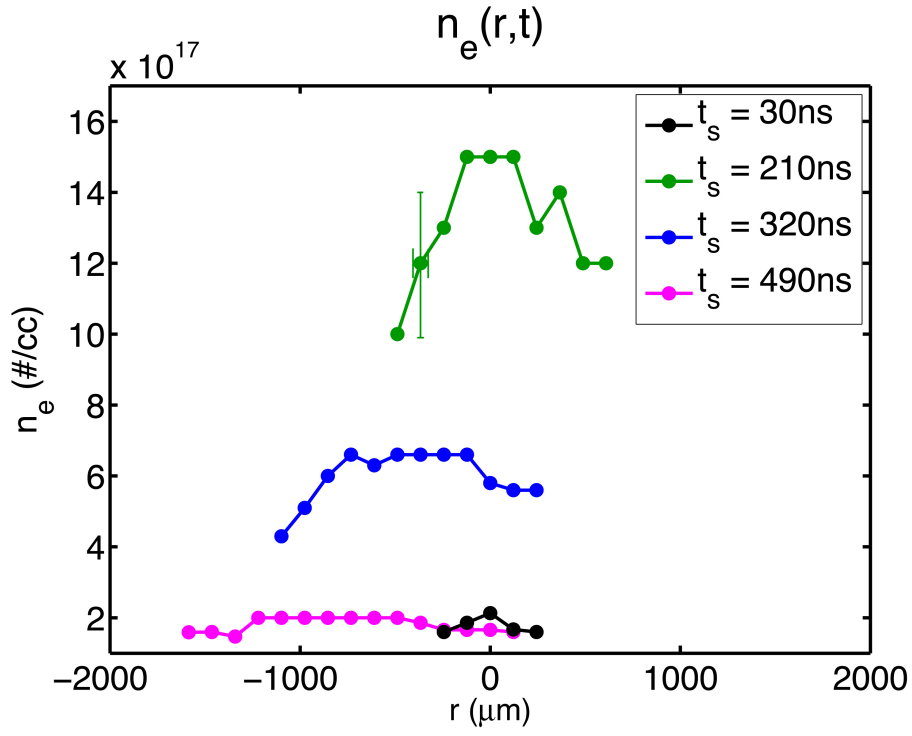

Figure 5.7: Electron densities for the spectra in Fig 5.4 determined using PrismSPECT®.

$3.5eV$ and an electron density of $4.3 \times 10^{17} cm^{-3}$.

At "Late Time" the plasma continued to expand while the current decreased while maintaining the same structure as earlier. The expansion continued the cooling and decrease in density of the central plasma. The colder denser central region had an electron temperature of $2.2eV$ and an electron density of $1.6 - 2 \times 10^{17} cm^{-3}$. As with "Peak Time", the plasma expanded beyond the points listed on the plot in Fig. 5.6 and Fig. 5.7, but those data points were not included because the Al II lines were no longer present and an electron temperature could not be determined. As far out as measurements can be made, the hotter less dense shell had a peak electron temperature of $2.7eV$ and a density of $1.6 \times 10^{17} cm^{-3}$.

Looking closer at the central dense region, it would have been helpful to have laser shadowgraphy images. It was not possible to collect that type of data during the experiments because a laser was not available. However, similar experiments were performed at the P. N. Lebedev Physical Institute of Russian Academy of Sciences in Moscow, Russia. These experiments did not have any spectral diagnostics, but did collect shadowgraphy images using a $532nm$ laser. The experiments were performed by exploding $25\mu m$ Al wires with a $10kA$ current pulse that had a rise time of $400ns$. Information about the experimental setup and pulser can be found in S. I. Tkachenko's paper [49].

From these experiments at the Lebedev Institute, Dr. Shelkovenko provided unpublished laser shadowgraphy images of the exploding wire at various times during the experiment. Shown in Fig. 5.8 are four shadowgraphy images that were taken at a time within the integration window of the corresponding LCP3 spectra. To the right of Fig. 5.8 are the entire shadowgraphy images of the ex-

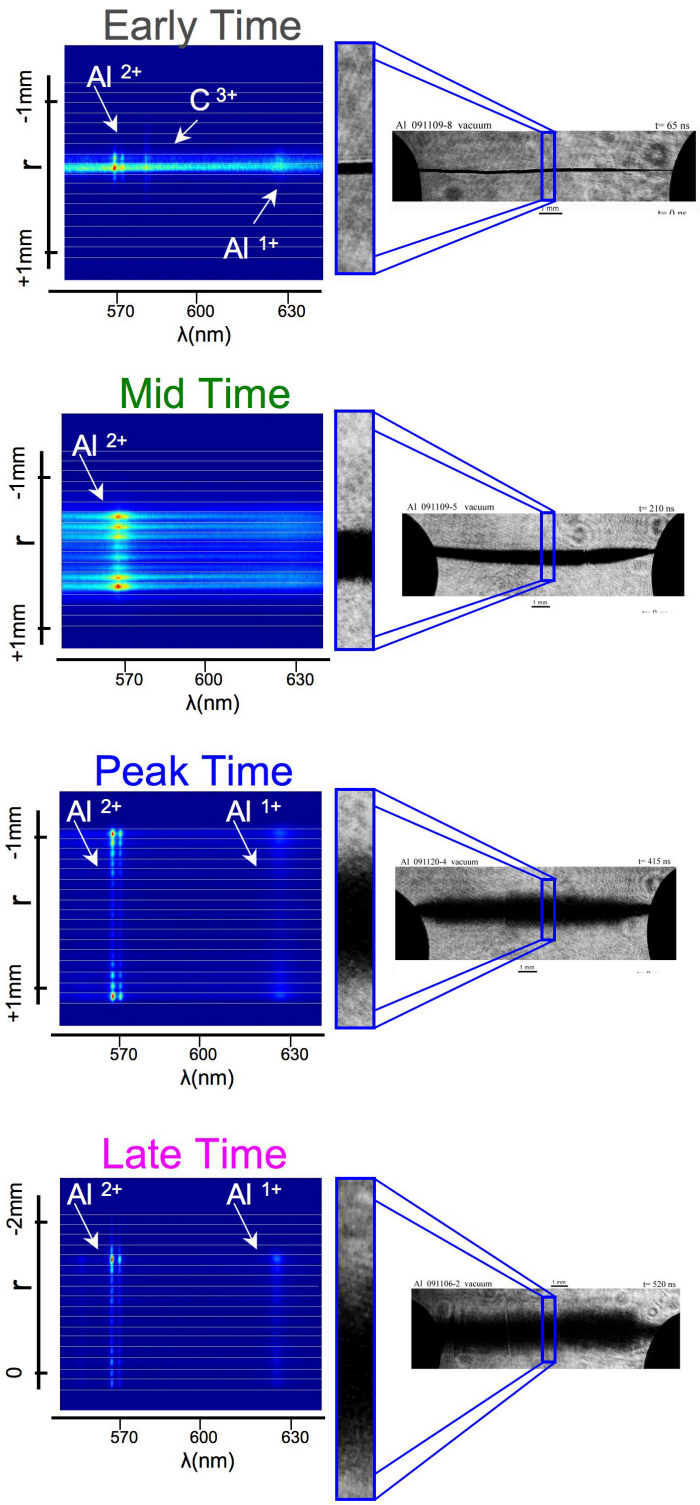

Figure 5.8: Laser shadowgraphy and spectral images of the evolution of the exploding wire plasma. The zoomed shadowgraphy box is scaled and aligned to the spectra image, with the whole shadowgraphy image of the wire to the right.

ploding wires. The zoomed boxes are selections of the center of the wires that are on the same scale as the spectra and aligned so that the original wire positions are the same in both images. Note that a different shot was selected for "Peak Time". The timing of this image was $20ns$ after the spectra shown in Fig. 5.4. It was chosen because the image was centered around the wire core, which is more useful for comparison to the shadowgraphy image.

At "Early Time", it is seen that the wire has expanded and the most intense portion of the spectra is the same size as the expanded wire core. While the surrounding plasma cannot be seen in the shadowgraphy image, the spectra show the extension of the aluminum plasma beyond the core.

At "Mid Time", "Peak Time", and "Late Time" the intensity profile of the spectra relative to the shadowgraphy wire core has changed from "Early Time". In the later spectra, the wire core is the same size as the dim portion on the spectra, which is also the same size as the colder denser plasma as determined by analyzing the spectra. At all of these times, the most intense lines are located just outside of the expanded dense cores, and those dense cores do not exhibit any continuum in the spectra. This suggests that the highest population of singly and doubly ionized aluminum is outside of the colder and denser expanded core.

Consider again the Spitzer resistivity, now with parameters ranging in electron temperatures from $2eV$ to $3.5eV$, and the electron densities from $1.6 \times 10^{17} cm^{-3}$ to $1.5 \times 10^{18} cm^{-3}$. The only dependence on density occurs in the $\ln \Lambda$ in the ionization level Z in Eqn. 5.1. Using the ionization level calculated with PrismSPECT for the various electron temperatures and densities, it is calculated that the Spitzer resistivity ranges from $1.6 \times 10^{-4} \Omega m$ to $3.2 \times 10^{-4} \Omega m$. The associ-

ated skin depth ranges from $8mm$ to $11mm$ which is always larger than the visible size of the exploded wire plasma. Therefore the conclusion made in Sec. 5.1 that the current ought to flow uniformly remains true unless there is a large radius, lower density plasma that is considerably hotter but not visible in these experiments.

From the T_e and n_e evolution, it is clear that the plasma has a structure of a hotter less dense shell surround a colder denser region. The hotter shell expands radially in time with a velocity of about $3km/s$, while the inner colder denser region cools and decreases in density as it expands after peak dI/dt.

CHAPTER 6

MAGNETIC FIELD AND ELECTRON DENSITY RESULTS

This work was intended to determine the experimental feasibility of using the Zeeman Broadening method to measure the magnetic field profile, and infer from it the current density distribution, in an exploding wire plasma. As determined in Chapter 5, the plasma reaches densities between $10^{17} - 10^{18} cm^{-3}$. Recall that $B \geq 4T$ is needed for measurable B when $n_e \geq 10^{18} cm^{-3}$. Naively, if the plasma carries the current at a radius of $r = 0.5mm$ or less, then it should be possible to measure the magnetic field. If the current flows largely at $r \geq 0.75mm$ in these experiments, then a B measurement is unlikely. This can be seen assuming a simple current distribution and its corresponding magnetic field profile shown in Fig. 6.1.

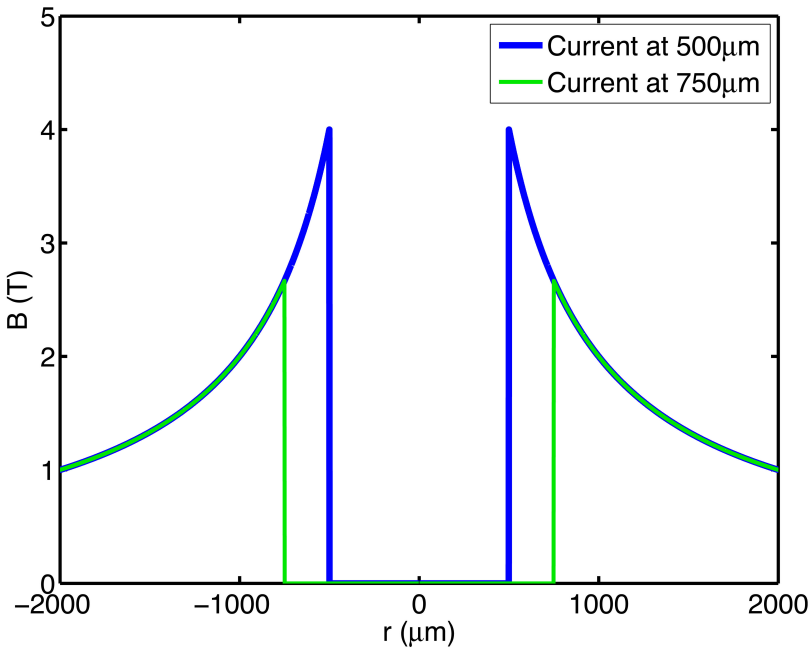

Figure 6.1: Magnetic field distribution from a cylindrically symmetric current profile with 10kA of current at a radius of 500μm in blue, and at a radius of 750μm in green.

6.1 PIMax3 System Results

Of the 64 high resolution spectra sets that were collected with the Princeton Instruments PIMax3 ICCD setup, only one spectrum from one shot was useful to determine the magnetic field. This was because the setup's resolution of $0.75\mathring{A}$ proved to be inadequate, there was no relative or absolute calibration on the setup, the signal-to-noise ratio was too low, and the noise pattern in the data did not follow a Poisson distribution. (All of these inadequacies were addressed when data was taken with the Andor system, the results from which are discussed in Sec. 6.2.) In spite of all of those flaws, important and informative data was obtained with this experimental system concerning making magnetic field measurements in exploding wire Al plasmas, especially in the data referred to below.

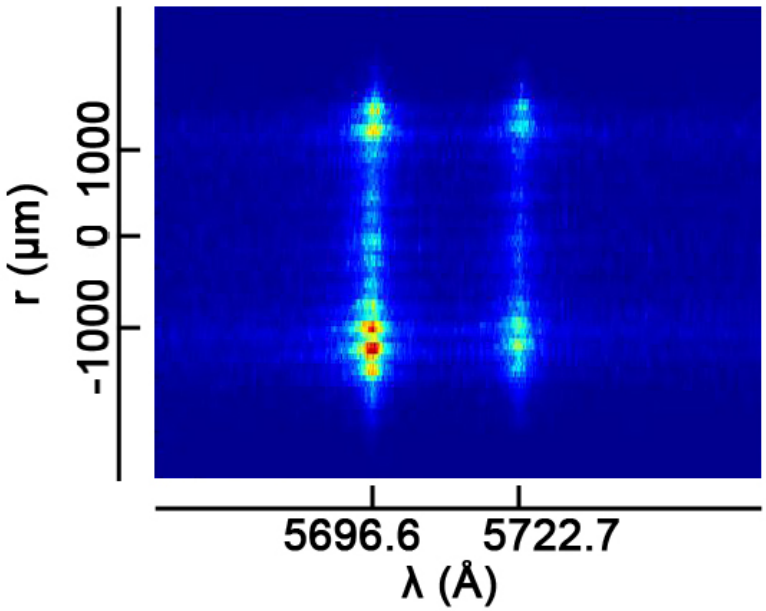

Figure 6.2: Raw spectra from shot 1462.

Shown in Fig. 6.2 is the raw data image from the 17 fibers from shot 1462.

One spectrum from the 17 in this set was used to fit a magnitude to the magnetic field. These data were taken starting at $485ns$ into the current pulse, which is $35ns$ after peak current, and integrating for $100ns$. This current and camera gate timing are depicted in Fig. 6.3. The average current during the snapshot was $10kA$. Each spectrum integrates spatially over $200\mu m$ which is the focal spot size of the fiber, with the original wire position defined as $r = 0\mu m$.

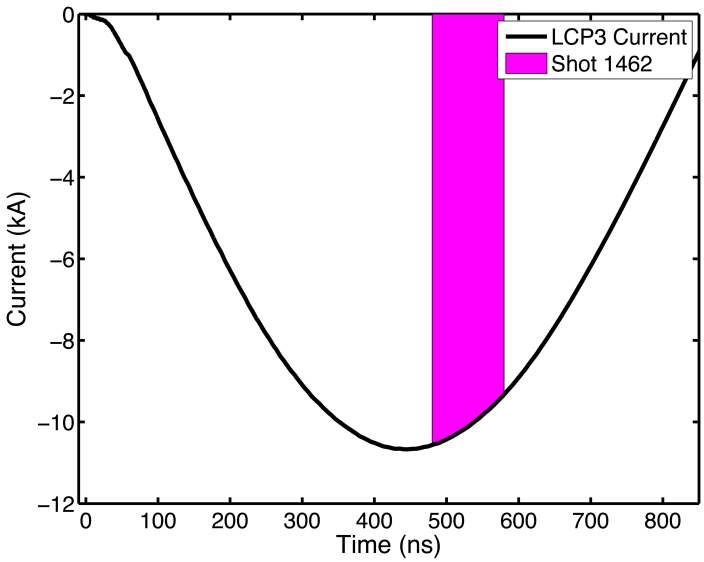

Figure 6.3: Current trace from shot 1462 with the spectral timing and integration window highlighted in pink.

After summing over the vertical pixels for each spectrum in Fig. 6.2, the data was then fitted with two Lorentzians and a flat continuum per the method described in the Zeeman Broadening paper [48]. A Lorentzian line profile is appropriate to use because the Gaussian contribution to the line profile due to the spectrometer is very small. Therefore the true Voigt profile can be approximated as a Lorentzian, which is much easier to use when fitting experimental data.

Difficulties were encountered in fitting the data because of the effect of the high level of the noise, that also didn't follow a standard noise distribution. For

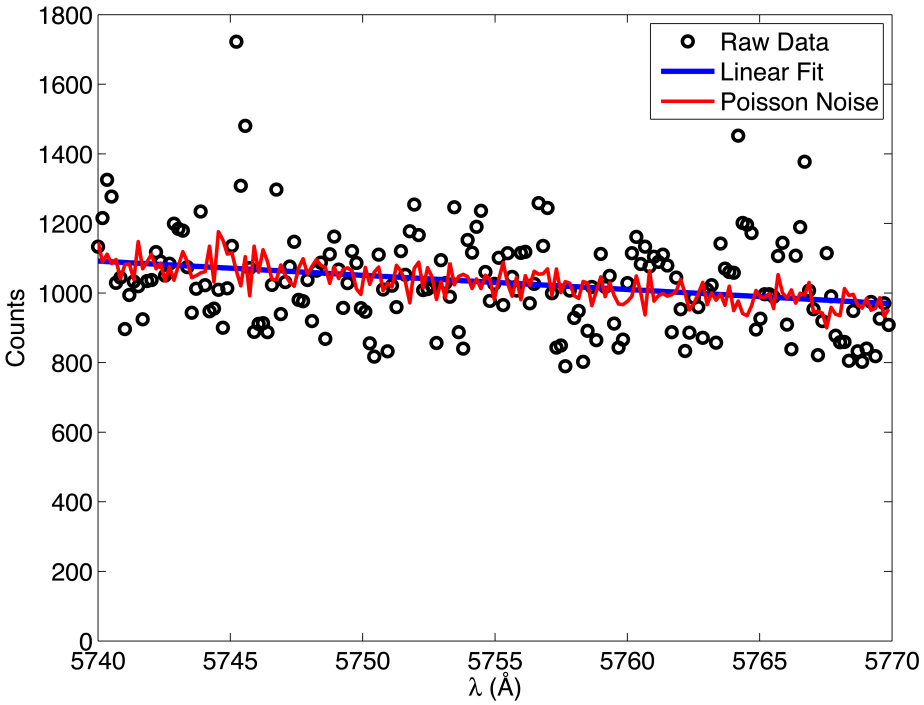

Figure 6.4: The raw counts for the continuum in shot 1462 plotted as circles. The blue line is a linear fit to this section of the data, and overlaid in red is artificial Poisson noise given the mean number of counts of the data. The noise from the camera does not follow a Poisson distribution, and the noise level is $\sim$ 27% of the signal.

ICCDs and other electronic devices, the noise should follow a Poisson distribution [50]. However for this set of spectra, the noise did not follow a Poisson distribution, as seen in Fig. 6.4 for a portion of the spectrum well away from any actual lines. The major obstacle in this noise is it's large variance. In addition, the noise level is a huge $\sim$ 27% of the signal. Therefore to obtain a reasonable fit, the continuum level had to be fixed and then the two Lorentzians were fitted to determine the line location, FWHM, and intensity. This problem resulting from the noise makes error bars on the fits difficult to assign, leading to great difficulty in assigning error bars to the magnetic field that is inferred from this system.

The FWHMs of the two Al III lines are shown in the top plot in Fig. 6.5. The blue line is the FWHM of the more intense 1/2 to 3/2 transition at 5696.6$\mathring{A}$. From here forward, this transition will be identified with a subscript of 3/2 in the plots. The red line is the FWHM of the less intense 1/2 to 1/2 transition at 5722.7$\mathring{A}$, which will be identified with a subscript of 1/2 in the plots. In this set of data, the FWHMs of the two lines range from 2.3$\mathring{A}$ to 6.5$\mathring{A}$.

In Sec. 4.1.2, it was shown that the FWHM of the 1/2 to 1/2 transition can be larger than the FWHM of the 1/2 to 3/2 transition only if there is magnetic field broadening. To enable fitting the magnetic field, it is preferable if the difference in the FWHMs is greater than 10%. To evaluate the difference in the FWHMs, the line width ratio was calculated by dividing the FWHM of the 1/2 to 1/2 line by the FWHM of the 1/2 to 3/2 line. This is plotted as the green line in the middle plot of Fig. 6.5. Whenever the width ratio is greater than 1, there is evidence for magnetic field. When the ratio is near or greater than 1.1, the magnetic field can, in principle, be calculated from analysis of the spectra. This occurs at $r = -976, -732, -488, -244,\ 0,\ 488\ \mu m$.

It is important to not consider the FWHM alone. The line intensity ratio also gives a lot of information about the plasma conditions. In the absence of confounding effects, the intensity of the 1/2 to 3/2 line is twice the intensity of the 1/2 to 1/2 line. Therefore deviations from a ratio of 2.0 are an indication of opacity effects or the carbon impurity line discussed in Sec. 4.1.2. Because there was only wavelength calibration and no intensity calibration on this setup, small deviations in the intensity ratio should be neglected as possibly being due to random or systematic deviations.

For the radial data points with a width ratio near or above 1.1, the intensity

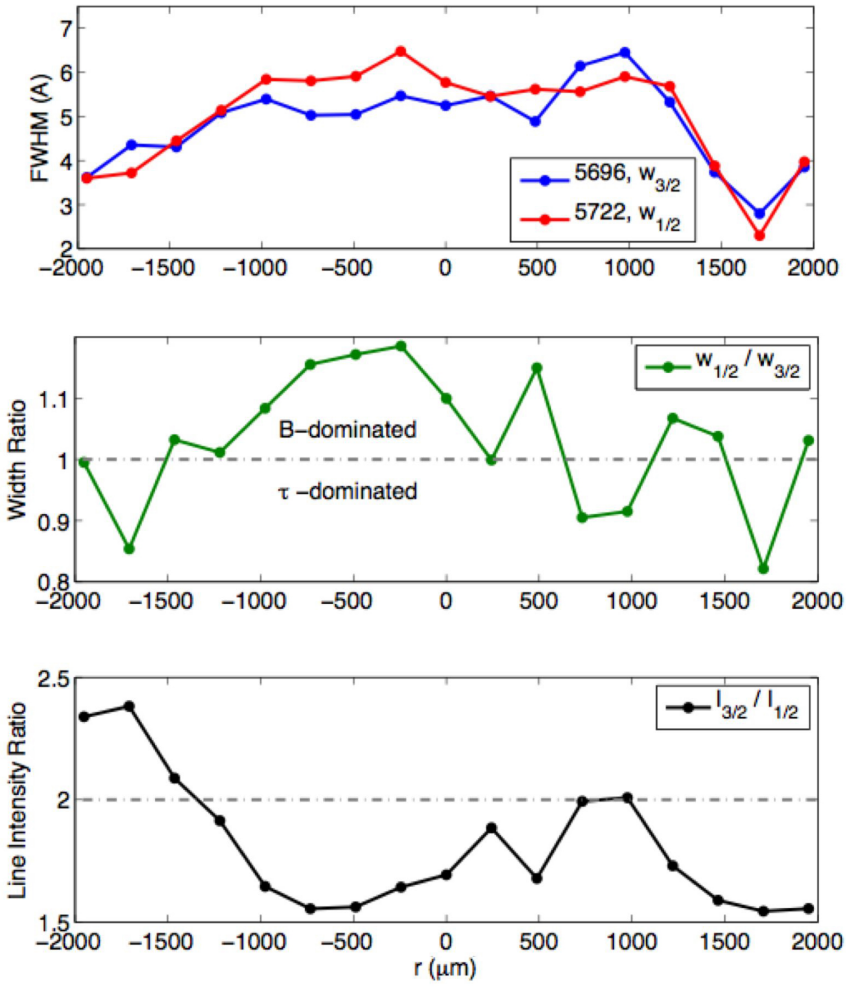

Figure 6.5: Fitted FWHM, line width ratios, and line intensity ratios for the spectra from shot 1462, shown in Fig. 6.2, as a function of radius on the two sides of the original wire position $r = 0\mu m$.

ratio in Fig. 6.5, lower curve, is also less than 2.0 indicating possible opacity effects. This strengthens the argument for the presence of magnetic field between $r = -976\mu m$ and $r = 488\mu m$. There does seem to be a trend of decreasing intensity ratios from one side of the plasma to the other. However given the constraints in the data set arising from the atypical noise and the lack of calibration, it cannot be said with certainty that the trend is real.

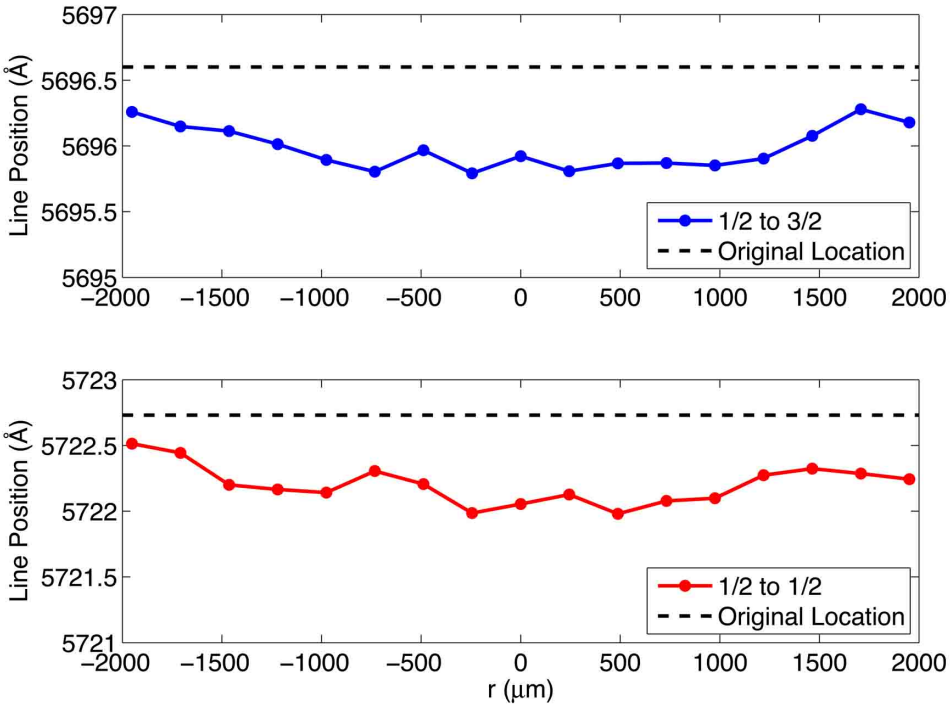

Figure 6.6: Shift of central wavelength for the 1/2 to 3/2 line in blue in the top plot, and the 1/2 to 1/2 line in red in the lower plot.

Consider the outermost four points at $r = \pm 1952$ and $r = \pm 1708$ which have very low line intensity, as seen in the middle plot in Fig. 6.7. With the problematic noise and the line intensity nearing the continuum level, it follows that there would be greater errors in the determination of the intensity ratio at these locations. But because of the problems fitting the data, the errors can only be discussed in general terms. Therefore, without additional information about the experimental setup, including the ICCD camera, it is not possible to say if the decreasing intensity ratio trend is real. Unfortunately the setup was based on a demo ICCD camera and could not be replicated.

To evaluate the electron density of the plasma using Al III lines with potential for large magnetic field broadening, in addition to Stark broadening, study-

ing the shift of the central wavelength of the lines is a great way to confirm that at least some of the line broadening is due to the Stark effect. Shown in Fig. 6.6 is the fitted line locations of the 1/2 to 3/2 Al III line in the top plot, and the 1/2 to 1/2 line in the lower plot. The original and unshifted wavelength is included in each plot in Fig. 6.6 as the dashed horizontal line. The larger shift in the central region is an indication of larger electron densities at those locations. This is confirmed by the fitted first approximation electron densities using the Baranger treatment shown in the top plot of Fig. 6.7.

The density plot at the top of Fig. 6.7 assumes the exploding wire plasma can be characterized by a single electron density along the line of sight, using the first approximation Baranger treatment. In fact the electron density ranges between $3.8 \times 10^{17} cm^{-3}$ and $1.2 \times 10^{18} cm^{-3}$, with the densest plasma seen along lines-of-sight through the center of the plasma around the original wire position. This is consistent with the lower resolution results with slightly higher electron densities for a comparable time frame. It should be noted that the current pulse between these data and the data presented in Sec. 5.2 was different. Therefore a difference in late time density is reasonable.

Examining the entire line intensity distribution as shown in the middle plot of Fig. 6.7, the distribution is consistent with the larger bandwidth data in Sec. 5.2 used to determine the electron temperature and density. When possible it is preferable to use the spectra with the highest line intensities, and therefore best signal-to-noise ratios, when attempting to determine the magnetic field. Unfortunately the spectra with the greatest intensities, located at $r = -976 \mu m$ and $r = \pm 1220 \mu m$, did not have FWHM width ratios large enough to be able to determine a magnetic field. Instead it was necessary to select a less intense

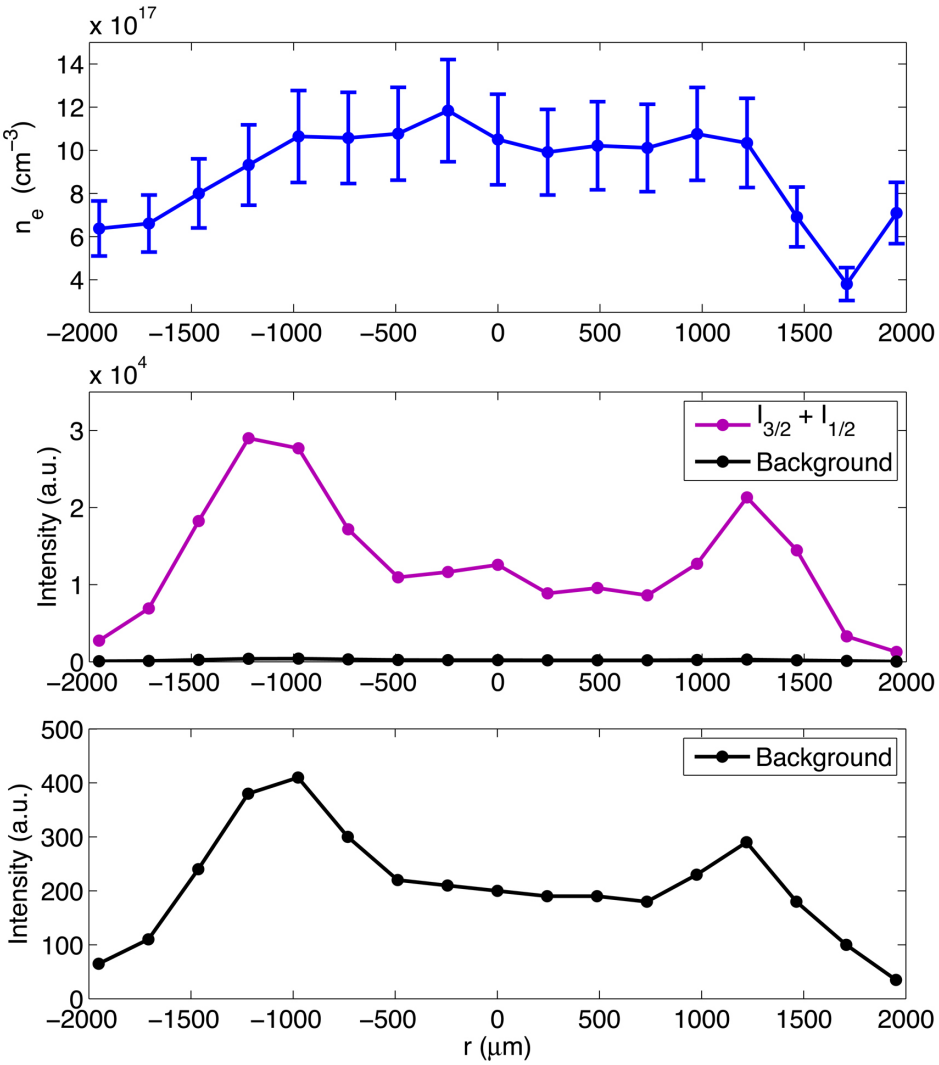

Figure 6.7: First order electron density, total line intensity, and background continuum intensity levels for shot 1462 as a function of radial position.

spectrum that was close to the original wire position that had a larger FWHM ratio.

Professor Maron selected the spectrum at $r = -488\mu m$ for analysis of the magnetic field. This location was preferable because it had slightly narrower lines with nearly the same ratio as the spectrum at $r = -244\mu m$, and the opacity was slightly less while having a slightly larger width difference compared to the

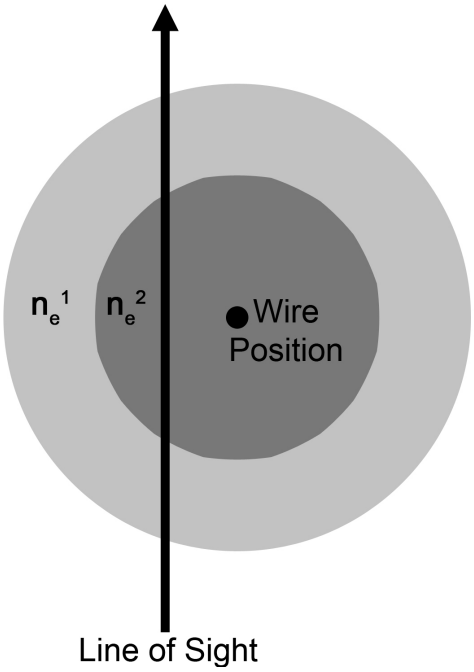

Figure 6.8: Diagram of two region electron density model.

spectrum at $r = -732\mu m$.

In order to achieve a fit to the data that was a good match to the entire line profile, not just the FWHM, it was necessary to assume a two region electron density model. An example of this model is shown in Fig. 6.8. By doing so, the "wing" of the line profile was matched properly. The fitting procedure was to first fit the 1/2 to 1/2 line transition at 5722.7$\AA$ as well as possible. Then the simulated line profile was evaluated for the quality of fit to the 1/2 to 3/2 line transition at 5696.6$\AA$. The χ^2 parameter was used to determine the quality of the fit.

Figure 6.9 shows Professor Maron's best fit to the 5722.7$\AA$ line assuming no opacity and no magnetic field, $B = 0\ T$. The electron density combination that best reproduced the 1/2 to 1/2 line profile was 50% $1.2 \times 10^{18} cm^{-3}$, and 50% $5 \times 10^{17} cm^{-3}$. As a side note, the first approximation electron density shown in

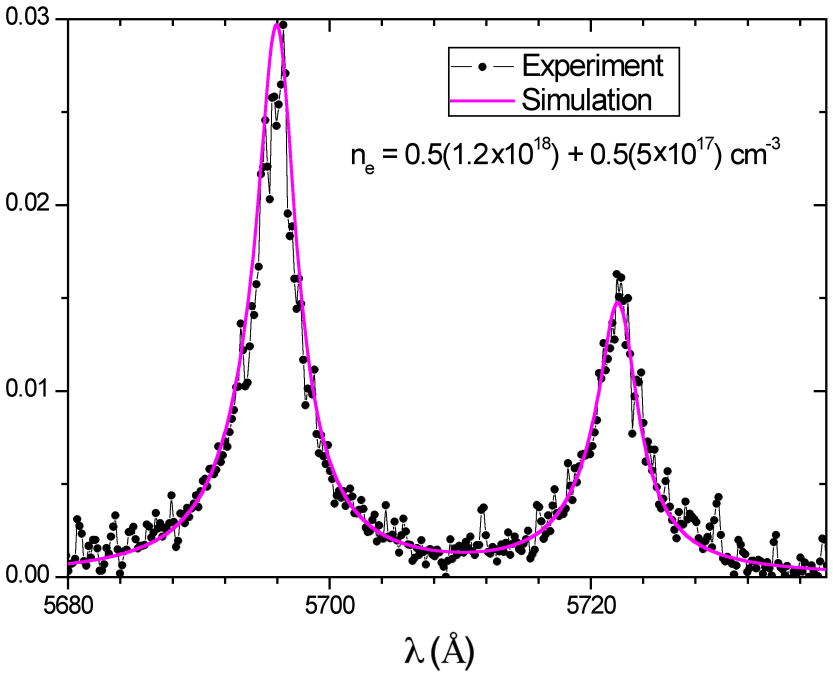

Figure 6.9: Shot 1462 spectrum at $r = -488\mu m$ fitted for two electron densities, no opacity, and no magnetic field.

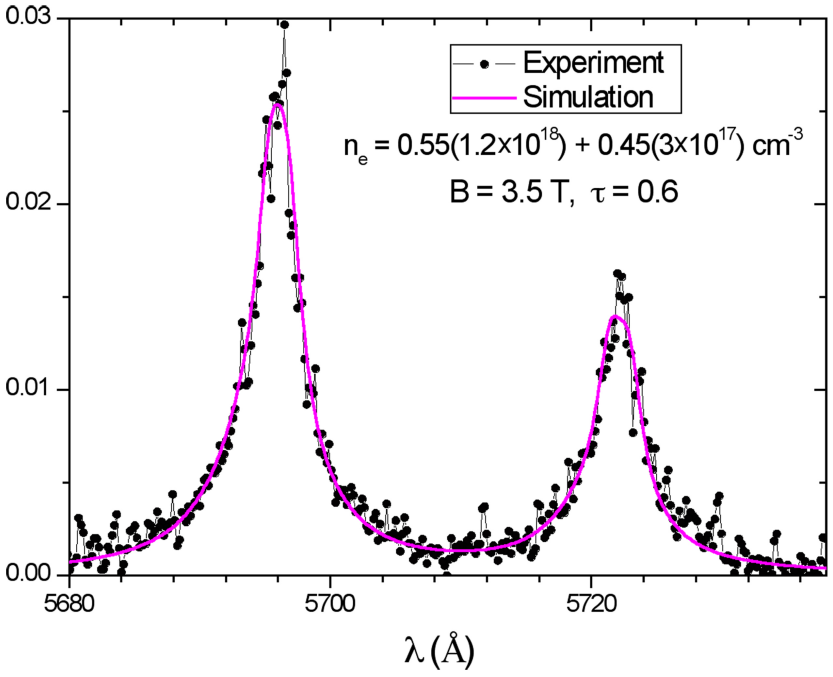

Figure 6.10: Shot 1462 spectrum at $r = -488\mu m$ fitted for two electron densities, opacity of $\tau = 0.6$, and a magnetic field of $B = 3.5T$.

Fig. 6.7 was $1.1 \times 10^{18} cm^{-3}$. It is clear that the simulated line profile overestimates both the FWHM and the intensity of the 5696.6$\AA$ line and is a poor fit.

Figure 6.10 shows Professor Maron's best fit to both the 5722.7$\AA$ line and the 5696.6$\AA$ line assuming opacity effects, magnetic field, and two electron density regions. The electron density combination was 55% $1.2 \times 10^{18} cm^{-3}$, and 45% $3 \times 10^{17} cm^{-3}$, and the optical depth was $\tau = 0.6$ as determined by the intensity ratio. Under these conditions, the best fit to the FWHMs of the two lines occurred with a magnetic field of $B = 3.5\ T$. As compared to Fig. 6.9 without any magnetic field, it is clear that the line profile including magnetic field and opacity effects does a better job of reproducing the FHWM, line intensity, and line profile of the two Al III lines. Therefore it is determined that at a radius of $r = -488 \mu m$, beginning at $485 ns$ into the pulse and integrating for $100 ns$, the average Al III density weighted magnetic field through the line of sight is $B = 3.5\ T$.

Instead of fitting the entire line profile, it is possible to try to infer the magnitude of the magnetic field using the average *full-width-half-area* (FWHA) and the difference in the FWHA between the two Al III doublet lines [48]. Published in the *Beyond Zeeman spectroscopy: Magnetic-field diagnostics with Stark-dominated line shapes* [48] are two figures that plot the average FWHA and difference in FWHA as a function of magnetic field and electron density for observations perpendicular and parallel to the direction of magnetic field. It is important to emphasize that the FWHA is used instead of the more common FWHM. When fitting data with noise that make the determination of the maximum intensity and consequently the FWHM ambiguous, the FWHA has a smaller error [19].

The B's inferred from using only the FWHA and ΔFWHA are plotted in Fig. 6.11 with the corresponding electron densities plotted in Fig. 6.12, as a func-

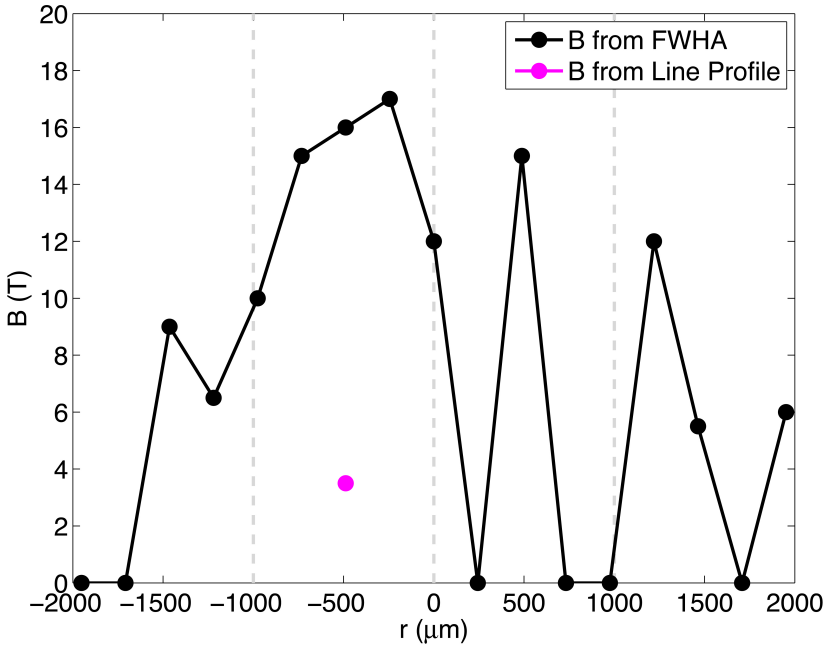

Figure 6.11: B inferred from the Al III doublet lines' average FWHA and ΔFWHA in black, with the B inferred by fitting the line profiles in pink.

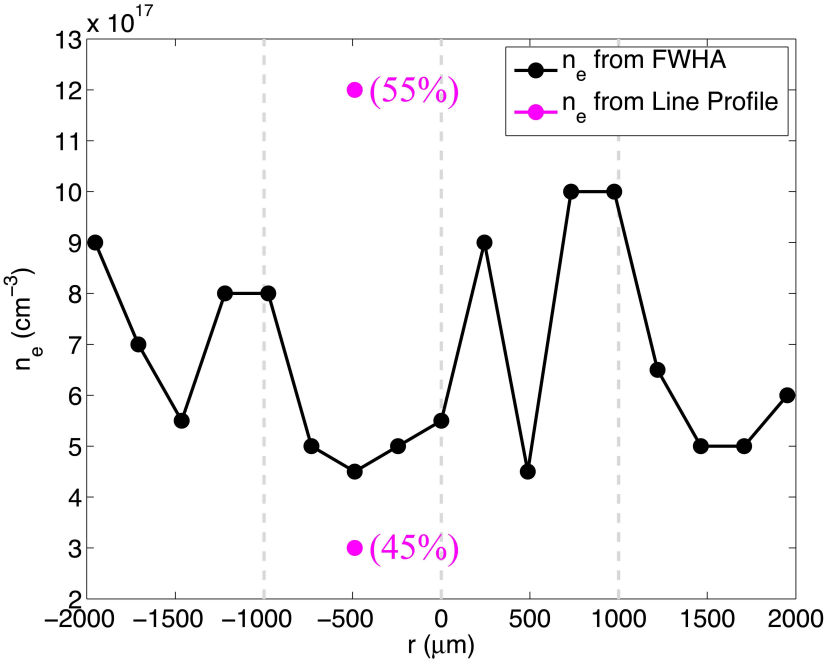

Figure 6.12: The n_e determined from the Al III doublet lines' average FWHA and the ΔFWHA in black, with the two n_e's used to determine B by fitting the entire line profile in pink.

tion of radius. Also included in those figures, in pink, is the $3.5T$ field inferred from fitting the line profile with the two electron densities (resulting from the two region fit). The magnetic field inferred with only the FWHA and ΔFWHA is 4.6 times larger than the line profile magnetic field. This is because the exploding single wire plasma is non-uniform in both B and n_e throughout the line-of-sight. The B's inferred from only the FWHA's are most valid when the magnetic field and electron density have a single value. When they are multivalued, as in the plasmas discussed in this dissertation, a fit to the entire line profile is essential for inferring the magnetic field. While the factor of 4.6 is daunting, this detailed analysis of shot 1462 will be drawn on as much as possible in subsequent analysis.

In a $1D$ problem, a magnetic field of $3.5T$ at $r = 488\mu m$ implies the presence of $8.5kA$ of current within that radius. The average current during the data collection was $10kA$; therefore, if the problem were $1D$ then the conclusion would be that $1.5kA$ was flowing outside $488\mu m$, while $8.5kA$ was inside that radius.

An argument can be made that perhaps more than $8.5kA$ was flowing inside the radius of $488\mu m$ based on the intensity profile of the Al III lines. The magnetic field measurement is an average over the line of sight through the plasma; it is weighted by the intensity of the emitted light at different locations. Examining the intensity profile in the center plot of Fig. 6.7, the profiles look similar to an Abel transform of a cylindrical shell with a peak intensity between $1000\mu m$ and $1250\mu m$. Therefore the light collected through a line of sight at a radius less than $1000\mu m$ would have a non-negligible contribution to integrated intensity from the cross-sections transversed at $r = \pm 1000\mu m$. Examining the width ratios for $r = \pm 1000\mu m$, there is no evidence for magnetic field at those radii.

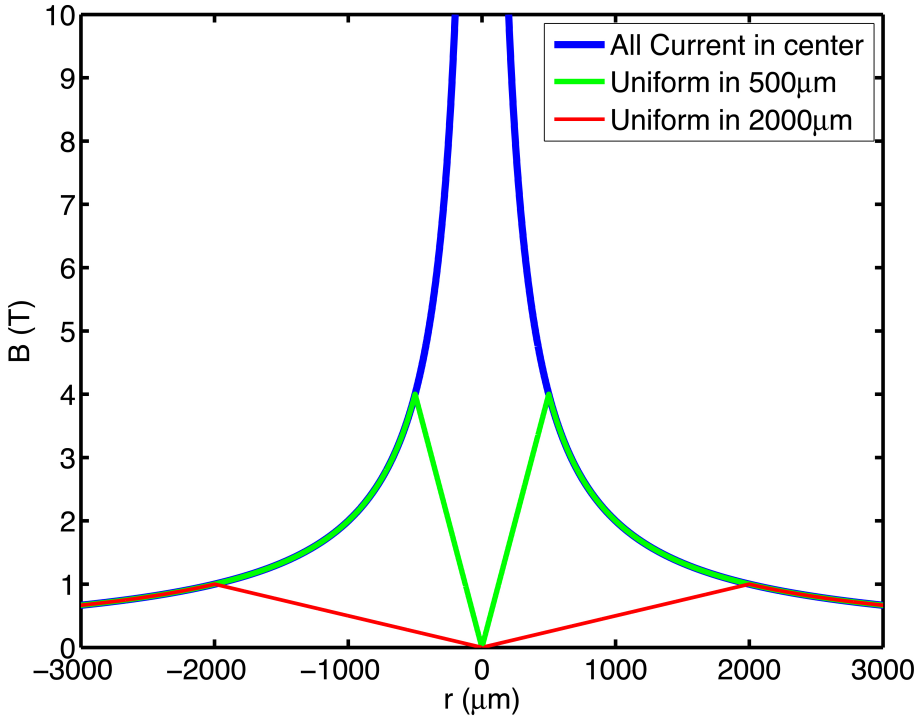

Figure 6.13: Magnetic field profiles from $10kA$ of current where all current flows at the original wire position (blue), with a uniform current density in a radius of $500\mu m$ (green), and with a uniform current density in a radius of $2000\mu m$ (red).

Therefore the contribution from $r = \pm 1000\mu m$ to spectra taken closer to the wire would effectively reduce the average magnetic field. If those exterior contributions could be unfolded from the measured line profile, perhaps a magnetic field larger than $3.5T$ could be measured at $r = -488\mu m$. Unfortunately because of the quality of the data, this hypothesis cannot be tested through further analysis of the data. While this could be done with higher quality data with one view point, a more robust analysis would include two orthogonal views taken simultaneously through the same spectrometer for tomographic analysis.

Three concrete conclusions result from the analysis of shot 1462. It was determined in Sec. 5.2 that the skin depth is larger than the plasma, meaning that

current could flow uniformly through the plasma. If this were the case, then the entire $10kA$ of current would be distributed evenly through the $4mm$ diameter plasma column. The magnetic field topology from this current distribution is shown in red in Fig. 6.13, and the largest value the field reaches is $1T$ at $r = 2000\mu m$. A field of $1T$ is below the threshold for measurement with the PI-Max3 setup and also is inconsistent with the spectra because there is indication for magnetic field with a radius of $1000\mu m$ and an inferred field strength of $3.5T$ at $-488\mu m$. Therefore the first conclusion is that current is not flowing uniformly throughout the plasma column.

Another hypothesis resulting from Sec. 5.2 is that because the current can flow anywhere in the plasma it is possible that inductive effects from the rise in current could push the current out to large radii so that the inductance would be lower. Since the electron density is large enough to support current at the outermost edge of the spectra, it follows under this hypothesis that the current would flow at the largest radii possible, which is $\sim 2000\mu m$, if the plasma were hot enough at large radii. If this were the case, then the magnetic field distribution would be like the red trace in Fig. 6.13 but without any magnetic field within $2000\mu m$. For the same reasons as before, this is inconsistent with the data. Therefore, the second conclusion is that all of the current is not flowing at large radii.

The third conclusion is that all of the current is not flowing at the original wire position. If this were the case, at a radius of $r = \pm 244\mu m$ the magnetic field would be $B = 8.2T$. This is over twice the field that was inferred at $r = -488\mu m$, and since the Zeeman effect is linear for these levels, one would expect to measure at least twice the difference in the FWHMs at $r = -244\mu m$ compared

to $r = -488\mu m$. This was not seen in the data; therefore, all of the current is not flowing at the original wire position.

These conclusions that sum to mean that current is not flowing at the initial wire position, but instead within a smaller region (perhaps $r \lesssim 500\mu m$) near the original wire position. This possibility is consistent with the results from Chap. 5 which find a dense low temperature core plasma. Perhaps the center of the wire core could be mostly neutral which would not carry current well. While a weakly ionized plasma or vapor occurs just outside the center of the core, temperature increased farther from the wire, that could support the current.

6.2 Andor System Results

With the $0.6\mathring{A}$ resolution Andor setup, 24 shots were taken of single exploding wires. In comparison to the PIMax3 data set, the high resolution Andor data set has improved potential for magnetic field measurements because of many system improvements in addition to the higher resolution. While throughly described in Sec. 2.3, the most important improvements were the higher signal-to-noise and the relative calibration that was completed.

In this section, 3 typical shots are presented to show the evolution of the possibility for magnetic field measurements through the single wire explosion. The data were analyzed in a similar method as the data in Sec. 6.1. However, because of the improved noise distribution, now with a noise level $\sim 11\%$ of the signal (27% previously) shown in Fig. 6.14, a continuum background could be fitted in the non-linear least squares regression. Therefore, it was possible to determine confidence intervals for the fitting coefficients which enabled the

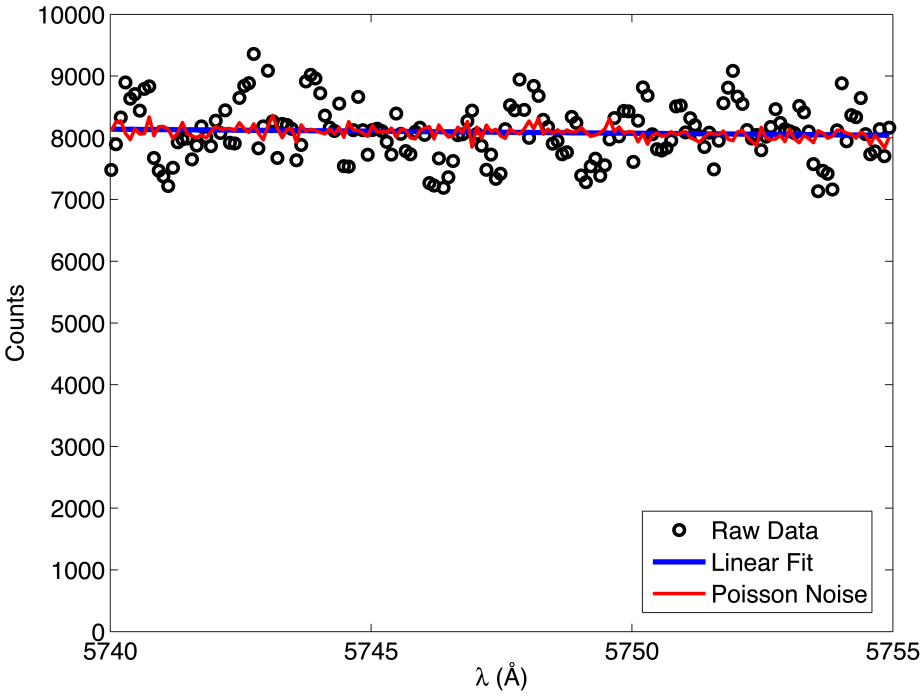

Figure 6.14: The raw counts for the continuum in shot 1601 (near peak current) plotted as circles. The blue line is a linear fit to this section of the data, and over laid in red is artificial Poisson noise given the mean number of counts of the data. The noise does not follow a Poisson distribution, and the noise level is ~ 11% of the signal.

calculation of error bars in the results obtained with the Andor data sets. As a stylistic preference, error bars shown will be $\pm 2\sigma$ in length to show the 95% confidence interval to the fit.

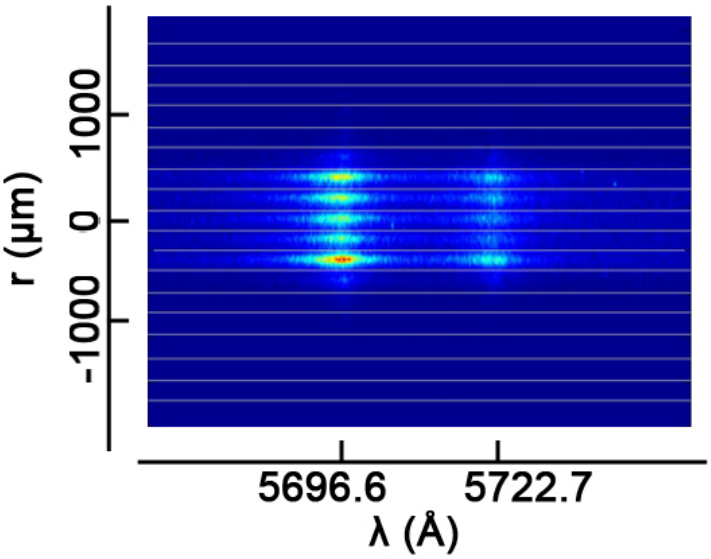

Figure 6.15: Raw spectra from shot 1598.

Early to Mid Time

Shown in Fig. 6.15 are the raw spectra versus radius for shot 1598 with the line positions labeled. This shot was selected to exemplify the early to mid time ranges in the evolution of the wire plasma spectra in the single wire explosion because it shared the same characteristics as the ”Mid Time” spectra in Sec. 5.2, but with $\sim 100ns$ earlier timing.

Figure 6.16 shows the timing of the gate pulse, with the green color bar representing the integration time. The integration window began $100ns$ into the pulse and lasted for $100ns$. At the start of data collection the current was $2.6kA$ and it had increased to $6.1kA$ by the end. The radial spot size at the wire plasma for a fiber is $166\mu m$ for all of the experiments with the Andor setup.

The strongly emitting plasma is only about $1.6mm$ wide at this time and the fitted FWHMs of the spectra from shot 1598 are shown in the top plot

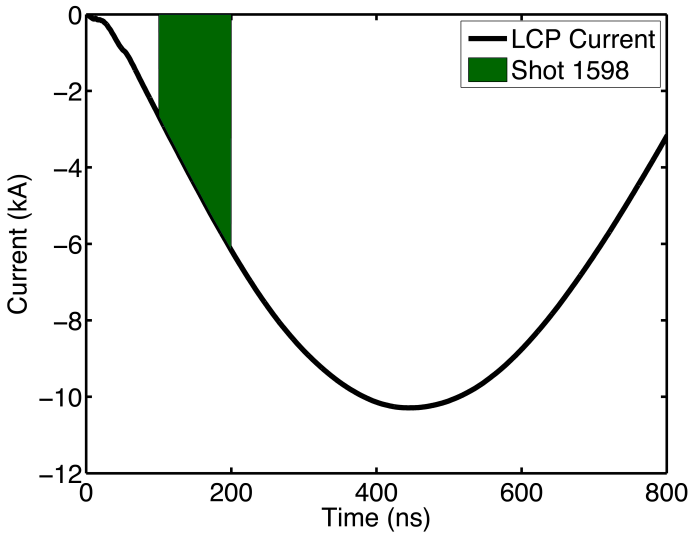

Figure 6.16: Current trace from shot 1598 with the spectral timing and integration window highlighted in green.

of Fig. 6.17. Due to the lower intensity levels at the edge of the plasma, the error bars on the widths are much larger for the four spectra obtained at $r = \pm 800\mu m, \pm 600\mu m$.

The middle plot in Fig. 6.17 shows the FWHM ratio of the 1/2 to 1/2 line over the 1/2 to 3/2 line. With the exception of the two spectra on the edge of the plasma at $r = \pm 800\mu m$, all of the width ratios and their error bars are in the opacity dominated regime. The only two points showing a hint of line broadening by magnetic field have very large error bars on the the width ratio which weakens the possibility for detectable magnetic field. Therefore it is not possible to infer a magnetic field using the Zeeman Broadening technique in this plasma at early to mid times. This possibility is further marginalized and confounded by the line intensity ratio. While the line intensity ratio range is less different from 2 than with the PIMax3 data presented in Sec. 6.1, it still varies significantly from the ideal ratio of 2. When the FWHM ratio falls below 1 it

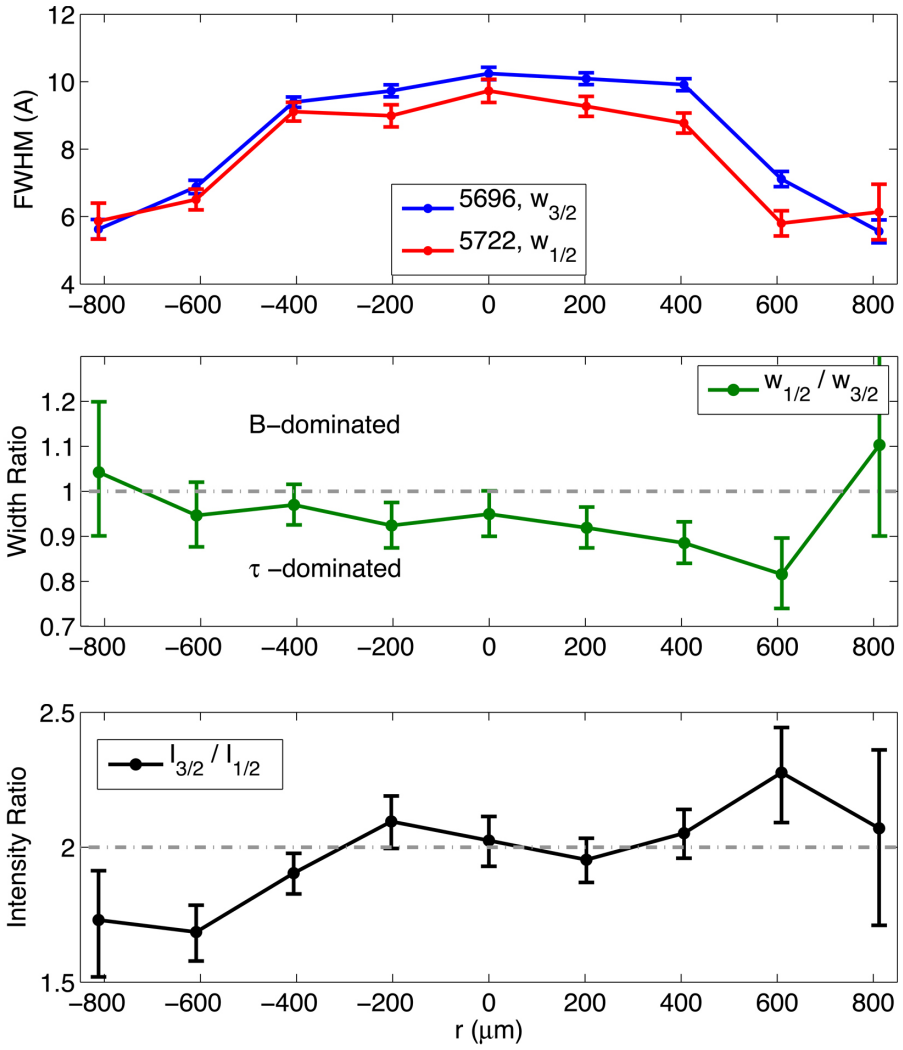

Figure 6.17: Fitted FWHM, line width ratios, and line intensity ratios for the spectra from shot 1598, shown in Fig. 6.15. Each error bar is $\pm 2\sigma$ long.

is expected that the line intensity ratio should be less than 2 because of opacity effects. However this is not the case. For the center positions the line intensity ratio is near 2, but there appears to be a trend of increasing intensity ratio across the plasma from ”negative” to ”positive” radii. This trend doesn't appear to be correlated to any of the other spectral characteristics such as electron density or total line intensity (see Fig. 6.19).

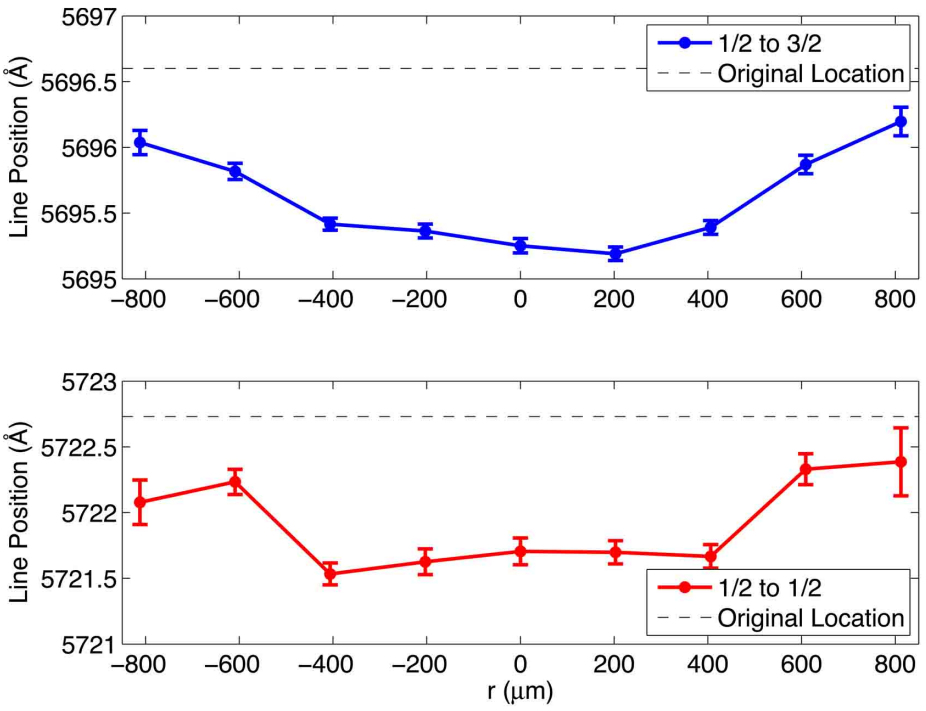

Figure 6.18: Shift of central wavelength for the 1/2 to 3/2 line in blue in the top plot, and the 1/2 to 1/2 line in red in the lower plot. Each error bar is $\pm 2\sigma$ long.

In addition, the intensity ratio on the "negative" side of the plasma indicates opacity effects. This is not inconsistent with the FWHM ratio because of the large error bars at large radii. However, it is physically unexpected to have opacity effects at the edge of the plasma. That said, opacity effects on the edge of the plasma may not be unphysical due to the high concentration of Al III which effectively lengthens the path length, giving more opportunity for reabsorption and emission of the lines. Yet the line intensity ratio distribution remains unusual. On the "positive" side of the plasma the FWHM ratio indicates opacity while the intensity ratio does not. If anything, the intensity ratio on the "positive" side of the plasma indicates the presence of a carbon contaminant adding to the intensity of the 1/2 to 3/2 line at 5696.6$\mathring{A}$.

Shown in Fig. 6.18 is the central wavelength shift of the two Al III doublet lines. Notice that in this data set, the lines have a larger shift than in the data from shot 1462 presented in Fig. 6.6. This larger shift indicates that this plasma in shot 1598 should be more dense. As seen in the top plot of Fig. 6.19 showing the first approximation electron density, indeed this plasma is more dense, with both the widths and the sifts showing the highest densities in the center regions as before.

Specifically, the top plot of Fig. 6.19 shows the first order electron density based on a Baranger treatment assuming no magnetic field. The error bars represent a $\pm 2\sigma$ variation from fitting the FWHM and an additional 20% error from using the Baranger method assuming no magnetic field [33]. In the plasma, the electron density ranges from $1.1 \times 10^{18} cm^{-3}$ to $1.8 \times 10^{18} cm^{-3}$. This is in the same electron density range as obtained from the large bandwidth ”Mid Time” spectra that were analyzed using PrismSPECT. Both data sets show a denser plasma for lines of sight through the central region.

The line intensity distribution shown in the middle plot of Fig. 6.19 looks like a cross between the large bandwidth ”Early Time” and ”Mid Time” spectra in Sec. 5.2. The intensity has a fairly flat top (similar to ”Early Time”) with the beginnings of a peak intensity near the drop in density (similar to ”Mid Time”).

Peak Time

An image of the raw spectra from shot 1601 is shown in Fig. 6.20. This set of spectra was obtained with a $100ns$ camera gate beginning $350ns$ after the start of the current pulse. The end of the integration time corresponded with peak cur-

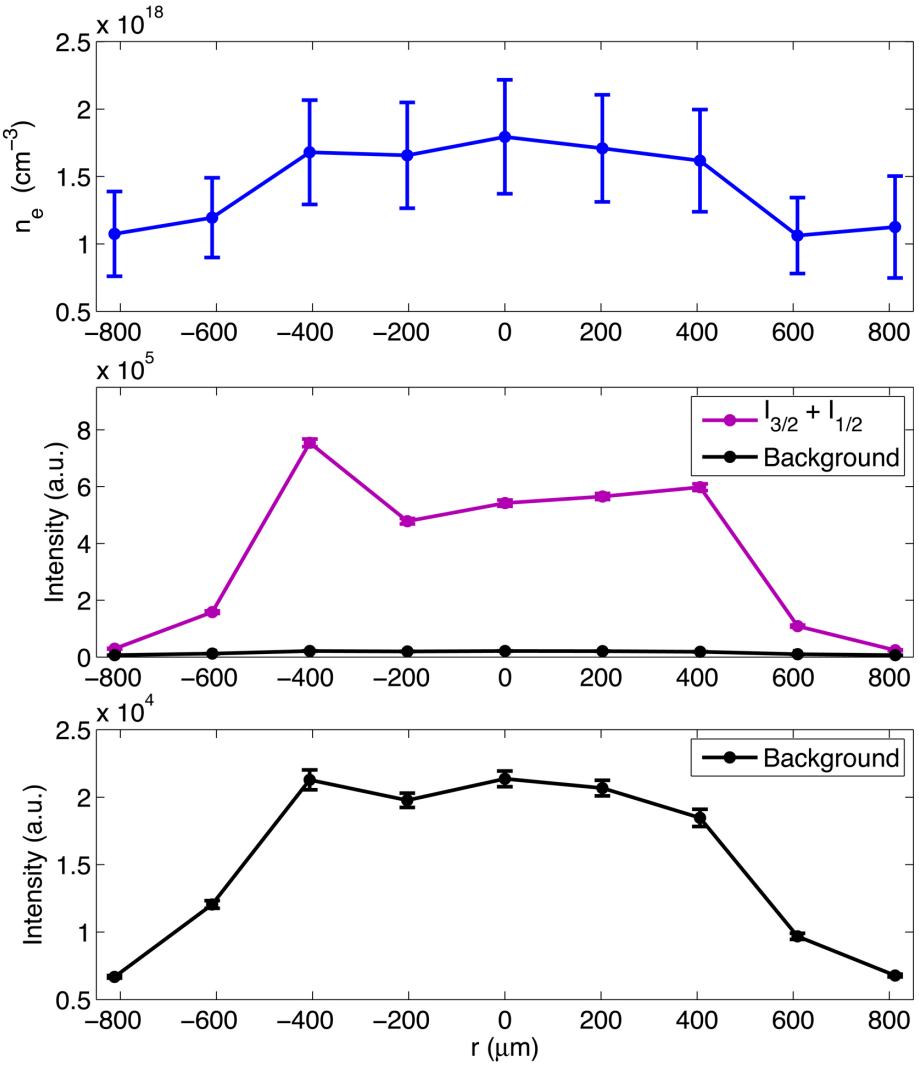

Figure 6.19: First order electron density, total line intensity, and background continuum intensity levels for shot 1598 as a function of radial position. Each error bar is $\pm 2\sigma$ long.

rent, and the average current through the plasma during the integration window was $10kA$. A plot of the current trace for shot 1601 is shown in Fig. 6.21 with the data integration window overlaid in blue. These data were taken at a similar stage in the single wire explosion as the spectrum that indicated the presence of magnetic field in Sec. 6.1, except that in this shot the current is increasing throughout the $100ns$ window of data collection.

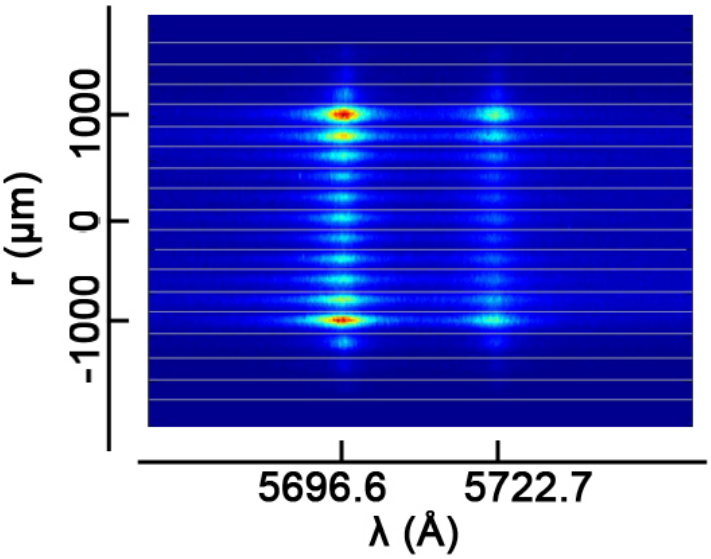

Figure 6.20: Raw spectra from shot 1601.

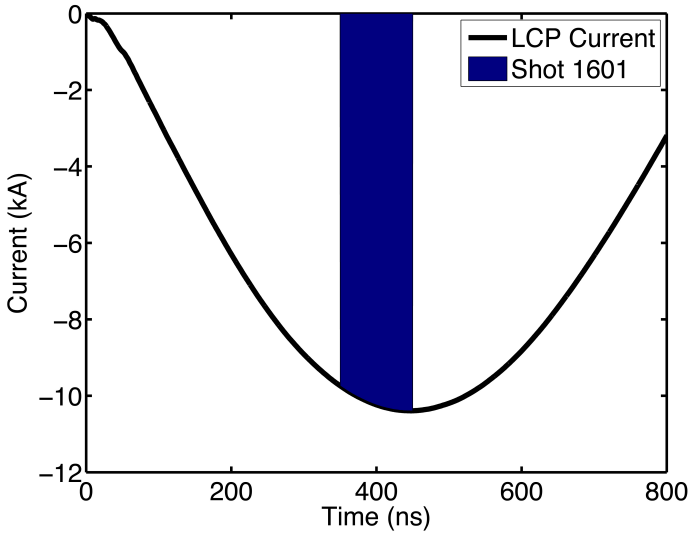

Figure 6.21: Current trace from shot 1601 with the spectral timing and integration window highlighted in blue.

At 350−450ns into the current pulse the exploding wire plasma has expanded to a diameter of $\lesssim 2.8mm$. Shown in the top plot of Fig. 6.22 is the FWHM of the two Al III doublet lines at 5696.6$\AA$ and 5722.7$\AA$ as a function of radial position across the wire, with the original wire position located at $r = 0\mu m$. The FWHM

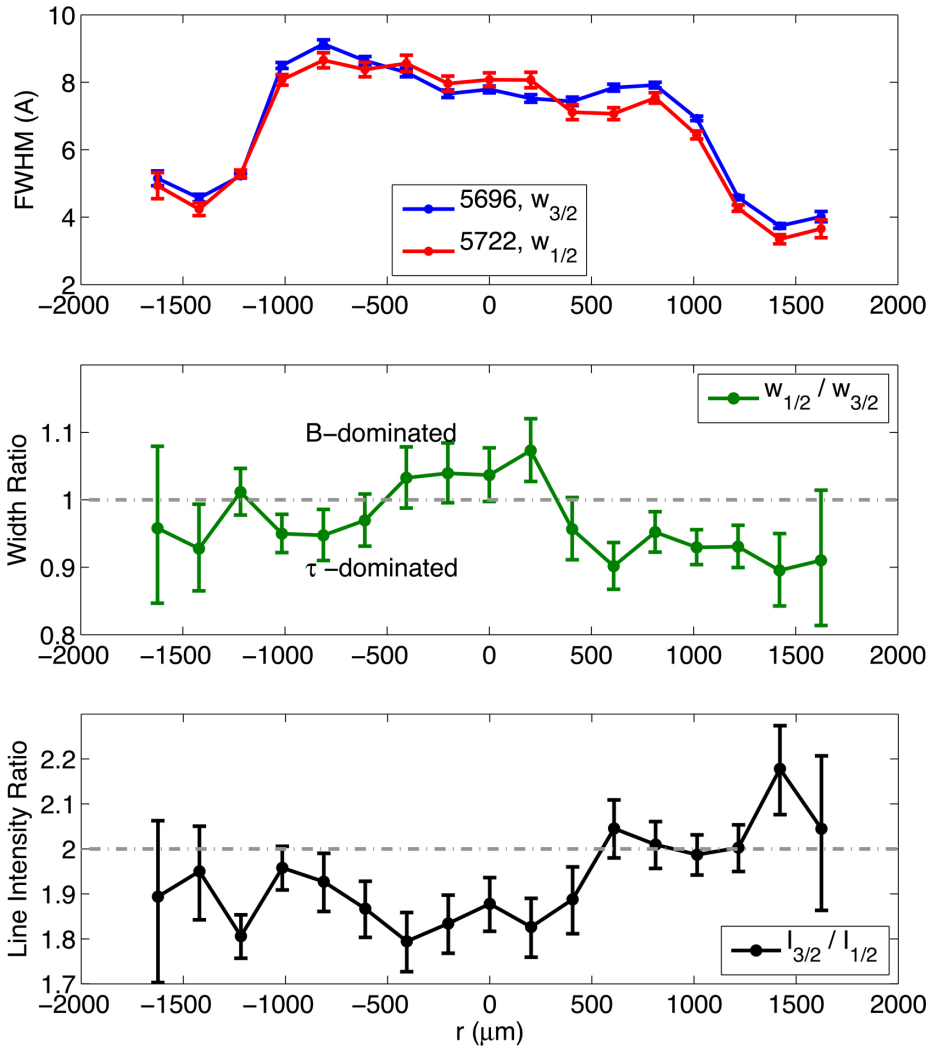

Figure 6.22: Fitted FWHMs, line width ratios, and line intensity ratios for the spectra from shot 1601, shown in Fig. 6.20. Each error bar is $\pm 2\sigma$ long.

ranges between 3.3$\mathring{A}$ and 9.1$\mathring{A}$.

The ratio of the FWHMs of the two Al III lines is shown in the middle plot of Fig. 6.22 with each error bar $\pm 2\sigma$ in length. The FWHM ratio is like a litmus test for measurable magnetic field. For the spectra located at $r = -400\mu m$, $-200\mu m$, $0\mu m$, $200\mu m$, the FWHM ratio suggests the presence of magnetic field broadening of the line. The error bar for the ratio barely crosses

the magnetic field threshold of 1 only at the position $r = -400\mu m$.

Qualitative information may be gathered about the magnetic field and current density profile using Fig. 6.22. At this time, there appears to be magnetic field broadening within a radius of $500\mu m$, meaning that a significant amount of current would be flowing within that radius. This is in agreement with the findings using the Princeton Instruments setup in Sec. 6.1. While lower than preferable, the FWHM ratio of 1.07 at $r = 200\mu m$ provides the most promise for determining that there is magnetic field broadening in this set of spectra.

The intensity ratio distribution shown in the lower plot of Fig. 6.22 again provides an interesting and unexpected story, while being different from the distribution from the early/mid time spectra in shot 1598 shown in Fig. 6.19. Here at the smaller radii, which indicate the possibility that magnetic field broadening is present in the width ratio, the intensity ratio is below 2, indicating opacity effects are present. The center four values range between 1.8 and 1.9. The low intensity ratio strengthens the argument for magnetic field broadening at these locations because a significant difference in the FWHM is present despite the counteracting effects of opacity.

At the "negative" side of the plasma the intensity ratio remains less than 2 while the FWHM ratio is in the opacity dominated regime. These two indicators are consistent. However, the first impression is that is physically unexpected to have opacity effects at an edge of the plasma. Yet with a higher concentration of Al III at the edges of the plasma, the path length for absorption remains long, which could create a larger optical depth, creating opacity effects.

At the "positive" side of the plasma, the intensity ratio is at or near 2, with

one spectrum at $r = 1400\mu m$ having a large intensity ratio, 2.2. This is inconsistent with the FWHM ratios which indicated opacity effects. The only way that these two trends could make sense together is if there was a substantial carbon contribution that was adding to both the intensity and the FWHM of the Al III line at 5696.6$\AA$. This is unlikely because the possible carbon line is not as sensitive to Stark broadening as the Al III lines. The fact that there are only indications for carbon in a third of the plasma seems unphysical as one would expect to have a uniform and symmetric carbon distribution in the plasma.

Due to the shot to shot variation and the oddities in the line intensity ratio distribution, it is important that information regarding the carbon distribution in the plasma be collected simultaneously in future experiments. Without any additional information about the carbon distribution, it is not possible to address these inconsistencies in the spectra quantitatively. Therefore it is not possible to determine definitely that magnetic field broadening has occurred and infer a value with meaningful error bars for this data set.

The electron density distribution in the plasma is shown in Fig. 6.24, assuming a single electron density and no magnetic field. The form of the distribution follows the same radial trend as the "Peak Time" spectra in Sec. 5.2 and the PIMax3 data used to determine the magnetic field in Sec. 6.1. However, the density is comparatively larger in these data. This is also confirmed in the spectra by the larger shifts in the wavelength of the line centers of the two Al III doublet lines (compared to the PIMax3 data in Sec. 6.1) as seen in the two plots in Fig. 6.23.

The line intensity distribution shown in the middle plot of Fig. 6.24 is also similar to the data used for determining the magnetic field in Sec. 6.1. It has

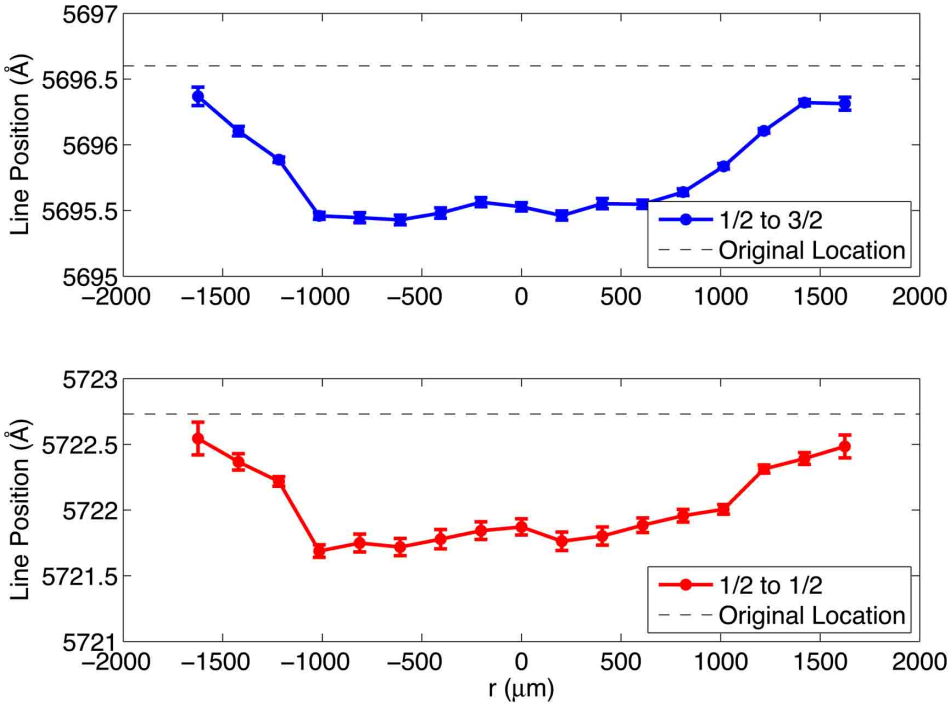

Figure 6.23: Shift of central wavelength for the 1/2 to 3/2 line in blue in the top plot, and the 1/2 to 1/2 line in red in the lower plot. Each error bar is $\pm 2\sigma$ long.

peaks in the distribution found with optical paths that view $r = \pm 1000 \mu m$, which are outside of the region where a magnetic field determination might be possible. The intensity distribution is again similar to an Abel transform of a cylindrical shell, indicating that the peak density of the Al III species is located at $r = \pm 1000 \mu m$.

The continuum background intensity is also plotted in the middle plot of Fig. 6.24 to show the scale difference between the continuum and the line intensity. To see the details of the continuum background, it is plotted by itself in the bottom plot in Fig. 6.24. While the distribution is similar to the line intensity, the peaks are located farther in, at $r = \pm 800 \mu m$, and the central continuum intensity does not decrease with the same proportions.

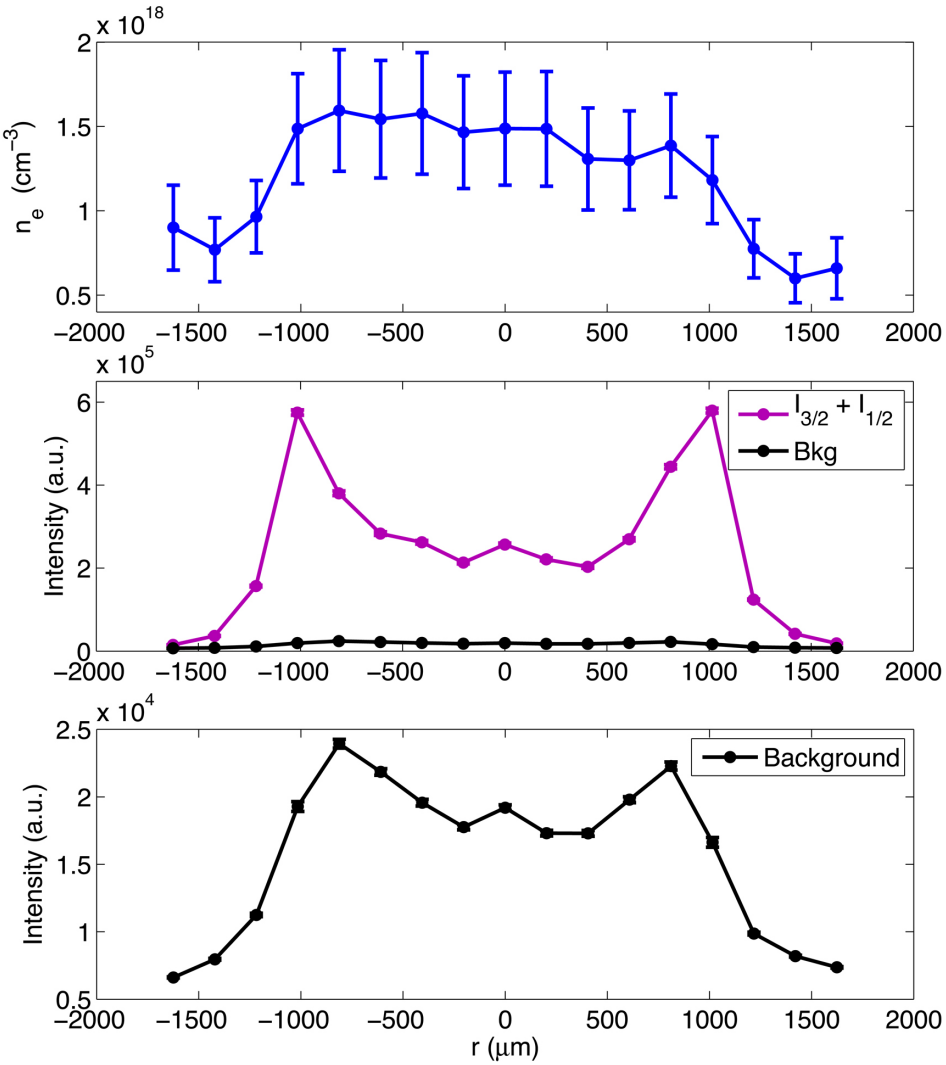

Figure 6.24: First order electron density, total line intensity, and background continuum intensity levels for shot 1601 as a function of radial position. Each error bar is $\pm 2\sigma$ long.

While it is important to solve the "carbon puzzle" so that any magnetic field inference based on a detailed line profile fit will not be suspect, it is possible to determine first-order magnetic field magnitudes from the ΔFWHA with caveats discussed in Sec. 6.1. Using the $\pm 2\sigma$ range of the FWHM shown in Fig. 6.22, the analogous average FWHA and ΔFWHA was calculated. These values were then used with the plots in [48] to determine the most probable B and a 95% confi-

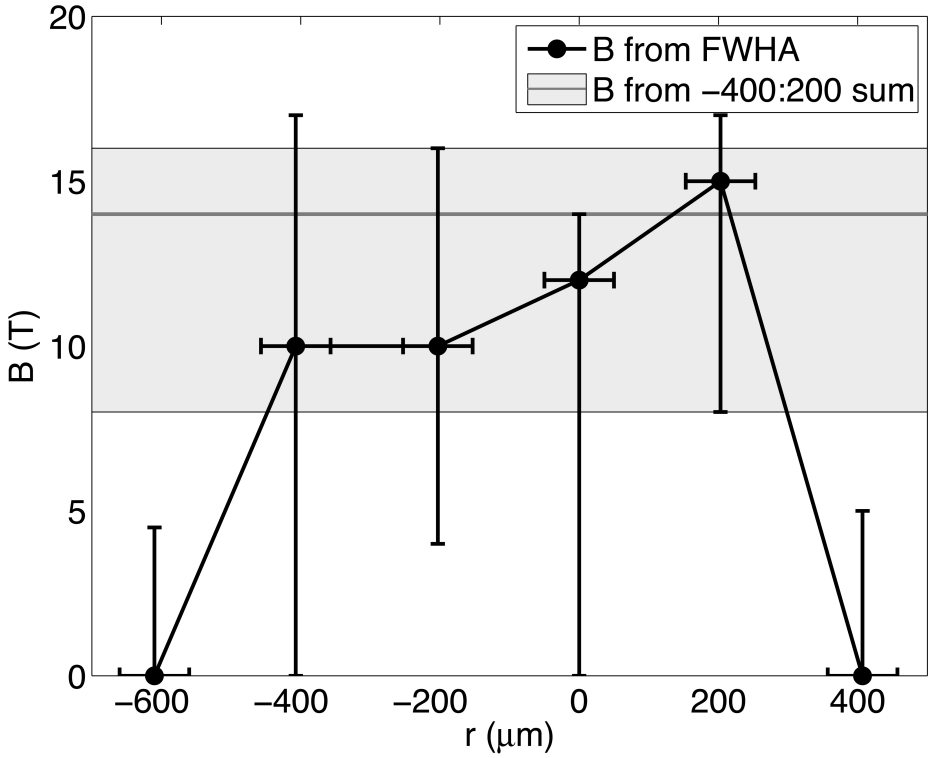

Figure 6.25: B inferred from the ΔFWHA shown in black with $\pm 2\sigma$ error bars from fitting the FWHA. If the four line profiles from $r = -400\mu m$ to $r = 200\mu m$ are summed, the resulting average B is the horizontal gray line with the shadded area as the B range resulting from the FWHA error.

dence interval from the average FWHA and ΔFWHA (remember it has limitations). The results are plotted as the black dots with $\pm 2\sigma$ error bars in Fig. 6.25 and Fig. 6.26.

As seen in Fig. 6.24, the Al III line intensity was lower for the spectra between $-600\mu m \leq r \leq 400\mu m$. Due to the reduced signal, the signal-to-noise ratio is lower than idea. In order to improve the signal-to-noise and reduce the error bars, the spectra at $r = -400\mu m,\ -200\mu m,\ 0\mu m,\ +200\mu m$ were summed because they had similar profiles and intensities. The new composite line profile was fitted to determine the most likely FWHA and ΔFWHA, as well as the $\pm 2\sigma$ for

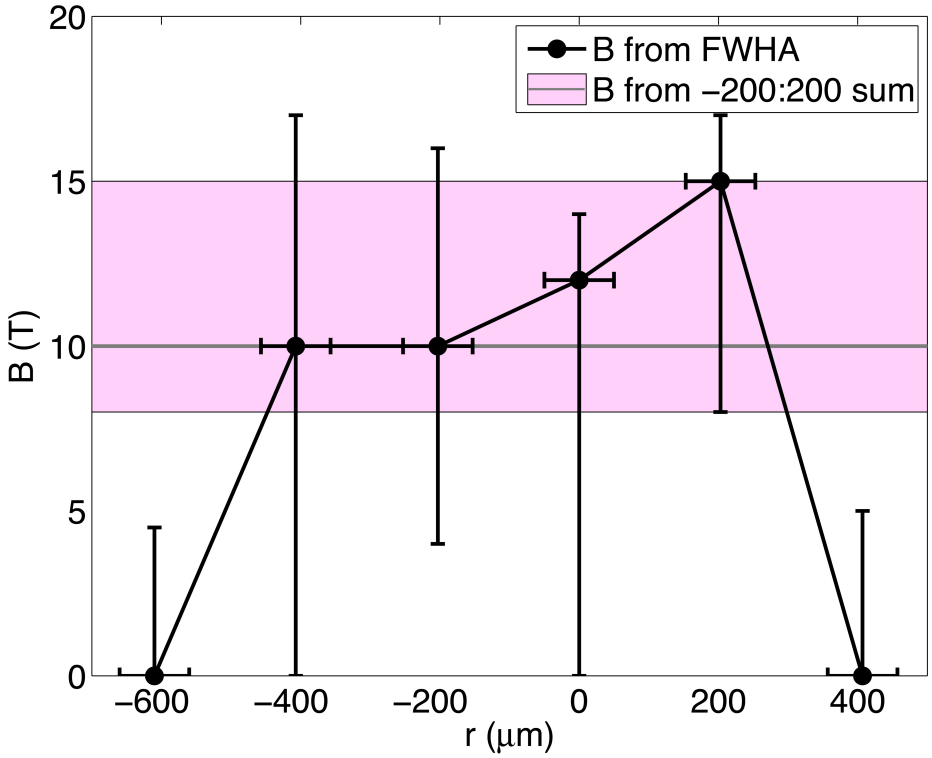

Figure 6.26: B inferred from the ΔFWHA shown in black with $\pm 2\sigma$ error bars from fitting the FWHA. If the three line profiles from $r = -200\mu m$ to $r = 200\mu m$ are summed, the resulting average B is the horizontal gray line with the pink area as the B range resulting from the FWHA error.

these values. Plotted in Fig. 6.25 is "averaged" B as the gray horizontal line and its $\pm 2\sigma$ range is the shaded gray area. From the composite line profile, the most likely B is $14T$ with a 95% probability of being between $16T$ and $8T$, recognizing that this is most applicable to the case when the plasma has only a single B and n_e, which is not true in these experiments.

If the line profiles at $r = -200\mu m,\ 0\mu m,\ +200\mu m$ were summed instead, then the most likely average B is $10T$ with a 95% probability of it being between $15T$ and $8T$. The new average B is plotted as the gray horizontal line in Fig. 6.26, with the 95% probability range as the pink area. The average B is lowered by

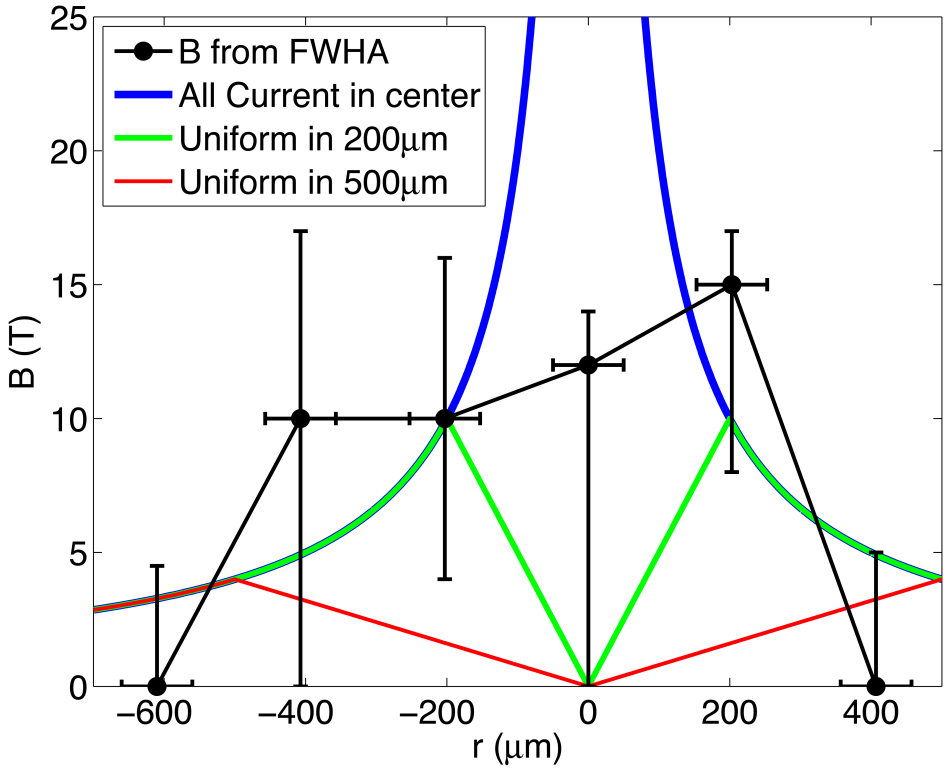

Figure 6.27: B determined from the ΔFWHA in black with magnetic field profiles from various distributions of a 10kA current.

omitting the profile at $r = -400\mu m$ despite its $B_{likely} = 10T$ because of the huge error bars related to that spectrum. The effect of omitting this spectrum is also seen in the reduction of the $\pm 2\sigma$ values for the average B.

It is likely that the magnetic field values inferred from the ΔFWHA are too high, as was true for the spectrum in Sec. 6.1, because they require a single B and n_e which is not the case in the plasmas in the experiments discussed in this thesis. However it is interesting to compare the inferred B's to magnetic field profiles of various current distributions. Plotted in Fig. 6.27 is the inferred B versus radius along with magnetic field profiles from three current distributions. The first, shown in blue, has 10kA of current flowing at the original wire position. The second, shown in green, corresponds to a 10kA current uniformly

distributed within a radius of $200\mu m$. The third, in red, has $10kA$ of current flowing uniformly with a radius of $500\mu m$. If the inferred B values based on the ΔFWHA were accurate, they would imply that the current is flowing within a $200\mu m$ radius. This is unlikely because it is reasonable to assume that a magnetic field inferred from the entire line profile, not just the average FWHA and ΔFWHA, would be lower. If the inferred values from fitting the line profile were reduced by 4.6 times from those inferred from only the FWHA, as with the spectrum in Sec. 6.1, then a current profile that was uniform within a $500\mu m$ radius could fit with the data. This would be consistent with the results in Sec. 6.1, which provided evidence for a significant portion of the current within a $500\mu m$ radius just after peak current.

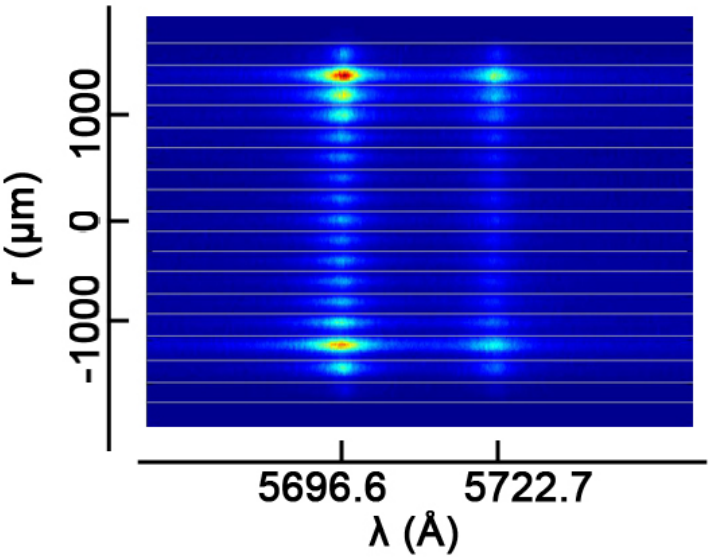

Figure 6.28: "Late Time" raw spectra from shot 1603.

Late Time

To discuss the plasma after peak current, shot 1603 was chosen to represent the "Late Time" spectra. The raw spectra are imaged in Fig. 6.28 with its wavelength and radial scale. The data were taken starting $460ns$ into the current pulse and integrating for $100ns$, i.e. beginning only $10ns$ after the end of the peak data. The current pulse for shot 1603 is shown in Fig. 6.29, with the integration timing and window overlaid in pink. The average current during this data collection period was also $10kA$. However, the current is decreasing during the data collection.

Shown in Fig. 6.31 are the line shifts of the central wavelengths of the Al III doublet lines. As compared to the "Peak Time" Andor data from shot 1603, the line shifts are not as large. This indicates that the density should be less in this shot. This is confirmed by the first approximation electron density fit shown as the top plot in Fig. 6.32. The distribution of the first approximation electron density is also supported by the distribution of the line shifts. With smaller sifts

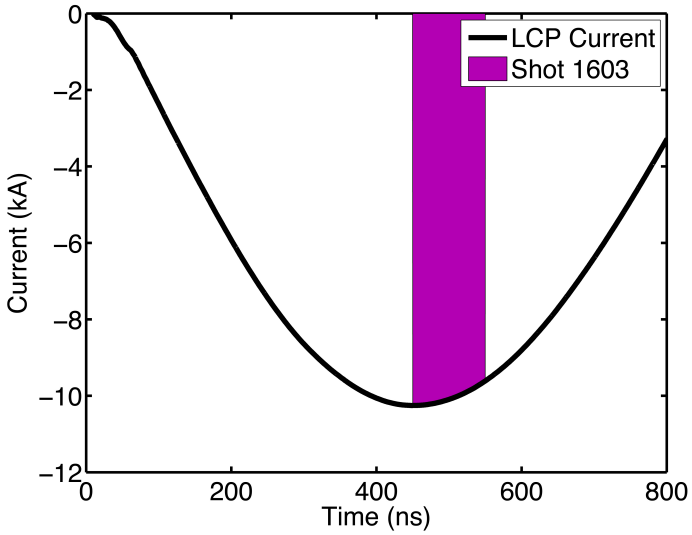

Figure 6.29: Current trace from shot 1603 with the spectral timing and integration window highlighted in magenta.

at the edges of the plasma, smaller electron densities are expected, which are confirmed by the line widths.

The top plot in Fig. 6.30 shows the FWHM of the Al III lines through the width of the plasma. The FWHM range between 4.3$\mathring{A}$ and 9.1$\mathring{A}$. This corresponds to electron densities between $7.9\times10^{17}cm^{-3}$ and $1.5\times10^{18}cm^{-3}$, assuming no broadening due to a magnetic field and a Baranger treatment based calculation of Stark broadening. The electron density as a function of radial position is the top plot in Fig. 6.32.

To examine the possibility for measurable magnetic field broadening in this data set, the FWHM ratio as a function of position is plotted in the center graph of Fig. 6.30. All of the width ratios fall below 1 with the exception of one point at $r = 1600\mu m$ with a lower error bar that crosses the value of 1. Therefore there is no possibility of determining a magnetic field in the set of late time spectra. The implication is that the current was flowing predominantly at radii larger than

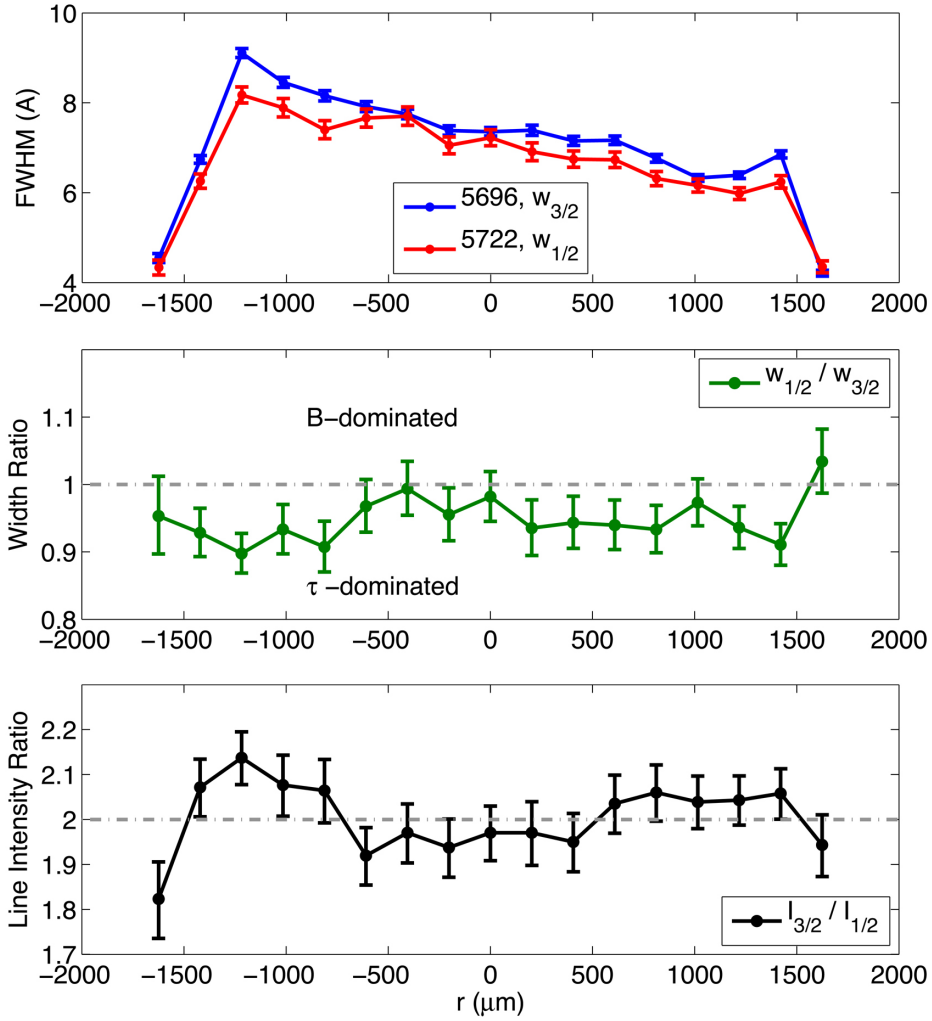

Figure 6.30: Fitted FWHM, line width ratios, and line intensity ratios for the spectra from shot 1603, shown in Fig. 6.28. Each error bar is $\pm 2\sigma$ long.

$r \geq 750 \mu m$.

While a magnetic field cannot be determined with this data, it is possible to extract other valuable information about the plasma from the line intensity ratios and the intensity distribution. The line intensity ratio as a function of position is shown in the bottom plot in Fig. 6.30. In stark contrast to the earlier times, the ratio distribution is symmetric. In the center region between r =

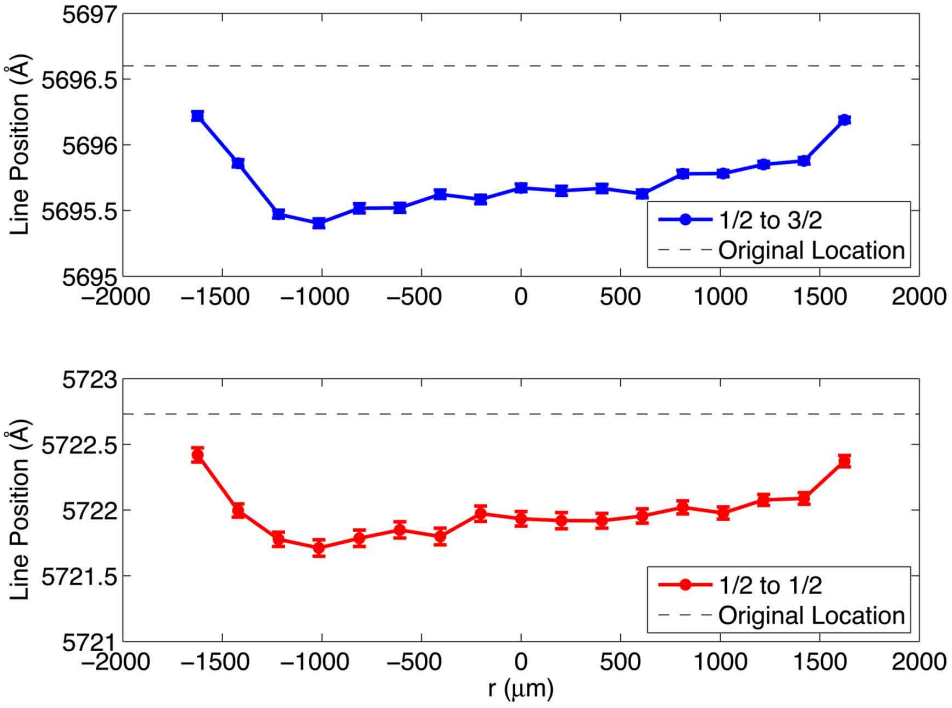

Figure 6.31: Shift of central wavelength for the 1/2 to 3/2 line in blue in the top plot, and the 1/2 to 1/2 line in red in the lower plot. Each error bar is $\pm 2\sigma$ long.

$-600\mu m$ and $r = 400\mu m$, the ratio is just below 2 indicating slight opacity effects agreeing with the FWHM ratios at those locations.

Outside the center region the line intensity ratio is greater than 2 indicating the possibility of carbon contamination in the 1/2 to 3/2 Al III line at 5696.6Å. A line intensity ratio that does not indicate opacity effects at large radii agrees with an intuitive picture of the plasma.

The total line intensity is graphed in the middle plot of Fig. 6.32. Between $460 - 560ns$ in the current pulse, the peak in the Al III line intensity occurs at $r = -1200\mu m$ and $r = 1400\mu m$. The background continuum distribution now matches the shape of the line intensity distribution with peaks at the same loca-

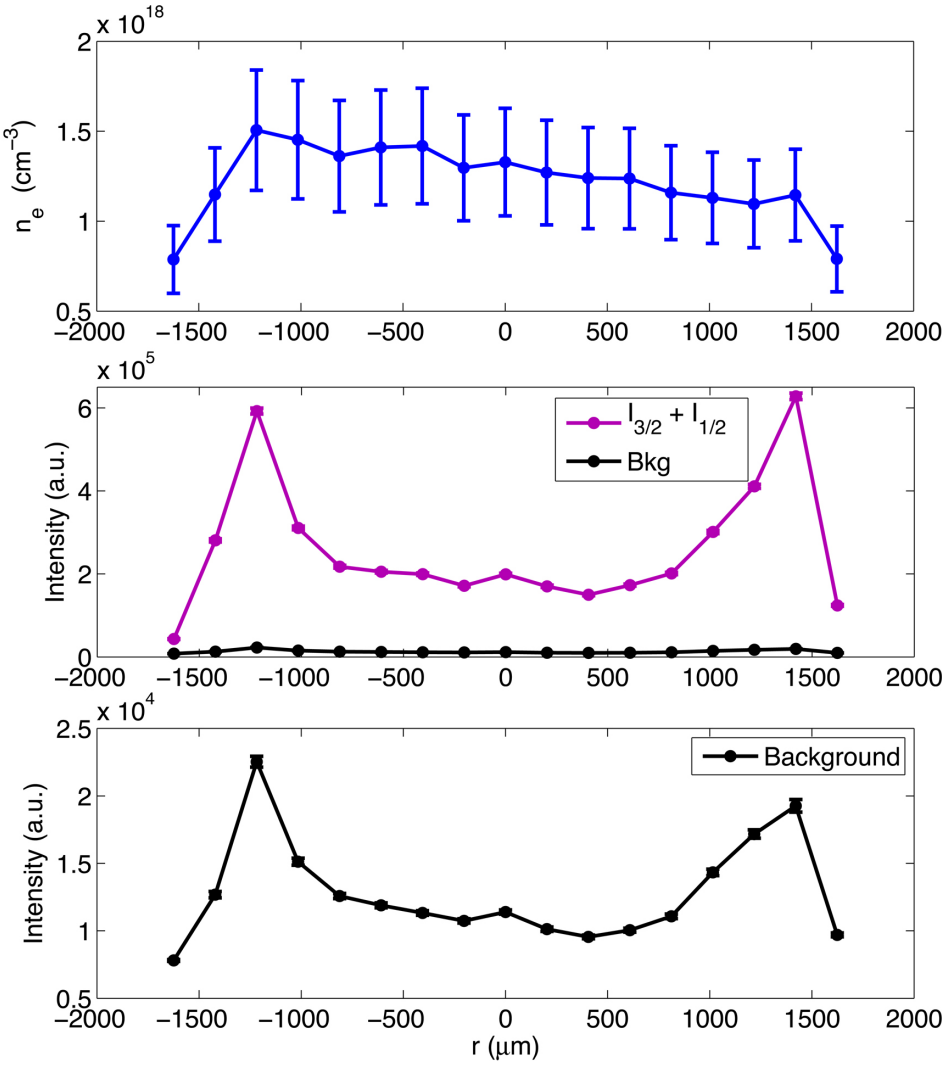

Figure 6.32: First order electron density, total line intensity, and background continuum intensity levels for shot 1603 as a function of radial position. Each error bar is $\pm 2\sigma$ long.

tion.

Summary

Information about the electron density and the Al III species distribution can be obtained at any time during the single wire explosion using the Al III doublet at 5696.6$\mathring{A}$ and 5722.7$\mathring{A}$. Figure 6.33 graphs the electron density through time and radial position during the single wire explosion. The times associated with each curve reflect the start time of the data collection, and each data set integrates for 100ns following the t_s start time. For readability, the error bars in Fig. 6.33 represent only the electron density error arising from uncertainty in determining the FWHM of the Al III line. The extra 20% error arising from using the Baranger based calculation is omitted in this plot but was included in the previous electron density plots.

The electron density evolution in Fig. 6.33 is in agreement with the large bandwidth data presented in section 5.2. Both data sets shows a higher density center expanding with a velocity of about 3km/s and decreasing with time. The expansion velocity was measured by tracking the edge of the higher density plasma which was located using the largest gradient in the electron density. In the early/mid time spectra shown in green and starting at 100ns into the current, the front occurs between 400 and 600 microns.

The distribution of the doubly ionized Al III through the plasma is tracked by the intensity distribution of the Al III lines. The evolution of the total Al III $4s - 4p$ doublet line intensity is plotted in Fig. 6.34. The Al III species begins at early/mid times as a thick shell distributed throughout the exploding wire plasma. At and after mid times the Al III species begins to collect in a shell. This shell expands radially outward with time while becoming narrower. To determine the expansion rate of the shell, the front of the intensity was tracked

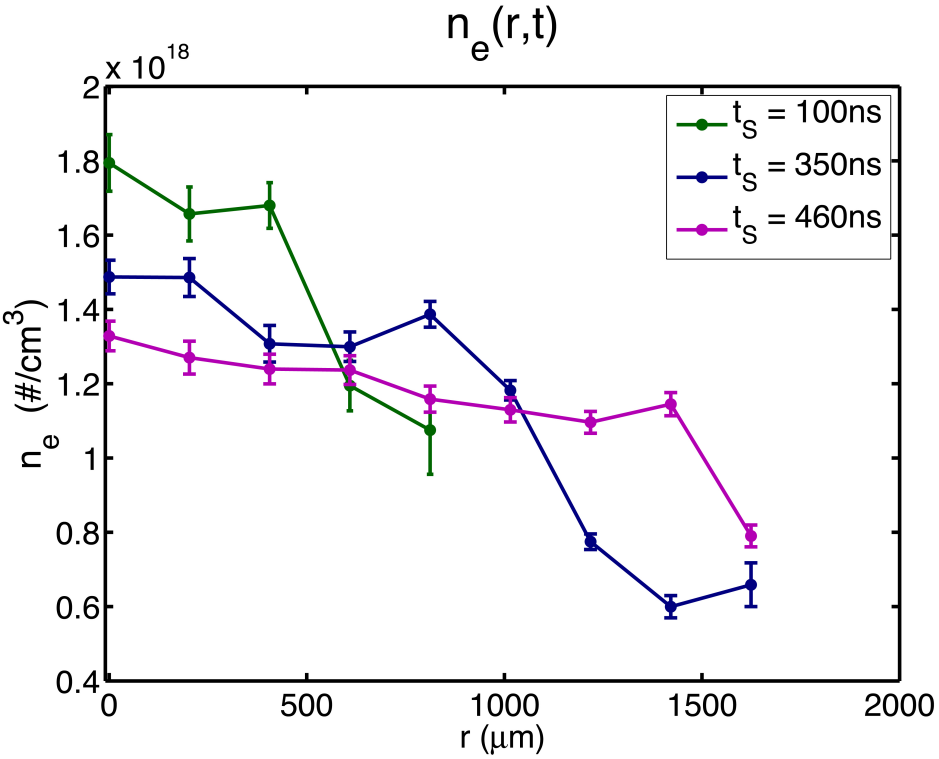

Figure 6.33: The evolution of the electron density through the single wire explosion. The error bars represent only the contribution from the FWHM determination of the Al III 5722.7$\AA$ line.

as it moved outwards. The front was defined to be located at the largest gradient in the line intensity. As an example, for the peak time spectra it occurred between the points at $1000\mu m$ and $1200\mu m$. The Al III intensity shell expanded with a velocity of about $3km/s$, the same as the plasma density front.

A magnetic field measurement in a single exploding wire plasma is most possible near peak current, given the experimental parameters and the location of the current. To measure the magnitude of the magnetic field with honest and accurate error bars, it is necessary to solve the puzzle arising from the line intensity ratio distribution. Information regarding the carbon distribution is paramount and unfortunately unavailable.

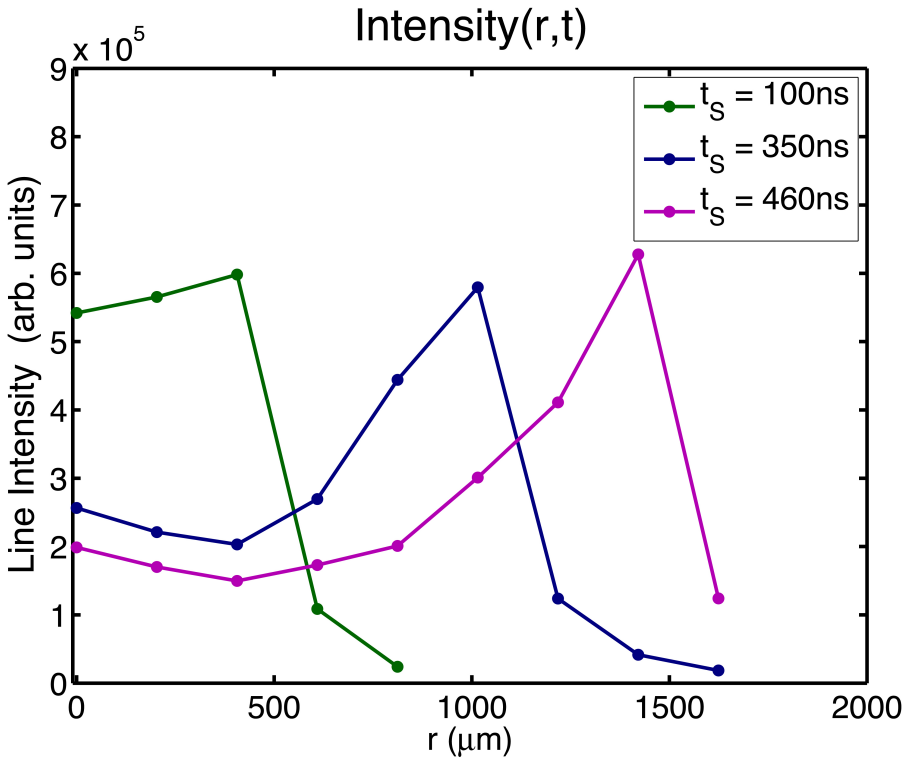

Figure 6.34: The evolution of the Al III line intensity through the single wire explosion showing the outward expansion of the Al III species.

The magnetic field information inferred from the peak time data set is in agreement with the conclusions resulting from the magnetic field measurement in Sec. 6.1. Firstly, the current is not flowing uniformly throughout the plasma column. Secondly, all of the current is probably not flowing at large radii. Thirdly, all of the current is not flowing at the original wire position.

CHAPTER 7

CONCLUSION

7.1 Summary of Results

The aim of this thesis is to add to the understanding of the physics in pulsed power driven single exploding wires with emphasis on the electron density, electron temperature, magnetic field, and current density profiles in the plasma. To accomplish these goals, high gain and high resolution spectral diagnostics were necessary. A preliminary investigation with an exploratory diagnostic setup, described in Sec. 2.3, was performed to narrow down the range of plasma electron density and electron temperature conditions in the experiment. Those results were presented in Sec. 5.1. While the magnetic field was determined to be just on the threshold of detectability because of the high electron density that were found, it was decided to continue to pursue magnetic field measurements using the Zeeman Broadening technique along with higher resolution electron density information. The high performance equipment needed for the measurement was not available in lab; therefore, it was necessary to borrow it.

Two demonstration units were borrowed from manufacturers and the experimental arrangements using them are described in Sec. 2.3. The first was from Princeton instruments, and the results obtained with it are presented in Sec. 6.1. The second was from Andor Technology and was used for both the high resolution magnetic field studies presented in Sec. 6.2, and large bandwidth electron temperature and electron density studies presented in Sec. 5.2.

It was determined in Sec. 5.2 that the exploding wire plasma consists of a

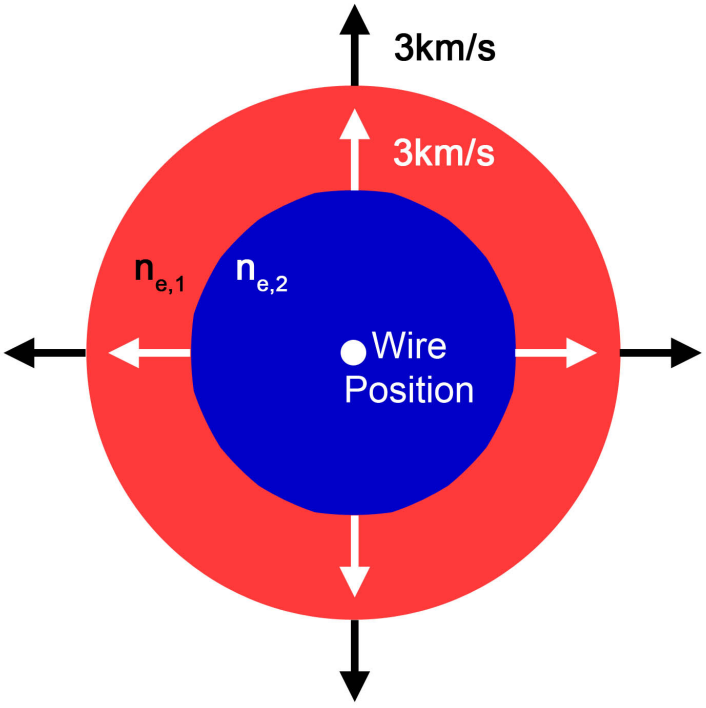

Figure 7.1: Cartoon of two density plasma with a hotter shell in red surround a colder and more dense central region in blue. Both expand with a velocity of $\sim 3km/s$.

hotter, less dense shell surrounding a colder and more dense core plasma. Due to the current drive profile, the magnetic field pressure never exceeded the thermal pressure and the plasma expanded throughout the current pulse. During the expansion, the plasma retained the structure of a hotter shell surrounding a colder denser core as drawn in Fig. 7.1. Both the shell and the denser central region expanded at $\sim 3km/s$. As the center region expanded, the electron density of that region decreased with time.

Unexpectedly, peak densities and temperatures occurred during the middle of the current rise (at peak dI/dt) instead of at peak current. This was apprently the case because of the relatively low current driving the single wire explosion.

If the current was higher, the magnetic field would have begun to pinch the plasma, inhibiting the expansion of the plasma. Instead, the magnetic field did not contain the plasma and it continued to expand, which led to cooling within the observed region as well as a decrease in electron density near peak current. At peak current the typical plasma diameter was $4mm$, whereas at peak dI/dt it was only $2mm$.

Using the electron densities and temperatures measured in Sec. 5.2, the skin depth of the plasma was calculated to be always larger than the diameter of the plasma as measured by visible light emission line intensity. Therefore it would be possible for the current to flow uniformly throughout the plasma. It would also be possible for the rising current to inductively move the current to the edge of the plasma if there were a hot, relatively low density plasma that was not visible at $r > 2mm$. Indeed, both of these hypothesis agree with "conventional wisdom" about exploding wires and wire array plasmas.

In Sec. 6.1, a magnetic field of $3.5T$ was inferred from the Al III doublet spectrum $500\mu m$ away from the original wire position during the interval of $485ns$ to $585ns$ into the current pulse. There was also strong indications of magnetic field broadening of the lines between $-976\mu m$ and $488\mu m$ away from the original wire position. The average current through the plasma was measured to be $10kA$ and was decreasing throughout the data collection.

In Sec. 6.2, a value of the magnetic field could not be determined due to a puzzle in the data set possibly arising from carbon contamination in the plasma. However, statistically significant indications of magnetic field broadening were present in the spectra taken near peak current. In shot 1601, the presence of magnetic field was inferred between $-400\mu m$ and $200\mu m$ away from the original

wire position 350ns to 450ns into the current pulse. During that time the current through the plasma was increasing and the average value was 10kA.

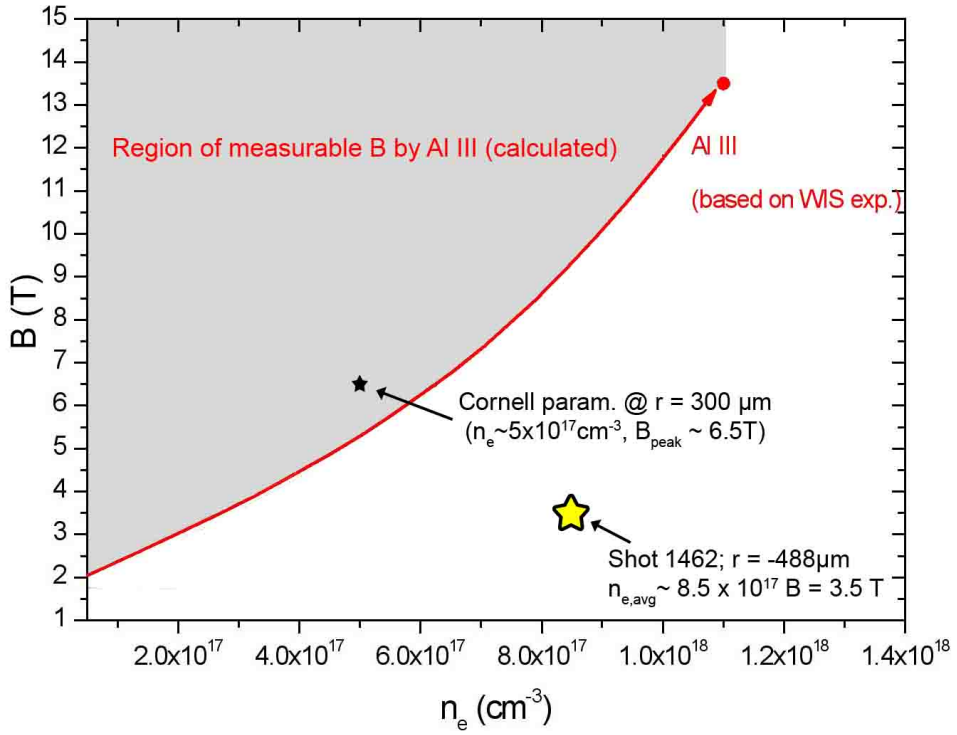

Figure 7.2: Parameter space for measurable magnetic fields from Fig. 4.2 with new measurement plotted as the large star.

From the experiments in this thesis it is now known that with sufficient resolution, a magnetic field measurement based on the Al III doublet can be made with electron density profile consisting of 50% of the emitting electrons at $1.2 \times 10^{18} cm^{-3}$, and 50% at $5 \times 10^{17} cm^{-3}$ and a magnetic field of $3.5T$. For these electron densities, the measured value actually falls below the recommended threshold. The severity of this can be seen in Fig. 7.2 where the new measured value is plotted as a star on the graph of the parameter space for reliably measurable magnetic field. Not only does Fig. 7.2 illustrate the difficulty of the measurement made in Sec. 6.1, but also how the limits of reliably measurable B field vary with density.

From the magnetic field measurements, several conclusion can be made. Firstly that the current is not flowing uniformly though the plasma. If this were the case the the magnetic field would reach a peak of $1T$ at $2mm$ away from the wire and would be too small to be detected at any point due to the high electron densities. The presence of a $3.5T$ magnetic field at $500\mu m$ in one experiment, disproves this hypothesis.

Secondly, all of the current is not flowing at the edge of the plasma or at radii above $1000\mu m$. If the current was flowing as a shell at a radius of $1000\mu m$ or larger, then there would be no magnetic field inside the current shell. If a thin current shell was located at $1000\mu m$, then the largest B value in the plasma would be $2T$. If the current was flowing along the edge of the plasma at a $2000\mu m$ radius, then the largest B value would be $1T$. The presence of a measurable magnetic field within a radius of $1000\mu m$ disproves this hypothesis.

Thirdly, all of the current is not flowing at the original wire position. If this were the case, there would be a doubling in the Al III $4s - 4p$ doublet FWHM difference between spectra taken at $-488\mu m$ and $-244\mu m$, which was not seen. Instead, the FWHM ratio varies only slightly between these locations at peak time.

The majority of current appears to be flowing within a $750\mu m$ diameter column between $350ns$ and $450ns$. Later, between $485ns$ and $585ns$, the current is flowing somewhere in a $1400\mu m$ diameter column. The locations of magnetic field are coincident with a decrease in line intensity and subsequently a decrease in the Al III species. As we move farther into the plasma, the temperature decreases while the density increases. At the plasma core, laser shadowgraphy indicates a possible third region of higher density, higher than the densities de-

termined from the emission spectroscopy. Within this high density region, one would presumably find neutral aluminum vapor near the original wire position. Summing these conclusions, it appears that a significant fraction of the current is flowing in the central regions ($r \leq 1mm$) of the plasma.

7.2 Future Experiments

It may be possible that the current is flowing at radii just outside the neutral aluminum wire core. To probe this hypothesis, one would need a series of Zeeman Broadening measurements and simultaneous measurements of the wire core. Absorption spectroscopy would provide the most useful information about the core plasma, while being extremely difficult to field in LCP3. Calibrated x-ray images to determine the neutral plus ion density could also be used to infer an effective ionization of a high density region. While simpler in setup and analysis, x-ray imaging in LCP3 would still pose a significant challenge.

At the very least, another series of single exploding wire experiments with wire cleaned of carbon contamination would be extremely valuable and hopefully solve the carbon puzzle encountered in Sec. 6.2. With carbon eliminated or significantly decreased in the plasma, it should be possible for additional Zeeman Broadening measurements of a single exploding wire plasma. In his thesis, Mark Johnston explored ways of eliminating carbon contamination on aluminum wires. He found that a 15 minute rinse with a 1M solution of H_2SO_4 followed by three washes in distilled water reduced the carbon line intensity by a factor of 3 [30].

If the carbon could not be eliminated through cleaning, then it would be

necessary to survey the carbon content in the single exploding wire plasma. Since the carbon line contaminating the Zeeman Broadening measurement is a C III line, other measurements of C III lines would provide valuable information about the C III ion distribution in the plasma. The best lines to use are the C III $1s^2 2s3s - 1s^2 2s3p$ triplet lines at 4647.42$\AA$, 4650.25$\AA$, and 4651.47$\AA$. These transitions share an energy level with the contaminating C III line at 5695.92$\AA$, from $1s^2 2s3p - 1s^2 2s3d$.

At peak current, the plasma at a radius of 500μm is challenging for Zeeman Broadening measurements due to the reduced intensity. Because of this, Zeeman Broadening combined with tomography would be an excellent technique for studying this region of the plasma. If two orthogonal views were used to collect spectra simultaneously as a function of radius, then it would be possible to extract more information about the plasma in the interior. The best way to collect such spectra is to have a coherent linear fiber array that splits into two at one end (like a "y"). Then half of the fibers are aligned to collect spectra from one view point while the other half collect light from an orthogonal field of view. It would be necessary that both views include the edge of the plasma to unfold the effects of integration along the other field of view. The other end of the fiber bundle would consist of all of the fibers so that all of the spectra can be dispersed and collected by the same spectrometer and detector.

Knowing that we can make a measurement with 50% $1.2 \times 10^{18} cm^{-3}$, and 50% $5 \times 10^{17} cm^{-3}$ and $3.5T$, it becomes possible to seek out these conditions (or more favorable ones with lower densities or higher B) in other experimental configurations such as an X pinch. X pinches are created by passing $50kA - 1MA$ through two or more fine metal wires that cross in the middle (forming an "X"

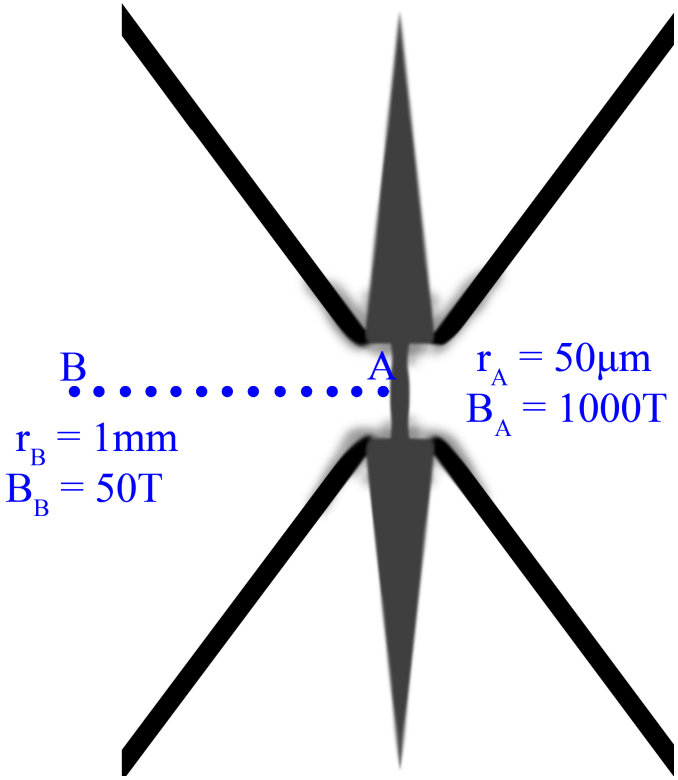

Figure 7.3: Drawing of an X pinch 2ns before pinch time. If there were 250*kA* flowing though the 50*μm* plasma column, at point A there would be *B* = 1000*T* and likely no Al III ions. At point B, there would be *B* = 50*T* with the possibility for Al III ions for a Zeeman Broadening measurement.

with two wires) [52, 42]. X pinches are an appealing application for Zeeman Broadening magnetic field measurement due to the extremely high magnetic field values at and near the crosspoint. At the cross point, a small Z-pinch is formed that is 200*μm* radius in early states and 5 – 50*μm* radius during the X pinch, for aluminum plasmas driven by a 50*ns*, 200*kA* current pulse [42]. If all the current flows through the small Z-pinch, then for a 200*μm* radius with 100*kA*, the magnetic field at the surface of the plasma column would be 100*T*. For a 50*μm* radius with 250*kA*, the magnetic field at the surface would be 1000*T*, as shown as point "A" in Fig. 7.3. At these locations an Al III 4s-4p Zeeman Broadening measurement would not be possible because there would not be

any Al III species, and even if there were the density would be too high with lower estimates of $10^{19} - 10^{20} cm^{-3}$ [41].

However, it is shown that with molybdenum (Mo) X pinches the density decreases rapidly in the plasma as one moves outward radially from the micro pinch to a value of $< 5.5 \times 10^{18} cm^{-3}$ at a radius of $1mm$ for a X-pinch driven by $80kA$ in $50ns$ [23]. Compared to Mo, Al X-pinches tend to be less dense and produce softer x-rays [41], and Mo does not expand as rapidly as Al [43]. Therefore, it is reasonable to believe that an Al X pinch corona would decrease in density as rapidly with radius as a Mo X pinch, if not more so. For the early time case with $100kA$ in a plasma column with $200\mu m$ radius, the magnetic field at $1mm$ away from the pinch would be $20T$. For the case near the X pinch with $250kA$ in a $50\mu m$ radius plasma, the magnetic field at $1mm$ away from the pinch would be $50T$, as shown as point "B" in Fig. 7.3. Therefore, at $1mm$ away from the X pinch a Zeeman Broadening magnetic field measurement should be possible assuming doubly ionized Al III ions exist at that location. It is also important to note that a measurement must be made before the x-ray burst (or in an X-pinch that doesn't pinch) because after the x-ray burst the dense plasma explodes outward and the plasma changes too rapidly.

It would also be interesting to study the jet of the X-pinch, as shown by the focal points labeled (1) in Fig. 7.4. In the jet one could possibly expect electron densities of $10^{17} cm^{-3} - 10^{19} cm^{-3}$ [35], and electron temperatures have been measured in some configurations to be $\sim 30eV$ [45]. At electron temperatures $\sim 30eV$ it is unlikely that any Al III ion species would exist to use for inferring a magnetic field. However, it would be interesting to investigate the possibility over many X-pinch configurations and current drives.

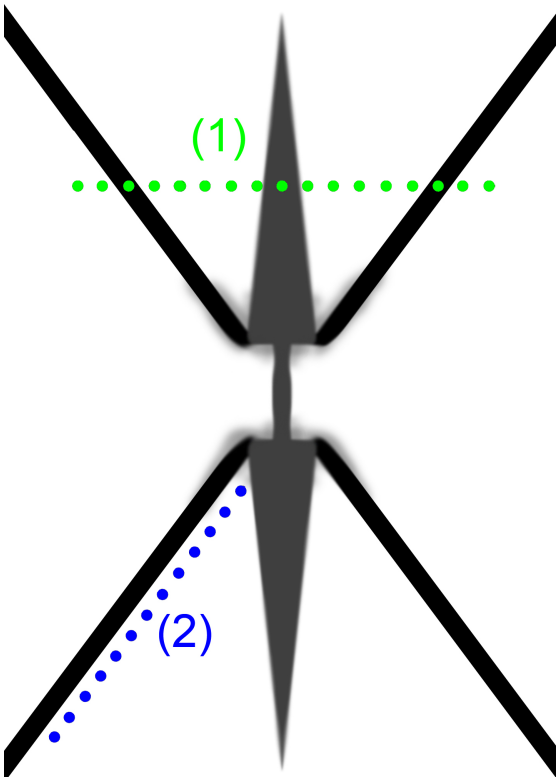

Figure 7.4: Drawing of an X-pinch showing two other viewing possibilities: 1) Across the jet plasma, and 2) Along one of the legs of the X-pinch.

One could also study the transition from global to local magnetic field effects on the ablation streams by looking along the leg of the X-pinch at the focal points labeled (2) in Fig. 7.4, in a manner similar to the work by Dr. Bott [7] and Mr. Collins [11].

Another interesting experiment would be to study a low wire number, non-imploding, cylindrical wire array. An array made of 3 fine Al wires would provide great diagnostic access to the ablation streams of the Z pinch, as can be seen in Fig. 7.5. While the precursor might have densities between $10^{18} cm^{-3}$ – $10^{20} cm^{-3}$, the ablation streams might have electron densities closer to $10^{17} cm^{-3}$. Assuming that Al III ion species are present, an electron density of

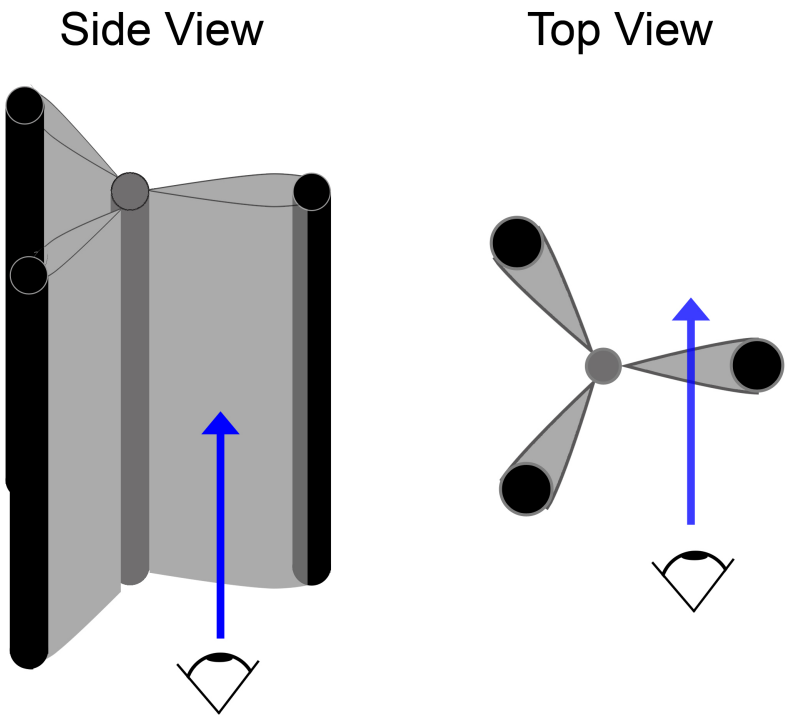

Figure 7.5: Drawing of 3-wire array setup, viewing through an ablation stream.

$10^{17} cm^{-3}$ would be small enough to detect Al III doublet line broadening due to fields of a few tesla. By looking through an ablation stream and recording spectra at many times during plasma evolution, it may be possible to study the transition of current from the wire cores to the precursor column.

A new spectroscopic system has been purchased from Andor Technologies by the Laboratory of Plasma Studies to be used for Zeeman Broadening magnetic field measurements. The system consists of a $750mm$ imaging Czerny-Turner spectrometer and a high gain gated ICCD Andor iStar camera. The spectrometer will have three gratings: $2400 grooves/mm$, $1800 grooves/mm$ and $600 grooves/mm$. With the high groove density grating, the diagnostic system will have a spectral resolution of $0.4 Å$. To make full use of the spectrometer, an

imaging flange was designed so that it would be possible to image a linear array of fibers with 0% cross-talk between adjacent fibers. This requires that there be $300\mu m$ of space between input fibers, e.g. for $100\mu m$ fibers there must be $400\mu m$ between core centers.

With this new spectroscopic system, the carbon puzzle in Sec. 6.2 will be addressed by making measurements of the carbon distribution in the plasma. Then an attempt will be made to clean the wires of the carbon contamination. If the carbon can be sufficiently reduced, another set of Zeeman Broadening measurements will be made to determine if more definitive magnetic field determinations can be accomplished in the single exploding wire plasma. If the carbon cleaning is inadequate, then the information on the carbon distribution will be used with existing measurements to address the magnetic field distribution in the plasma. Upon completion of the single wire experiments, the new Andor spectroscopic system will be used to study the magnetic field of a two wire aluminum X pinch as described above.

APPENDIX A

FIBER ALIGNMENT

To verify that the wire was properly focused onto the fiber array, and that the initial wire location was known in the recorded spectra, the alignment was checked and optimized for each shot. This was done by shining a bright continuum source onto the wire, at a 45° to 90° angle to the collection optics, ideally through a different port than used for the collection optics so that light is not backscattered off the window into the collecting lens. The incident light scatters off of the wire into the collection optics which creates an image of the wire, that must be focused onto the fiber bundle. If it is not focused by eye on the fiber bundle, then adjustments should be make so that a rough focus is obtained, enabling the fine adjustment and focus described below.

The following fine alignment procedure is for aligning the fiber array to collect signal perpendicular to the wire, radially across the plasma. If this is the first time setting up the optics, care should be taken to ensure that the center of the wire, the center of the optics, and the center of the fiber array are all aligned so that the light is not going at an angle through the port window or the lens. The lens, or compound lens, should not be rotated. This can be check by shining a level laser perpendicular to the port window that hits the center of the wire and the center of the fiber position. Then the lens element can be installed so that the laser goes through the center of the lens or through both the center of the entrance and exit of the compound lens. If installed properly, the laser point will be located at the same location on the fiber bundle prior to the lens addition.

To verify that the fiber head is not rotated and will collect all of the light from the lens, it is best to shine a laser through the spectrometer side of the

fiber. The laser light coming out of the chamber side will create a diffuse circle of light incident on the imaging lens that should be centered on the lens, and larger than the lens. This will ensure that all of the light exiting the lens will be collected by the fiber bundle for a particular point in the image. If it is not centered, then the fiber head can be rotated or translated slightly. If the diffuse circle is smaller than the lens, a different magnification should be used so that light is not lost. The laser light should also be focused to a small point on the wire.

Once a rough focus and alignment is obtained, the fine focusing is best done through the spectrometer and ICCD. With the continuum light shining on the wire, an image is taken of the resulting spectra. (To see the signal, the exposure will need to be lengthened and the gain set higher compared to typical shot settings.) If the wire image is focused, there ICCD signal will be a single line of continuum coming from a single fiber. If light is spread across many fibers either the focus or the alignment needs to be adjusted.

These adjustments are done through small changes in the fiber bundle's location using the micrometers on the translation stage. If the focus is the problem, then a change that increases or decreases the distance between the lens and the fiber will change the number of fibers with continuum signal. If "left or right" alignment is the problem, a change that moves the fiber bundle perpendicular to the incoming light will shift the signal to different fibers while not changing the number of fibers illuminated. The exception occurs when the focus is near ideal. At this point, a "left or right" shift will change the signal from being dim on two fibers to being bright on one fiber. At this point very small changes should be made in both the focus and the alignment so that the continuum signal is the

brightest and only comes from a single fiber.

Once the continuum signal is bright and coming from a single fiber, the entrance optics are aligned and the initial wire position is known.

APPENDIX B

RELATIVE CALIBRATION

A relative calibration was performed on the Andor experimental setups in two steps, which were similar in effect to the Flat Field Correction in Appendix C on page 145.

The first stage was to account for the intensity variation over the entire surface of the ICCD. To do this a uniform light distribution must be shinned on the face of the camera and the signal recorded. A uniform light distribution was created by taking a common camera flash lamp, diffusing the light with a polished low grit number diffuser to spread the light uniformly over a larger angle, and then placing it far away from the camera. Because the incident light is uniform, the signal should also be uniform within the noise error. If it is not, then it is important to record several signals and then average those signals to create a smoothed signal. Then each pixel value is divided into 1 to create a relative calibration factor for each pixel location on the ICCD.

The second stage is more similar to the procedure described in Appendix C on page 145. A camera flash lamp with a known color temperature (typically around 5600 K) was placed in the center of the experimental chamber at the location of the wire. The light was then transmitted along the same diagnostic path, i.e. through the lenses, fibers, and spectrometer, used in experiments, and the signal was recored by the ICCD. After applying the intensity calibration factor, the signal can then be compared to the known color temperature cure for that region of the spectrum. If there is a deviation, across all fibers or individual ones, then another calibration factor can be created for the path of the light (possibly dependent of the individual fibers). Because the fibers can shift locations

on the ICCD depending on small changes in alignment (even if it is only a few vertical pixels), it is important that the two calibration factors are kept separate and applied independently.

As different gratings are used in the spectrometer, even if the new grating has the same groove density and blaze as the old one, it is important to repeat the second stage of the relative calibration. Each grating has its own defects and dust contamination, which could affect the dispersion. Therefore each time a new grating is used, a new calibration should be performed. If one is routinely switching between two gratings a new calibration is not needed unless the spectrometer is physically opened (i.e. the gratings are not on a turret and must be changed manually), thereby exposing the gratings to damage and dust.

APPENDIX C

ABSOLUTE CALIBRATION

While an absolute calibration was not performed on the experimental setups presented in this dissertation, the process was discussed and Professor Maron wrote a guide about how to absolutely calibrate an optical spectroscopic system [33]. Being a useful tool, it seemed important that it not be lost between generations of LPS graduate students. Therefore it is reproduced exactly as received from Professor Maron, so that others may benefit.

Road map for

Absolute calibration of a spectroscopic system

Generally, one can either calibrate the entire system as a single unit, or calibrate separately the effect of each of the system's components, i.e., lenses and mirrors, spectrometer, and detector. While the first approach is more efficient for a specific measurement, it is not always practical and it obviously requires recalibration if the spectroscopic system is modified. Moreover, it is also more instructive to treat separately the different parts of the system. In the calibration procedures described below we will determine:

1. The efficiency of the light collection into the spectroscopic system
2. The efficiency of the spectrometer and detector

Let us consider the following typical arrangement:

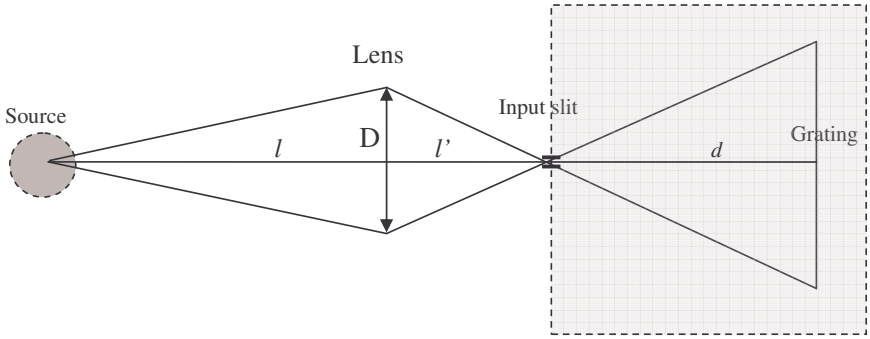

Fig. 1: A representative diagram of a spectroscopic system consisting of a lens and spectrometer (shaded rectangular) observing an extended source.

Let $\varphi_\lambda[s^{-1}]$ be the number of photons emitted at a specific wavelength per second from the volume observed in the plasma, and $\varphi'_\lambda[s^{-1}]$ the number of photons of a specific wavelength per second reaching the spectrometer slit.

Then: $\varphi'_\lambda = \frac{\pi(D/2)^2}{4\pi l^2} \cdot T(\lambda)\varphi_\lambda$ Eq. (1),

where D is the lens diameter, l the optical distance from the source to the lens, and $T(\lambda)$ the combined transmittance of all the optical components (e.g., windows, mirrors, lenses, prisms) mounted along the source-spectrometer path. It is now convenient to express Eq. (1) in terms of the system magnification, $M=l'/l$, and the spectrometer F-number, defined by $f^{\#} = d/G$ (where G is the "typical length" of the grating – see #1 below). From Fig. 1 we obtain $D/l' = d/G = f^{\#}$, therefore:

$$\varphi' = \frac{M^2}{16(f^{\#})^2} \cdot T(\lambda)\varphi \quad \text{Eq. (2)}$$

Note: here we assume that the F-number of the optical system matches that of the spectrometer,

namely, we assume that all the light collected by the optical system enters the spectrometer slit and exactly covers the grating. If this is not the case and $f^{\#}_{optical\ system} > f^{\#}_{spectrometer}$, a factor of $\left(\frac{f^{\#}_{optical\,system}}{f^{\#}_{spectrometer}}\right)^2$ must be added.

Note that at different wavelengths the lens position varies (due to the focal length λ-dependance) and the magnification changes accordingly. Eq. 2 implies that the collected number of photons depends on the square of the magnification. However, the observed volume, V, also depends on this factor: $V \approx S \cdot L/M^2$, where S is the slit area and L is the plasma length along the line-of-sight). Therefore, M^2 cancels out, and Eq. (2) becomes:

$$\varphi' \approx \frac{1}{16(f\#)^2} \cdot T(\lambda) SLJ \qquad \text{Eq. (3),}$$

where J is the photon density (averaged over the observed volume) emitted per second.

Note that in the case of a discrete spectral line $J = n_{up}\, gA$, where n_{up} is the transition upper-level population, A the Einstein coefficient, and g the degeneracy of the transition lower-level.

Note: here we assume that for all M (and thus for all λ) the plasma spatial extent in the plane perpendicular to the line-of-sight is at least as large as S/M^2.

Comments for system designers:

(i) While M is not needed for calculating the number of photons reaching the spectrometer slit, this parameter is important for the system design since it determines the spatial resolution perpendicular to the line-of-sight. Once the desired range of M is selected for the measurement, the lens focal length is determined. Then, the diameter of the lens is determined to match the spectrometer F-number for the *longest* wavelength measurable by the system. When shorter wavelengths are measured and the lens is positioned closer to the spectrometer slit, only a portion of the lens is needed to match the spectrometer F-number. Light reaching the outer parts of the lens may lead to stray light problems and require the use of an iris.

(ii) In order to improve the spatial resolution and obtain large signals, one should choose a lens that can be positioned as close as possible to the source. For a *fixed spatial resolution*, a lens positioned closer to the source is combined with a larger slit.

In principle, all the terms in Eq. (2) are known rather accurately, but one should pay special attention to the following:

1. In some cases, the spectrometer F-number, as specified by the manufacturer,

is a symbolic one that does not adequately reflect the light collection efficiency. Therefore, it is always recommended referring to the detailed documentation (or to take off the spectrometer cover) in order to determine the *F*-number. In the case of the common Czerny-Turner configuration and a rectangular grating and mirrors, it is calculated by dividing the entrance slit-mirror distance by the "equivalent mirror diameter" (obtained by equating the mirror area with a circle of the same area). It is important to emphasize that in the present approach, the *F*-number is defined through the light cone that fills up the spectrometer first mirror, which is wavelength independent. Had we treated the response of the spectrometer separately, we would also have to consider the variation of the effective *F*-number with wavelength due to the varying angle of the grating that results in a wavelength-dependence effective area of the grating. In the present approach this latter effect is already included in the calibration of the spectrometer-detector unit. For an experimental determination of the spectrometer wavelength-dependence effective *F*-number, see Appendix.

2. While the transmittance of most optics in the visible region is similar (~ 96 % for each surface), it can greatly vary in the UV region (down to a few percent), depending on the wavelength and the exact material composition and coating.

Eq. (3) links the light intensity reaching the spectrometer slit with the intensity emitted from the source. In the second stage of the calibration we will treat the spectrometer and the detector as a single unit and determine a conversion coefficient, $C(\lambda)$, that enables us to transform the measured signal into the number of photons entering the spectrometer per unit time: $\varphi' = I / C(\lambda)$, where I is the measured signal (given in counts for CCD-type detectors) and C is given in units of [counts/(photons/sec)] **for a given gate-time**.

Since the calibration is performed for pulsed-power experiments, we use a pulsed laser to account for the response of the detector to a pulsed signal. The calibration procedure is as follows (see also a comment below on polarization issue):

First, a bias or dark image should be acquired. The average dark signal acquired during the relevant gate should be subtracted from the measured signal. Next, attenuate the laser beam as needed in order to prevent damages to the grating and to the detector. Direct the beam into the spectrometer input slit, following an expansion so that the expanded laser beam fully reaches the grating. If the laser beam diameter, W, is greater than, say ~ 0.5 cm, the beam expansion can be performed using a

rather standard lens such that f/W $\geq f^{\#}_{spect.}$(where f is the lens focal length). Alternatively, if W is smaller, one may use a diffuser and image the diffused spot onto the entrance slit using an appropriate lense. Ideally, the expanded beam *exactly* covers the spectrometer first mirror. Measure the intensity of the beam in front of the entrance slit with a power-meter. Make sure that the entire beam that enters the slit also enters the power-meter. Note that the expansion of the laser beam is needed only for averaging the response function over the entire mirror and grating areas, so that small defects on the grating and mirror surfaces would not invalidate the calibration. Now, measure the signal intensity at the detector by triggering the gate of the ICCD attached to the exit slit of the spectrometer, so that the laser pulse is fully contained within the gate of the ICCD. The ratio of the counts on the ICCD (integrated over the entire line profile, $\sum_{Line} I_i$, where I_i represents the counts in the i^{th} column of the CCD array) to the power of the attenuated laser light, **given in number of photons per second**, (measured separately, including the effect of the expanding lens), is the conversion factor $C(\lambda)$.

Substituting $\varphi' = I / C(\lambda)$ into Eq. (3) we obtain J_λ - the photon density (averaged over the observed volume), at a wavelength λ, emitted per second:

$$J_{\lambda(center)} = \frac{16(f^{\#})^2 I}{T(\lambda)C(\lambda)SL} \qquad \text{Eq. (4),}$$

where the subscript *"center"* indicates that J is retrieved from a signal measured at the center of the CCD pixel array. If the signal is recorded at other parts of the CCD, one must include additional correction factor – see Sec. "*flat field correction*" below.

Important note regarding polarization:

The efficiency of the diffraction grating may depend on the polarization of the incident light. Therefore, if the laser light is polarized, one should perform the calibration both for the S and P polarizations (*P-plane* is polarized parallel to the grating grooves, while *S-plane* is polarized perpendicular to the grating grooves). For completely unpolarized incident light, the efficiency curve will be exactly halfway between the P and S efficiency curves.

Expansion to other wavelengths

A straightforward expansion of the calibration to other wavelengths is achieved by repeating the procedure above using a different harmonic of the laser light, e.g., the 3^{ed} harmonic of a Nd:YAG laser at 3550 Å (the second is at 5320 Å). One can also use the common He-Ne laser to extend the calibration to 6328 Å, assuming the response to a CW signal is the same.

Pencil style calibration lamps offer additional possibilities using several techniques:

1. We take advantage of the fact that the three Hg I transitions at 5460 Å, 4358 Å, and

4046 Å, which are clearly seen in the Hg-lamp spectrum, have a common upper level. Thus, the relative spectroscopic system response to these transitions and their known *gA* coefficients, yield the relative calibration in these wavelengths. Assuming that the absolute calibration at 5460 Å is very close to that at 5320 Å, already obtained with the Nd:YAG, we also obtain the absolute calibration at 4358 Å, and 4046 Å.

2. Other mercury lines can be then used based on NIST studies that give the relative irradiance of approximately 15 lines [J. Reader et al., Applied Optics 35, 1996]. However, relying on that work may lead to large uncertainties due to possibly different characteristic spectra of variant lamps.
3. Employ prominent lines of various lamps, combined with *narrow band pass filters*. Here we point out the Hg I line at 2536 Å (typically responsible for ~ 90% of the total radiation emitted by mercury lamps), for which many manufacturers especially design high quality filters (prices range from $ 200 to $ 400). A signal of 30 mW (the indoor light contributes ~ 5 mW) is obtained by a standard power meter using a pencil mercury lamp (without a filter) operating at ~ 15 Ampere. Therefore, a measurable signal of ~ 15 mW is expected for the 2536-Å line after passing through a filter with a typical transmittance of ~ 60% .
4. Employ calibrated light sources (rather expensive > $ 1 k, but available also in the UV region 2000 – 4000 Å using deuterium lamp; the pre-calibration is usually valid up to a couple of hundred hours of operation).

The calibration procedure using lamps is basically similar to that employed using laser. Here it is demonstrated by measuring the response to the Hg I 5460 Å, 4358 Å, and 4046 Å lines. Relying on the absolute calibration for 5320 Å (which we assume is the same for the 5460 Å), here we only seek for the *relative response* among these three wavelengths. An important issue that affects the accuracy of the measurement is that the same area of the lamp should be seen by the spectrometer slit in the 3 measurements. One possibility is simply placing the lamp close to the slit so there is sufficient signal. This arrangement may lead to stray light problems, resulting from direct illumination of the detector. However, the effect of stray light can be estimated by turning the grating to a nearby wavelength range free of lines. The measured signal in this range is an estimate for the noise and the stray light effect. Another possibility is performing the relative calibration using a lens with the appropriate *F*-number. For each of the 3 wavelengths, the lens should be shifted to match the spectrometer *F*-number, achieving maximum throughput. In this procedure, there are two main sources of uncertainty. The first is the error in the optimal lens position at each of the

wavelengths. The second source of error arises from the non-uniformity of the lamp combined with the different portion of the lamp that is imaged on the spectrometer slit at each wavelength (due to the different magnification at each wavelength). The relative measured signal by the ICCD divided by the Einstein coefficient of the respective transition is the relative combined response of spectrometer and the ICCD:

$$\mathrm{C}(5460\mathring{A}):\mathrm{C}(4358\mathring{A}):\mathrm{C}(4046\mathring{A}) \;=\; \frac{\mathrm{I}(5460\,\mathring{A})}{4.9\times10^{7}}:\frac{\mathrm{I}(4358\,\mathring{A})}{5.6\times10^{7}}:\frac{\mathrm{I}(4046\,\mathring{A})}{2.1\times10^{7}}$$

Note: Due to the relatively low intensity of the lamp emission (compared to a laser), the ICCD gate should be sufficiently long (several μs) to yield a good signal.

Flat field correction

The calibration described above is performed for selected wavelengths recorded at the middle of the CCD pixel array. However, minor misalignments and vignetting in the system that may result in variation in illumination over the field of the array, as well as non-uniformities in the response of the CCD pixels, require flat fielding. Flat field correction can be achieved by placing a continuum light source, of a known intensity curve, as close as possible to the position of the plasma source in the planned experiment. The same optical arrangement that will be used in the experiment should be used in order to record this continuum emission. A good continuum source can be a tungsten-halogen lamp. These lamps are characterized by a typical color-temperature of ~ 3100 K that can serve as a good reference for correcting the recorded spectra. Since here we are only interested in the *relative* calibration of the array, the uncertainty in the color-temperature does not lead to a significant error in the calibration at wavelength regions (say, at ~ 4500 – 5000 Å) that are far from the black-body peak curve. For example, assuming a color temperature of 3000 K instead of 3200 K, would lead to an error of less than 15% in the calibration for the entire range 4600 – 4800 Å. The result of this procedure is a function *F* that gives the relative response of the various parts of the CCD array along the dispersion direction (averaged along the slit direction). Normalizing the function by taking *F*(central column of pixels) = 1, we finally obtain :

$$J_{\lambda} = \frac{16(f^{\#})^{2} I}{T(\lambda)C(\lambda)F(pixel\#)SL} \qquad \text{Eq. (5),}$$

Note that flat fielding using this technique should be done within a limited spectral window of not more than ~ 30 Å, for which one can assume that the system response is *wavelength independent*. Otherwise, it would be impossible to distinguish between the effect of variation in illumination and the effect of wavelength sensitivity.

An alternative flat field correction can be achieved selecting a strong isolated spectral line and map its relative intensity across the entire CCD array by rotating the spectrometer grating. This procedure can be repeated for several spectral lines, resulting in a set of functions F_λ(pixel #), each such function gives the relative response of the various parts of the CCD array along the dispersion direction (averaged along the slit direction) for a specific central wavelength λ.

Calibrating the linearity of the ICCD response with respect to

3. Intensity
4. Gate duration (near minimum gate)

ICCD cameras usually have very good linearity (defined by the transfer function between the incident photonic signal and the final digitized output) with respect to the illumination intensity. Deviations from linearity should be less than a few tenths of a percent for several orders of magnitude. However, for short exposure times (usually below a few ns, depending on the system), deviations from linearity may occur also due to the camera response to the details of the shape of the high-voltage pulse, leading to a difference between the "electronic gate" and the actual "optical gate". The deviation can be determined by measuring the signal value versus the exposure time.

Appendix

Experimental determination of the spectrometer *effective F-number*.

The *F*-number determination can be performed using the generic configuration shown in Fig. 1. One can compare the signal obtained with and without a mask, whose aperture accurately defines a specific light collection cone, as shown in Fig. 2.

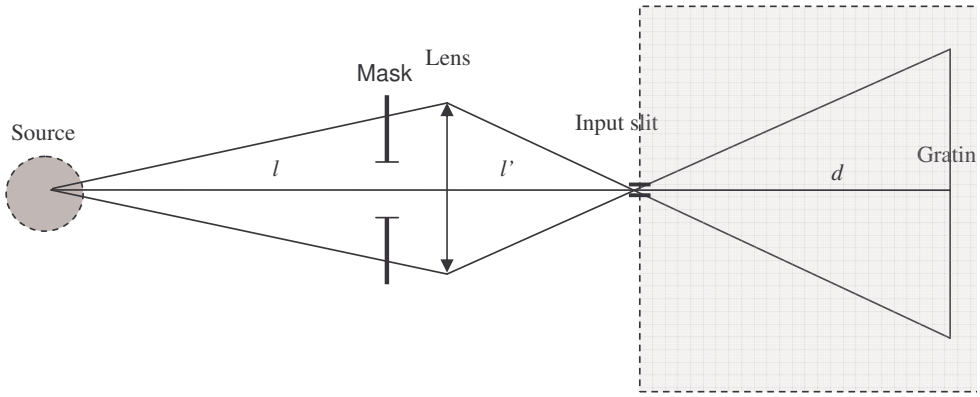

Fig. 2: The mask aperture determines the light collection cone with an $f^{\#}_{Mask}$.

Since the measured signal is proportional to $(f^{\#})^2$ (see Eq. 2), we obtain:

$$(f^{\#})^2 = (f^{\#}_{Mask})^2 \frac{I^2_{optimal}}{I^2_{With\,Mask}} \ ,$$

where the optimal signal is the signal obtained when the spectrometer first mirror (assuming Czerny-Turner configuration) is entirely illuminated.

Note:

- The spectrometer "effective *F*-number" varies with wavelength. Therefore, this measurement should be performed for various wavelengths.
- An accurate determination of the spectrometer *F*-number requires that the setup without the mask yields the optimal signal.

BIBLIOGRAPHY

[1] Michel Baranger. General impact theory of pressure broadening. *Phys. Rev.*, 112:855–865, Nov 1958.

[2] K. S. Bell, T. A. Shelkovenko, S. A. Pikuz, R. D. McBride, I. C. Blesener, P. F. Knapp, D. A. Hammer, J. B. Greenly, and Y. Maron. Optical spectroscopy experiments on the 500 kA XP pulsed-power generator. *AIP Conf. Proc.*, 1088:161–163, 2009.

[3] W. H. Bennett. Magnetically self-focussing streams. *Phys. Rev.*, 45(12):890–897, Jun 1934.

[4] S. N. Bland, S. V. Lebedev, J. P. Chittenden, G. N. Hall, F. Suzuki-Vidal, D. J. Ampleford, S. C. Bott, J. B. A. Palmer, S. A. Pikuz, and T. A. Shelkovenko. Implosion and stagnation of wire array Z pinches. *Phys. Plasmas*, 14(5):056315, 2007.

[5] K. S. Blesener, S. A. Pikuz, T. A. Shelkovenko, I. C. Blesener, D. A. Chalenski, D. A. Hammer, Y. Maron, and V. Bernshtam. Time resolved single wire aluminum optical spectroscopy experiments. In *Bulletin of the American Physical Society 52nd Annual Meeting of the APS Division of Plasma Physics*, volume 55, 2010.

[6] K. S. Blesener, T. A. Shelkovenko, S. A. Pikuz, I. C. Blesener, D. A. Chalenski, P. F. Knapp, J. B. Greenly, D. A. Hammer, and Y. Maron. Low current single wire optical spectroscopy experiments. In *IEEE International Conference on Plasma Science*, pages 1–1, 2010.

[7] S.C. Bott, D.M. Haas, Y. Eshaq, U. Ueda, S.V. Lebedev, J.P. Chittenden, J. Palmer, S.N. Bland, G.N. Hall, D.J. Ampleford, and F.N. Beg. Quantitative measurements of wire ablation in tungsten X-pinches at 80 kA. *Plasma Science, IEEE Transactions on*, 36(5):2759 –2764, Oct. 2008.

[8] D.A. Chalenski, P.U. Duselis, H.S. Barnard, and B.R. Kusse. Energy Deposition and Expansion Rates of Single 15μm Modulated and Un-Modulated Aluminum Wires. In *Plasma Science, 2005. ICOPS '05. IEEE Conference Record - Abstracts. IEEE International Conference on*, page 218, June 2005.

[9] K.M. Chandler, D.A. Hammer, D.B. Sinars, S.A. Pikuz, and T.A. Shelkovenko. The relationship between exploding wire expansion rates

and wire material properties near the boiling temperature. *Plasma Science, IEEE Transactions on*, 30(2):577 – 587, Apr 2002.

[10] F. F. Chen. *Introduction to Plasma Physics and Controlled Fusion*. Plenum Press, 2nd edition, 1984.

[11] G. W. Collins IV, D. Marsical, D. M. Haas, R. E. Madden, K. Gunasekara, J. Kim, M. L. L. Abarr, S. C. Bott, J. P. Chittenden, and F. N. Beg. Effect of the global to local magnetic field ratio on the ablation modulations on X-pinches driven by 80 kA peak current. *New Journal of Physics*, 14(4):043021, 2012.

[12] C. Colón, G. Hatem, E. Verdugo, P. Ruiz, and J. Campos. Measurement of the stark broadening and shift parameters for several ultraviolet lines of singly ionized aluminum. *Journal of Applied Physics*, 73(10):4752–4758, 1993.

[13] R.D. Cowan. *The theory of atomic structure and spectra*. Los Alamos series in basic and applied sciences. University of California Press, 1981.

[14] G. Davara, L. Gregorian, E. Kroupp, and Y. Maron. Spectroscopic determination of the magnetic-field distribution in an imploding plasma. *Physics of Plasmas*, 5:1068, 1998.

[15] Ramy Doron. Personal communication, 2012.

[16] Peter Duselis. *Factors affecting energy deposition and core expansion rates in single fine wire low current experiments*. PhD thesis, Cornell University, Ithaca, NY, 2004.

[17] Peter U. Duselis and Bruce R. Kusse. Experimental observation of plasma formation and current transfer in fine wire expansion experiments. *Physics of Plasmas*, 10(3):565–568, 2003.

[18] Peter U. Duselis, Jeffrey A. Vaughan, and Bruce R. Kusse. Factors affecting energy deposition and expansion in single wire low current experiments. *Physics of Plasmas*, 11(8):4025–4031, 2004.

[19] Marco A. Gigosos, Manuel Á. González, and Valentín Cardenoso. Computer simulated balmer-alpha, -beta and -gamma stark line profiles for non-equilibrium plasmas diagnostics. *Spectrochimica Acta Part B: Atomic Spectroscopy*, 58(8):1489 – 1504, 2003. 5th European Furnace Symposium

and 10th International Solid Sampling Colloquium with Atomic Spectroscopy.

[20] H.R. Griem. *Plasma Spectroscopy*. McGraw-Hill, 1964.

[21] H.R. Griem. *Spectral Line Broadening by Plasmas*. Pure and applied physics. Academic Press, 1974.

[22] H.R. Griem. *Principles Of Plasma Spectroscopy*. Cambridge Monographs on Plasma Physics. Cambridge University Press, 2005.

[23] D. Haas, S. C. Bott, V. Vikhrev, Y. Eshaq, U. Ueda, T. Zhang, E. Baranova, S. I. Krasheninnikov, and F. N. Beg. Dynamics of low density coronal plasma in low current x-pinches. *Plasma Physics and Controlled Fusion*, 49(8):1151, 2007.

[24] D.A. Hammer and D.B. Sinars. Single-wire explosion experiments relevant to the initial stages of wire array Z pinches. *Laser and Particle Beams*, 19:377–391, 2001.

[25] Min Hu and Bruce R. Kusse. Optical observations of plasma formation and wire core expansion of Au, Ag, and Cu wires with 0–1 kA per wire. *Physics of Plasmas*, 11(3):1145–1150, 2004.

[26] I. H. Hutchinson. *Principles of Plasma Diagnostics*. Cambridge University Press, 2nd edition, 2002.

[27] Prism Computational Sciences Inc. PrismSPECT. http://www.prism-cs.com/Software/PrismSpect/PrismSPECT.htm.

[28] J. D. Jackson. *Classical Electrodynamics*. John Wiley & Sons, Inc., 3rd edition, 1999.

[29] M. D. Johnston, Y. Y. Lau, R. M. Gilgenbach, T. S. Strickler, M. C. Jones, M. E. Cuneo, and T. A. Mehlhorn. Caterpillar structures in single-wire Z-pinch experiments. *Applied Physics Letters*, 83(24):4915–4917, 2003.

[30] Mark Johnston. *Ionization Dynamics of a Single Wire Z-Pinch*. PhD thesis, The University of Michigan, Ann Arbor, MI, 2004.

[31] H.J. Kunze. *Introduction to Plasma Spectroscopy*. Springer Berlin Heidelberg, 2009.

[32] J. M. Lerner and A. Thevenon. *The Optics of Spectroscopy*. Retrieved January 10, 2012, from http://www.horiba.com/.

[33] Yitzhak Maron. Personal communication, 2011.

[34] K. Matzen. Z pinches as intense x-ray sources for high-energy density physics applications. *Physics of Plasmas*, 4(5):1519–1527, 1997.

[35] I. H. Mitchell, R. Aliaga-Rossel, R. Saavedra, H. Chuaqui, M. Favre, and E. S. Wyndham. Investigation of the plasma jet formation in X-pinch plasmas using laser interferometry. *Physics of Plasmas*, 7(12):5140–5147, 2000.

[36] S. A. Pikuz, T. A. Shelkovenko, A. R. Mingaleev, D. A. Hammer, and H. P. Neves. Density measurements in exploding wire-initiated plasmas using tungsten wires. *Physics of Plasmas*, 6(11):4272–4283, 1999.

[37] S. A. Pikuz, T. A. Shelkovenko, D. B. Sinars, J. B. Greenly, Y. S. Dimant, and D. A. Hammer. Multiphase foamlike structure of exploding wire cores. *Phys. Rev. Lett.*, 83:4313–4316, Nov 1999.

[38] Yu. Ralchenko, A. Kramida, J. Reader, and NIST ASD Team (2011). NIST *Atomic Spectra Database* (version 4.1) [Online]. http://physics.nist.gov/asd National Institute of Standards and Technology, Gaithersburg, MD.

[39] G.B. Rybicki and A.P. Lightman. *Radiative Processes in Astrophysics*. John Wiley & Sons, 2008.

[40] G. S. Sarkisov, P. V. Sasorov, K. W. Struve, D. H. McDaniel, A. N. Gribov, and G. M. Oleinik. Polarity effect for exploding wires in a vacuum. *Phys. Rev. E*, 66:046413, Oct 2002.

[41] T. A. Shelkovenko, S. A. Pikuz, D. B. Sinars, K. M. Chandler, and D. A. Hammer. Time-resolved spectroscopic measurements of ~ kev, dense, subnanosecond x-pinch plasma bright spots. *Physics of Plasmas*, 9(5), 2002.

[42] T. A. Shelkovenko, D. B. Sinars, S. A. Pikuz, and D. A. Hammer. Radiographic and spectroscopic studies of x-pinch plasma implosion dynamics and x-ray burst emission characteristics. *Physics of Plasmas*, 8(4):1305, 2001.

[43] D. B. Sinars, Min Hu, K. M. Chandler, T. A. Shelkovenko, S. A. Pikuz, J. B. Greenly, D. A. Hammer, and B. R. Kusse. Experiments measuring the initial

energy deposition, expansion rates and morphology of exploding wires with about 1 ka/wire. *Physics of Plasmas*, 8(1):216–230, 2001.

[44] D. B. Sinars, T. A. Shelkovenko, S. A. Pikuz, Min Hu, V. M. Romanova, K. M. Chandler, J. B. Greenly, D. A. Hammer, and B. R. Kusse. The effect of insulating coatings on exploding wire plasma formation. *Physics of Plasmas*, 7(2):429–432, 2000.

[45] Daniel Sinars. *Time Resolved Measurements of the Parameters of Bright Spots in X-pinch Plasmas*. PhD thesis, Cornell University, Ithaca, NY, 2001.

[46] E. Stambulchik and Y. Maron. A study of ion-dynamics and correlation effects for spectral line broadening in plasma: K-shell lines. *J. Quant. Spectr. Rad. Transfer*, 99(1–3):730–749, 2006.

[47] E. Stambulchik, K. Tsigutkin, and Y. Maron. Spectroscopic method for measuring plasma magnetic fields having arbitrary distributions of direction and amplitude. *Phys. Rev. Lett.*, 98(22):225001, May 2007.

[48] S. Tessarin, D. Mikitchuk, R. Doron, E. Stambulchik, E. Kroupp, Y. Maron, D.A. Hammer, V.L. Jacobs, J.F. Seely, B.V. Oliver, and A. Fisher. Beyond Zeeman spectroscopy: Magnetic-field diagnostics with Stark-dominated line shapes. *Phys. Plasmas*, 18(9):093301, 2011.

[49] S. I. Tkachenko, V. M. Romanova, A. R. Mingaleev, A. E. Ter-Oganesyan, T. A. Shelkovenko, and S. A. Pikuz. Study of plasma parameters distribution upon electrical wire explosion. *The European Physical Journal D - Atomic, Molecular, Optical and Plasma Physics*, 54:335–341, 2009.

[50] W. van Etten. *Introduction to random signals and noise*. Wiley, 2005.

[51] E.E. Whiting. An empirical approximation to the Voigt profile. *Journal of Quantitative Spectroscopy and Radiative Transfer*, 8(6):1379 – 1384, 1968.

[52] S.M. Zakharov, G.V. Ivanenkov, A.A. Kolomanskii, S.A. Pikuz, A.I. Samokhin, and J. Ullschmied. Wire X-pinch in a high current diode. *Sov. Tech. Phys. Lett.*, 8:456, 1982.